The Kinematics of Faults in the San Francisco Bay Area
Inferred from Geodetic and Seismic Data

by

David Andrew Schmidt

B.S. (University of California, San Diego) 1997

A dissertation submitted in partial satisfaction of the
requirements for the degree of
Doctor of Philosophy

in

Geophysics

in the

GRADUATE DIVISION
of the
UNIVERSITY OF CALIFORNIA, BERKELEY

Committee in charge:
Professor Roland Bürgmann , Chair
Professor Douglas Dreger
Professor Steven Glaser

Fall 2002

The Kinematics of Faults in the San Francisco Bay Area

Inferred from Geodetic and Seismic Data

Abstract

The Kinematics of Faults in the San Francisco Bay Area

Inferred from Geodetic and Seismic Data

by

David Andrew Schmidt

Doctor of Philosophy in Geophysics

University of California at Berkeley

Professor Roland Bürgmann , Chair

The work presented in this dissertation focuses on the kinematics and mechanics of the Hayward fault, the Loma Prieta earthquake rupture, and the Silver Creek fault. To better understand their behavior and geometry, geodetic and seismic data are used in conjunction with elastic models of the crust. Along the northern and central segments of the Hayward fault, a steady interseismic deformation rate is observed. Variations in this rate along strike suggest a variable slip-rate distribution at depth indicative of locked and creeping patches. A locked patch that correlates with the presumed source region of the 1868 earthquake on the Hayward fault implies that elastic strain is accumulating at this location. The southern Hayward fault exhibits complex time-dependent slip. Interferometric Synthetic Aperture Radar (InSAR) is employed to visualize the crustal deformation signal by utilizing over 100 interferograms. Results suggest that the observed surface deformation is best explained

by a combination of transient fault slip and land subsidence. This is in contrast to the Silver Creek fault in the Santa Clara Valley where all of the deformation is attributed to differential aquifer compaction and expansion across the fault. Regional faults interact through the redistribution of stress in the crust and upper mantle. The effect of this change in stress on the creeping portion of the Hayward fault following the 1906 San Francisco earthquake is explored using a rate-and-state friction model. The predicted surface creep response, driven by the postseismic relaxation of the mantle following the 1906 event, is used to constrain the rheology of the lower crust. Rheologies that include a horizontal shear zone underpredict the surface creep response observed from offset cultural features. Inversions for the coseismic slip distribution of the 1989 Loma Prieta earthquake are performed to evaluate the sensitivity of the inversion to the prescribed fault geometry. Models the incorporate a dipping Loma Prieta fault and a vertical San Andreas are preferred over a single dipping plane. The findings presented in this thesis provide new insight on how active faults behave and interact throughout the earthquake cycle.

Contents

List of Figures

List of Tables

Preface

0.1 Introduction and Motivation

The San Andreas Fault System is the most studied fault network in the world. The foundation for our present-day understanding of active fault systems was developed after the $\mathbf{M}_w 7.7$ earthquake on the San Andreas fault in 1906. *Reid* [1910] first hypothesized that earthquakes represent the release of elastic energy which is accumulated over time in the crust. However, it wasn't until the acceptance of plate tectonics in the later part of the twentieth century that the buildup of elastic strain could be understood in the context of the larger earth system. While a general understanding of earthquakes is well established, the details of how faults behave throughout the earthquake cycle and interact within a fault system are not fully understood. Recent observations of transient aseismic events, slow earthquakes, and repeating earthquake sequences have illustrated the diversity of faulting behavior. The frictional, rheological, and geometrical controls that dictate how faults behave are current topics of research in the earth science community.

This dissertation focuses on the kinematics and mechanics of faults in the San Francisco Bay Area. Three major faults accommodate the deformation between the Pacific plate and Sierra Nevada microplate in the Bay Area: The San Andreas, the Hayward, and

the Calaveras faults. Of these three faults, the Hayward fault is the best system to study because it exhibits a wide range of faulting behavior and it is well instrumented. The Hayward fault has also received attention because it passes beneath an urban corridor in the Bay Area. A major earthquake on any part of the Hayward fault would result in a significant loss of human life and property. The work presented here draws upon a diversity of data sets including seismic waveform data, alignment array data, well level data, seismic relocations, extensometer measurements, leveling data, and surface displacements observed using the Global Positioning System (GPS) and Interferometric Synthetic Aperture Radar (InSAR). These data are used to study both seismic and aseismic processes along locked and creeping faults in an attempt to provide insight on the mechanics of fault systems. Each chapter represents an independent body of work that addresses different scientific and technical issues. In the next section, a detailed summary outlines the approach and principal findings contained in the following chapters.

0.2 Technical Summary

The technology behind InSAR was originally developed to produce topographic maps. *Gabriel et al* [1989] demonstrated that InSAR can also be used to image crustal deformation arising from processes as earthquakes or land subsidence. In this work, InSAR is used to observe the deformation along the Hayward fault. InSAR has the potential to resolve the details of both the spatial and temporal pattern of deformation. Before utilizing the InSAR data along the Hayward faut, a time-series methodology is developed for exploiting a large InSAR data set. In Chapter 1, 115 differential interferograms are

inverted for a time-dependent deformation signal in the San Francisco Bay Area. The linear inversion solves for the incremental deformation between synthetic aperture radar (SAR) scene acquisitions. The resulting time series spans from 1992 to 2000 and has a temporal resolution on the order of months. A nonlinear range-change signal is extracted from the InSAR data without imposing a model of the expected deformation. The time-series methodology facilitates the spatial and temporal interpretation of deformation in regions where the deformation is complex, such as the superposition of tectonic and land subsidence signals.

The InSAR time series is compared to leveling, well water level, and extensometer data in the Santa Clara valley to evaluate the resolution and accuracy of the inversion methodology. Over an eight-year period, up to 41±18 mm of land uplift is observed due to recharge of the confined aquifer. Maximum uplift occurred north of Sunnyvale and in the Evergreen Basin. Seasonal uplift and subsidence dominates west of the Silver Creek fault near San Jose with a maximum peak-to-trough amplitude of ∼35 mm. The pattern of uplift provides constraints on the spatial and temporal characteristics of water-bearing units within the aquifer. The Silver Creek fault partitions the uplift behavior of the basin, suggesting that it acts as a hydrologic barrier to fluid flow. While no tectonic creep is observed along the fault, the development of a low permeability barrier in the fault core suggests that appreciable shear has been accommodated in the Quaternary alluvium.

Having developed a tool to visualize time-dependent deformation, in Chapters 2 and 3 the focus returns to the Hayward fault. InSAR and surface creep data along the southern Hayward fault are used to interpret the complex, time-dependent deformation

observed in Fremont, California, from 1992 to 2000. A time-series analysis of 108 interferograms observes both right-lateral surface creep and vertical deformation. Surface creep is corroborated by independent alignment array data. An inversion of ascending and descending InSAR data is performed to assess the aseismic slip distribution over two time periods. The resulting slip distribution and residuals suggest that the InSAR and fault creep data are not easily satisfied by fault creep alone. Broad deformation to the west of the Hayward fault likely reflects a component of land subsidence of the Niles alluvial fan. The analysis of ascending and descending InSAR data suggests subsidence in 1998 on the east side of the fault near the outlet of Niles canyon. We find that the deformation is best explained by a combination of fault creep and land subsidence, although existing data sets are not sufficient to resolve the detailed kinematics of the deformation.

While the deformation along the southern Hayward fault is complex, surface creep rates along the northern 50 km of the Hayward fault appear to be constant over the last several decades. In Chapter 3, the depth of aseismic slip on the Hayward fault is addressed. The distribution of aseismic slip has implications for the mechanics of the fault system as well as for the seismic hazard. A least-squares inversion of multiple geodetic and seismic data sets is performed to determine the strike-slip distribution of the aseismic slip-rate. InSAR data from 9 independent ERS interferograms are stacked to obtain range-change rates from 1992 to 2000. Horizontal surface displacement rates at 43 sites are measured using GPS from 1991 to 1999. Surface creep observations and estimates of deep slip rates determined from characteristic repeating earthquake sequences are also incorporated in the inversion. The densely spaced InSAR data require a non-planar fault surface to adequately

model the near-fault data. The fault is discretized into 283 triangular dislocation elements that approximate the non-planar attributes of the fault surface. South of Hayward, a steeply, east-dipping fault geometry accommodates the divergence of the surface trace and the micro-seismicity at depth. Laplacian smoothing and a positivity constraint are included in the inversion. The InSAR data provide the greatest resolution on the shallow portion of the fault. The additional data sets complement the InSAR data and improve the model resolution. The inversion result suggests a heterogeneous distribution of aseismic slip-rate that is characterized by both locked and freely slipping patches. A locked region at depth coincides with the likely source region of the 1868 earthquake (**M** 6.8) on the southern Hayward fault.

The most recent large earthquake to occur in the Bay Area is the **M6.9**, 1989 Loma Prieta earthquake. The aftershock distribution and the diversity of aftershock focal mechanisms suggest that the Loma Prieta mainshock was complex with slip potentially occurring on multiple rupture planes. In Chapter 4, I explore how assumptions of fault plane geometry may effect the kinematic slip distribution. Waveform data from strong motion stations with absolute time and geodetic displacements are incorporated into a combined inversion for the kinematic slip history. Several different fault geometries are evaluated including (1) a 70° southwesterly-dipping plane, (2) a 65° dipping plane below 10 km with a vertical plane above, and (3) a model that includes a shallow, southwesterly dipping thrust on the east side of the primary rupture plane. Combined synthetic inversions suggest that the mapping of complex rupture onto a single fault plane can account for the variability in rake and slip magnitude of previously published source models. A bilateral slip

distribution is found consistent with previous studies. Results suggest a primary asperity that ruptured with oblique motion northwest of the hypocenter, consistent with the location of the initial aftershock response. The data prefer rupture on dipping structures suggesting that little slip occurred on a vertical San Andreas fault. A small concentrated patch of slip prefers the shallow dipping thrust fault, although the improvement in fit to the data does not appear to be significant.

The Loma Prieta earthquake acted to redistribute stress to neighboring faults. Along the southern Hayward fault, left-lateral creep was observed for 4 years following the 1989 event. It is expected that the 1906 earthquake produced a much larger change in stress on the Hayward fault. However no data exist to document how surface creep rates were affected by the 1906 event. In Chapter 5, numerical simulations are performed to predict the shallow surface creep response of the Hayward fault given the coseismic and postseismic stress history imposed following the 1906 San Francisco earthquake. The creeping section of the Hayward fault is modeled as a one-dimensional elastic system that behaves according to a rate-and-state constitutive law. This analysis requires prior knowledge of various fault parameters used to specify the rate-and-state formulation as well as the postseismic stressing history. The appropriate values for the fault parameters are determined by fitting the creep response observed on the southern Hayward fault following the 1989 Loma Prieta earthquake. No documented observations of creep on the Hayward fault were made immediately following the 1906 earthquake that can confirm or refute the details of our model predictions. However, large coseismic stress changes for the 1906 earthquake should have resulted in a left-lateral slip response of 0.03 to 0.21 m. Offset cultural features suggest

that creep rates along the Hayward fault have remained constant since about 1920 until the

1989 Loma Prieta earthquake. Modeling the surface slip helps to constrain the magnitude

of the imposed stress shadow and evaluate rheological models for the Bay Area.

Acknowledgements

As with any human endeavor, many individuals contributed in small and large ways to this dissertation. I would like to especially acknowledge some of those individuals who have helped me to complete my studies at Berkeley. First, I would like to thank Roland Bürgmann who served as my advisor, mentor, and friend during my graduate student career. After working with Roland for several years, I have gained an appreciation for his ability to remain optimistic and provide encouragement. Throughout the countless seminars and discussions, Roland always emphasized the exciting aspects of doing science. I hope that I can duplicate his educational model with my future students. John Lynch and Josh Roering first encouraged me to consider Roland as an advisor and I am grateful for their advice. I am appreciative for the patience exhibited by Doug Dreger as I juggled multiple projects. Doug guided me during my foray into strong motion seismology and helped to diversify my expertise. Eric Fielding acted as an invaluable resource while trying to learn the InSAR processing package, ROI PAC. With over 10,000 lines of code and no instruction manual, Eric patiently answered all of my inquires. The office staff in the Department of Earth and Planetary Science and the Berkeley Seismological Laboratory helped to ensure that the resources were available for me to complete my work. I would especially like to thank Charley Paffenbarger, Eleanor Blair, Christina Jordan, and Hank

Chapter 1

Time-dependent land uplift and subsidence in the Santa Clara valley, California, from a large InSAR data set

1.1 Introduction

Over the past decade, interferometric synthetic aperture radar (InSAR) has proven itself to be a powerful tool for studying earth processes such as volcano deformation, tectonic deformation, and land subsidence [for references see *Massonnet and Feigl*, 1998; *Bürgmann et al.*, 2000a]. InSAR provides a spatially continuous observation of the change in range between the satellite and the ground over the time period of the interferogram [*Gabriel et al.*, 1989]. Crustal deformation data are often interpreted under the assumption of constant deformation rates due to limitations of sparsely sampled data sets, such as campaign GPS data. However, the deformation signal for many interesting phenomena is time-dependent. Transient relaxation processes following large earthquakes produce surface displacements

that decay non-linearly with time. Deformation arising from volcanic inflation can be spatially and temporally variable and the observation of this complexity can provide valuable insight into the rate of fluid or magma movement within the subsurface. Aseismic surface creep and slow earthquakes are additional examples of transient processes that are best resolved using data sets with high spatial and temporal resolution.

InSAR has the potential to resolve spatially and temporally complex deformation especially if redundant data can be used to separate the desirable deformation signal from noise and other artifacts, such as atmospheric delays [e.g., *Sandwell et al.*, 1998; *Zebker et al.*, 1997]. Many regions of study are affected by more than one deformation process, such as land subsidence resulting from ground water pumping in combination with tectonic deformation, which can complicate the interpretation of individual interferograms [*Watson et al.*, 2002; *Bawden et al.*, 2001]. The analysis of individual interferograms can be further complicated by the presence of non-deformation artifacts such as orbital, atmospheric, or processing errors. Since standard statistical techniques, such as stacking, are not suitable to resolve non-linear deformation, new techniques to synthesize multiple interferograms must be developed. Recent studies have attempted to extract temporal information by utilizing the growing catalogue of available SAR scenes collected by the Earth Remote Sensing spacecraft (ERS-1 and ERS-2) of the European Space Agency (ESA) [e.g., *Lanari et al.*, 2002; *Beauducel et al.*, 2000; *Ferretti et al.*, 2001]. A methodology for exploiting a large data set of differential interferograms is presented. Using a linear inversion scheme, a crustal deformation time series is extracted from a data set consisting of 115 differential interferograms of the Santa Clara valley located in the San Francisco Bay Area (Figure 1.1).

By comparing the result with other geodetic measurements, it is demonstrated how InSAR can be a powerful tool to image time-dependent, nonlinear processes.

1.2   InSAR Processing Procedure

Interferograms are produced using the Repeat Orbit Interferometry Package (ROI PAC) developed at JPL/Caltech. SAR data are processed using 8 looks in range and 40 looks in azimuth which results in pixel widths of roughly 150 m. A weighted power spectral density filter and an adaptive filter are applied to each interferogram [*Goldstein and Werner*, 1998]. Processing parameters were chosen to counter temporal decorrelation in those interferograms spanning several years while maximizing resolution. Topography is removed using a 30 m U.S. Geological Survey (USGS) Digital Elevation Model (DEM). Results from the Shuttle Radar Topography Mapping (SRTM) mission were not available at the time that the interferograms were processed. Upon the recent release of the SRTM data a comparison was performed with the USGS DEM. A 50-km-wavelength signal with a maximum peak-to-trough amplitude of 2.7 m was found in the residual between elevation models for the flat, urban regions of the Bay Area. However the analysis of tandem ERS InSAR data (one-day interferograms) suggests that this anomalous signal originates from the SRTM data set. A 2.7 m elevation change would translate to ∼1 mm in range change for a perpendicular baseline of 100 m.

Orbital errors result in near-linear gradients across an interferogram. Precise Orbit Products provided by the European Space Agency (ESA) are used as the initial parameters when calculating the orbital baseline. A regional gradient associated with the interseismic
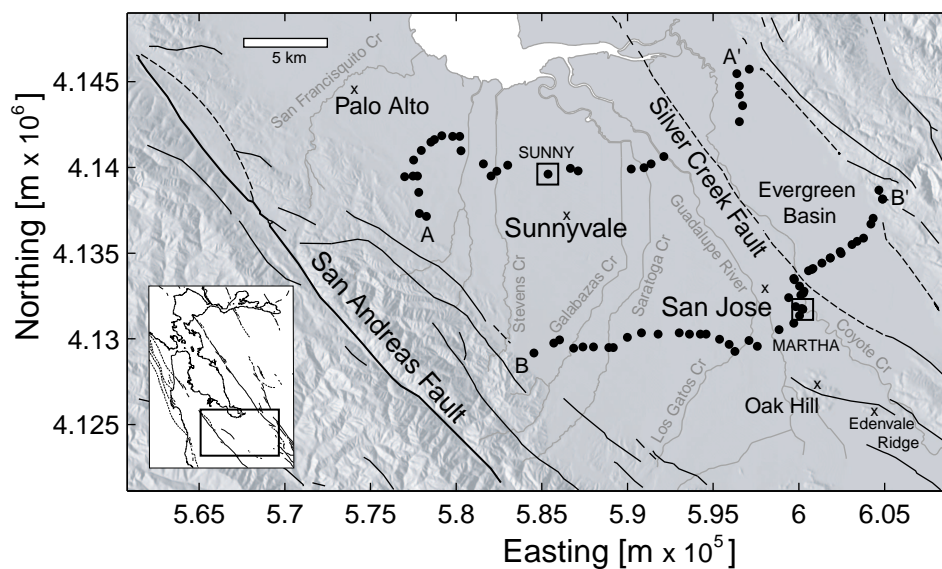
Figure 1.1: A shaded relief map of the Santa Clara valley is shown with benchmark locations along two leveling lines (dots), extensometer sites (open squares), and major cities or other significant locations (x). All InSAR observations are referenced to Oak Hill. Quaternary faults appear as bold lines, dashed where inferred [*Jennings*, 1994]. Major drainage channels appear as gray lines.

strain field across the Bay Area is removed using a dislocation model derived from available GPS data presented in *Bürgmann et al.* [2000b]. Regions of isolated, coherent data are connected by manually estimating the number of wavelength cycles represented by the deformation field before an automated algorithm unwraps the phase. Orbital baseline values are then re-estimated using the flattened interferogram and the interseismic gradient is added back to the interferogram. Finally, the interferograms are geo-referenced to the USGS DEM.

1.3   Time Series Inversion Methodology

A range-change time series is determined by performing a least squares inversion from the differential interferograms. Interferograms are co-located and of identical dimensions. The notation for the discussion that follows can be found in Table 1.1. The range-change data are contained in Γ_{ijk}, where i and j are the pixel coordinates of the kth interferogram, and N interferograms are created from S independent SAR scenes. The range change in each interferogram is referenced to a common pixel (i_r, j_r) to ensure that all deformation is measured relative to a common location,

$$\mathbf{I}_{ijk} = \mathbf{\Gamma}_{ijk} - \mathbf{\Gamma}_{i_r j_r k}. \tag{1.1}$$

The dates of the SAR scenes are contained in chronological order in the 1xS vector $\mathbf{L}$, and $\mathbf{T}$ is a 2xN array with the beginning and ending date for each interferogram ordered by the date of the first scene. Information about the temporal distribution of interferograms is included in the inversion through $\mathbf{H}$, where $\mathbf{H}$ is a Nx(S-1) matrix composed of ones and

zeros using the information in $\mathbf{T}$ and $\mathbf{L}$,

$$\mathbf{H}_{ij} = \begin{cases} 1 \text{ for } \mathbf{T}_{i1} \leq \mathbf{L}_j < \mathbf{T}_{i2} \\ \\ 0 \text{ for } \mathbf{T}_{i1} > \mathbf{L}_j \text{ or } \mathbf{L}_j \geq \mathbf{T}_{i2}. \end{cases} \tag{1.2}$$

The data kernel, $\mathbf{G}$, is constructed using $\mathbf{H}$, and the finite difference approximation of the Laplacian smoothing operator, ∇^2 [see *Harris and Segall*, 1987],

$$\mathbf{G} = \begin{bmatrix} \mathbf{H} \\ \gamma^2 \nabla^2 \end{bmatrix}. \tag{1.3}$$

The smoothing operator acts as a temporal rather than a spatial filter since the independent variable is time. The degree of smoothing is determined by the factor γ where $\gamma=0$ corresponds to no smoothing. The data vector, $\mathbf{d}$, consists of the relative range change in each interferogram for a given pixel *(i,j)*,

$$\mathbf{d}_k = \begin{bmatrix} \mathbf{I}_{ijk} \\ 0 \end{bmatrix}. \tag{1.4}$$

The relative range-change that occurs during each time step is contained in the model vector, $\mathbf{m}_k$, and is calculated using a least squares inversion where $\mathbf{m}_k = \mathbf{G}^{-g}\mathbf{d}_k$ [*Menke*, 1989]. Given the InSAR data that is available for most applications, this is a mixed-determined inverse problem performed for each pixel *(i,j)*. The generalized inverse, $\mathbf{G}^{-g}$, is calculated using singular value decomposition. The time series, $\mathbf{C}$, is constructed by summing the range change from preceding time steps,

$$\mathbf{C}_{ijk_f} = \sum_{k=1}^{k_f} \mathbf{m}_k. \tag{1.5}$$

The acquisition rate of SAR scenes dictates the temporal resolution of the final time series, while the number and distribution of interferograms determines the model and data resolution of the inversion. The inversion methodology results in a time series with an irregular

temporal sampling, since the date of each time step corresponds to the acquisition date of a SAR scene used to create the interferograms. The ERS spacecraft repeat their orbits every 35 days; however, longer gaps occur when acquisitions were not scheduled, orbit baselines were unsuitable, or the spacecraft orbital configuration was altered.

Interferograms are often plagued by atmospheric artifacts with complex spatial and temporal correlations [*Hanssen*, 2001; *Williams et al.*, 1998; *Zebker et al.*, 1997]. Any atmospheric signal resulting from the lateral heterogeneity of water vapor would ideally be estimated using *a priori* zenith delays determined from meteorological data or continuous GPS. Unfortunately, this information is not readily available at the required spatial or temporal resolution to be feasible for this study. Alternatively, an additional set of model parameters could be included in the inversion which represent the atmospheric signal associated with each SAR scene. This would make the inversion significantly underdetermined. For this analysis, any such signal is treated as uncorrelated noise, acknowledging that this signal is correlated among interferograms that share common SAR scenes. The estimated error for the time series, σ_c, is calculated assuming that the standard error of an interferogram, σ_d, is 4 mm,

$$\Sigma_m = \sigma_d{}^2 \mathbf{G}^{-\mathbf{g}} \mathbf{I} (\mathbf{G}^{-\mathbf{g}})^{\mathbf{T}}, \tag{1.6}$$

$$(\sigma_m)_i = \sqrt{(\Sigma_m)_{ii}}, \tag{1.7}$$

$$(\sigma_c)_i = \sqrt{\sum_{j=1}^{i} (\sigma_m)_j{}^2}. \tag{1.8}$$

A comparison of the time series result with existing data sets suggests that the propagated errors exceed the actual precision of the result. Other data analysis techniques, such as stacking, would produce smaller estimates of the error. A higher error estimate is expected

Table 1.1: Notation.

i_r, j_r	pixel reference location
u, v	number of pixels along the width and length of an interferogram
S	number of SAR scenes
N	number of interferograms in data set
$\mathbf{I}$	(u x v x N) array containing the range-change data
$\mathbf{L}$	(S x 1) vector with the dates of the SAR scenes
$\mathbf{T}$	(N x 2) array with the date of the first and second pass for each interferogram
$\mathbf{d}_k$	(S x 1) data vector containing the range-change for interferogram k at pixel (i,j)
$\mathbf{G}$	($N + S$ - 2 x S) data kernel
∇^2	(S - 2 x S) Laplacian smoothing operator
γ	smoothing factor
$\mathbf{m}_k$	(S x 1) model vector, incremental range-change between SAR acquisitions for pixel (i,j)
$\mathbf{C}$	(S x 1) cumulative time series at pixel (i,j)
σ_c	(S x 1) vector with the time series error at pixel (i,j)

because the time-dependent signal is not constrained to a linear or sinusoidal form. However, results are found to be consistent between time series and stacking approaches where such analysis is appropriate.

Typically, N, the number of interferograms, is significantly greater than S, the number of SAR scenes. As N approaches S, the inversion becomes less stable and it may become necessary to exclude those interferograms where a SAR scene is used only once. This helps to improve the model resolution matrix and stabilize the inversion at the expense of reducing the temporal resolution. At least 30 interferograms are required to produce a reasonable time series.

1.4   Results for the Santa Clara Valley

The time series inversion is demonstrated using SAR data from the San Francisco Bay Area. Surface deformation in the region due to tectonic and non-tectonic processes has been monitored using terrestrial and space geodetic techniques [e.g., *Lisowski et al.*, 1991; *Lienkaemper and Galehouse*, 1997; *Bürgmann et al.*, 2000b]. Thus the InSAR time series can be compared directly to independent geodetic observations to evaluate its spatial and temporal accuracy. The time series methodology was developed to assist in the interpretation of complex deformation that occurs along active strike-slip faults [e.g. *Bürgmann et al.*, 2000b]. In the Bay region, the largest magnitude deformation signal is due to hydrologic, non-tectonic processes. The following analysis focuses on the Santa Clara valley since this region provides the best data set to evaluate the time series result. The Santa Clara Valley is a sedimentary basin whose stratigraphy forms a series of interbedded aquifers and aquitards

[*Clark*, 1924; *Iwamura*, 1995]. The primary confined aquifer is located at a depth interval of 60-300 m and consists of unconsolidated alluvium over the semi-consolidated alluvium of the plio-pleistocene Santa Clara formation. Consolidated bedrock of the Franciscan complex is found at greater depths.

Land uplift and subsidence in the valley due to the recharge and withdrawal of fluids is well documented by several public agencies such as the Santa Clara Valley Water District (SCVWD) and the USGS [see *Poland and Ireland*, 1988; *Poland and Davis*, 1969]. An increase in the withdrawal of water from the aquifer and a decrease in rainfall for the first half of the twentieth century resulted in a substantial drop in well levels and a corresponding land subsidence of ∼4 m. Recovery efforts over the past quarter century, such as the import of water from outside sources and the construction of percolation ponds, have allowed water levels to partially recover. Preservation of the aquifer requires the continual monitoring through extensometers, well water levels, and level line observations (Figure 1.1). Most of the initial subsidence was due to inelastic, unrecoverable consolidation of fine silts and clay layers. Some elastic rebound can be expected with the recovery of water levels. InSAR is an attractive method for monitoring land subsidence because of its spatial coverage and precision [*Massonnet et al.*, 1997; *Fielding et al.*, 1998; *Galloway et al.*, 1998; *Amelung et al.*, 1999; *Bawden et al.*, 2001; *Hoffmann et al.*, 2001]. However, individual interferograms are often difficult to interpret because the amount of deformation that is observed is highly dependent on the seasonal differences between the acquisition of the first and second SAR scenes. A time-series analysis has the potential to overcome this limitation by resolving the temporal variability of the surface deformation.

For the Santa Clara valley time series analysis, 115 interferograms are used in the inversion. The temporal distribution of interferograms used in the analysis is displayed in Figure 1.2. Interferograms used in the analysis are limited to those with small perpendicular baselines ($<$ 200 m) to ensure that errors imposed by topography remain small. SAR data were collected by the ERS1 and ERS2 satellites between April of 1992 and June of 2000 along two different orbital tracks. Track 70 is on a descending trajectory with the satellite moving from north to south and the antenna looking to the northwest (look azimuth $\approx$284°). Track 747 is on an ascending trajectory with the satellite moving from south to north looking to the northeast (look azimuth $\approx$76°). The ascending and descending geometries can be used to decipher vertical from horizontal deformation if one component of the three-dimensional deformation field can be independently constrained. While both ascending and descending data were included in the inversion, the vast majority of SAR data were collected along the descending trajectory (106 out of 115). Comparisons of the ascending and descending data suggest that the crustal deformation is predominately vertical. Therefore the range-change data are projected onto a vertical vector. The range-change in all interferograms is referenced to Oak Hill, an outcrop of consolidated bedrock located in the southern portion of the Santa Clara valley [*Wentworth et al.*, 1999]. It is assumed that this point is less susceptible to the ground-water-controlled deformation. A comparison of the time series result with individual interferograms illustrates the ability of the time series to fit the original data (Figure 1.3).

The InSAR time series reveals an overall pattern of uplift since 1992 (Figure 1.4a). The uplift is attributed to an increase in the ground water levels. The increase in pore
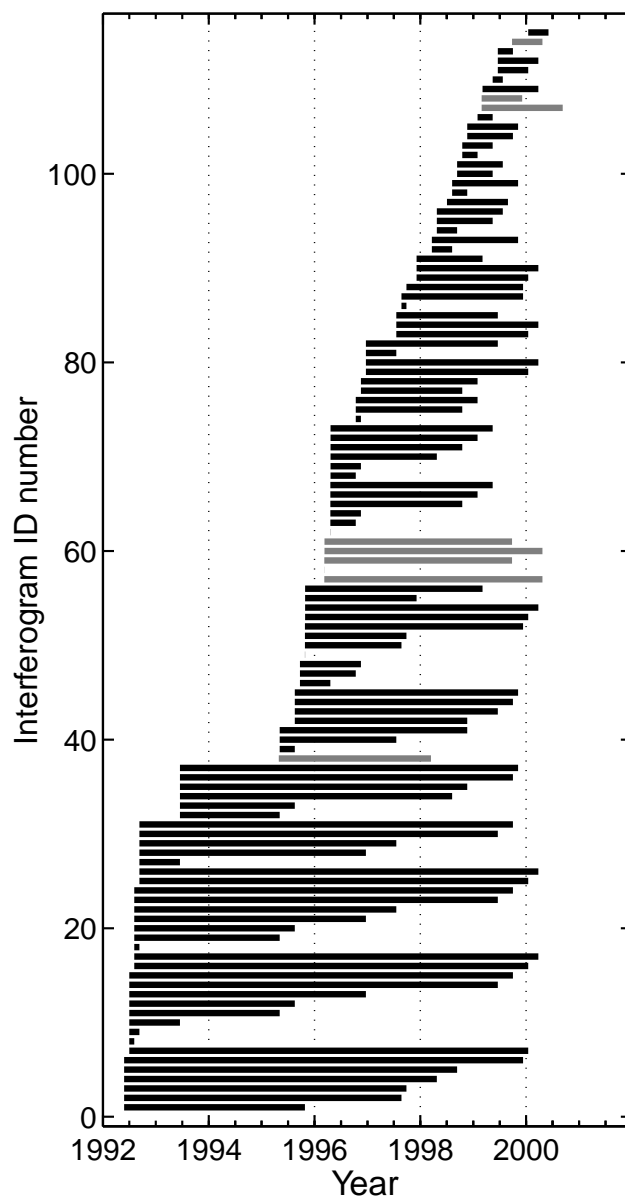
Figure 1.2: The chart shows the temporal distribution of interferograms with perpendicular baselines of less than 200 m used in the analysis for the Santa Clara valley. These include all data acquired by the ERS1/2 spacecraft from April of 1992 to June of 2000 along tracks 478(gray horizontal bars) and 70(black horizontal bars). A complete list of interferograms can be found in Table 1.2.

Table 1.2: List of interferograms used in the analysis of the Santa Clara valley.

| Date1 | Date2 | Track | Sat 1 | Orbit 1 | Sat 2 | Orbit 2 | Perp. | Δt |
YYYYMMDD	YYYYMMDD						Base. (m)	(yr)
19920610	19951110	70	ERS1	4724	ERS1	22603	36	3.4
19920610	19970906	70	ERS1	4724	ERS2	12449	4	5.2
19920610	19971011	70	ERS1	4724	ERS2	12950	3	5.4
19920610	19980509	70	ERS1	4724	ERS2	15956	181	5.9
19920610	19980926	70	ERS1	4724	ERS2	17960	172	6.3
19920610	19991225	70	ERS1	4724	ERS2	24473	71	7.5
19920715	19000129	70	ERS1	5225	ERS2	24974	104	7.5
19920715	19920819	70	ERS1	5225	ERS1	5726	61	0.1
19920715	19920923	70	ERS1	5225	ERS1	6227	23	0.2
19920715	19930630	70	ERS1	5225	ERS1	10236	172	1.0
19920715	19950519	70	ERS1	5225	ERS1	20098	66	2.8
19920715	19950901	70	ERS1	5225	ERS1	21601	92	3.1
19920715	19970104	70	ERS1	5225	ERS2	8942	76	4.5
19920715	19990703	70	ERS1	5225	ERS2	21968	48	7.0
19920715	19991016	70	ERS1	5225	ERS2	23471	77	7.3
19920819	20000129	70	ERS1	5726	ERS2	24974	43	7.4
19920819	20000408	70	ERS1	5726	ERS2	25976	107	7.6
19920819	19920923	70	ERS1	5726	ERS1	6227	38	0.1
19920819	19950519	70	ERS1	5726	ERS1	20098	127	2.7
19920819	19950901	70	ERS1	5726	ERS1	21601	153	3.0
19920819	19970104	70	ERS1	5726	ERS2	8942	15	4.4
19920819	19970802	70	ERS1	5726	ERS2	11948	13	5.0
19920819	19990703	70	ERS1	5726	ERS2	21968	13	6.9
19920819	19991016	70	ERS1	5726	ERS2	23471	138	7.2
19920923	20000129	70	ERS1	6227	ERS2	24974	81	7.3
19920923	20000408	70	ERS1	6227	ERS2	25976	145	7.5
19920923	19930630	70	ERS1	6227	ERS1	10236	195	0.8
19920923	19970104	70	ERS1	6227	ERS2	8942	53	4.3
19920923	19970802	70	ERS1	6227	ERS2	11948	51	4.9
19920923	19990703	70	ERS1	6227	ERS2	21968	25	6.8
19920923	19991016	70	ERS1	6227	ERS2	23471	100	7.0
19930630	19950519	70	ERS1	10236	ERS1	20098	106	1.9
19930630	19950901	70	ERS1	10236	ERS1	21601	80	2.2
19930630	19980822	70	ERS1	10236	ERS2	17459	81	5.1
19930630	19981205	70	ERS1	10236	ERS2	18962	4	5.4
19930630	19991016	70	ERS1	10236	ERS2	23471	95	6.3
19930630	19991120	70	ERS1	10236	ERS2	23972	73	6.4
19950513	19980329	478	ERS1	20005	ERS2	15362	95	2.8
19950519	19950901	70	ERS1	20098	ERS1	21601	26	0.3

Table 1.2: Continued.

Date1 YYYYMMDD	Date2 YYYYMMDD	Track	Sat 1	Orbit 1	Sat 2	Orbit 2	Perp. Base. (m)	Δt (yr)
19950519	19970802	70	ERS1	20098	ERS2	11948	140	2.2
19950519	19981205	70	ERS1	20098	ERS2	18962	102	3.5
19950901	19981205	70	ERS1	21601	ERS2	18962	76	3.3
19950901	19990703	70	ERS1	21601	ERS2	21968	140	3.8
19950901	19991016	70	ERS1	21601	ERS2	23471	15	4.1
19950901	19991120	70	ERS1	21601	ERS2	23972	153	4.2
19951007	19960503	70	ERS2	2429	ERS1	25108	124	0.6
19951007	19961026	70	ERS2	2429	ERS2	7940	68	1.1
19951007	19961130	70	ERS2	2429	ERS2	8441	66	1.1
19951110	19951111	70	ERS1	22603	ERS2	2930	268	0.0
19951110	19970906	70	ERS1	22603	ERS2	12449	40	1.8
19951110	19971011	70	ERS1	22603	ERS2	12950	33	1.9
19951110	19991225	70	ERS1	22603	ERS2	24473	35	4.1
19951111	20000129	70	ERS2	2930	ERS2	24974	152	4.2
19951111	20000408	70	ERS2	2930	ERS2	25976	88	4.4
19951111	19971220	70	ERS2	2930	ERS2	13952	23	2.1
19951111	19990320	70	ERS2	2930	ERS2	20465	44	3.4
19960323	20000507	478	ERS1	24514	ERS2	26384	58	4.1
19960323	19960324	478	ERS1	24514	ERS2	4841	134	0.0
19960323	19991010	478	ERS1	24514	ERS2	23378	14	3.5
19960324	20000507	478	ERS2	4841	ERS2	26384	192	4.1
19960324	19991010	478	ERS2	4841	ERS2	23378	120	3.5
19960503	19960504	70	ERS1	25108	ERS2	5435	90	0.0
19960503	19961026	70	ERS1	25108	ERS2	7940	56	0.5
19960503	19961130	70	ERS1	25108	ERS2	8441	58	0.6
19960503	19981031	70	ERS1	25108	ERS2	18461	53	2.5
19960503	19990213	70	ERS1	25108	ERS2	19964	24	2.8
19960503	19990529	70	ERS1	25108	ERS2	21467	126	3.1
19960504	19961026	70	ERS2	5435	ERS2	7940	146	0.5
19960504	19961130	70	ERS2	5435	ERS2	8441	148	0.6
19960504	19980509	70	ERS2	5435	ERS2	15956	152	2.0
19960504	19981031	70	ERS2	5435	ERS2	18461	37	2.5
19960504	19990213	70	ERS2	5435	ERS2	19964	66	2.8
19960504	19990529	70	ERS2	5435	ERS2	21467	36	3.1
19961026	19961130	70	ERS2	7940	ERS2	8441	140	0.1
19961026	19981031	70	ERS2	7940	ERS2	18461	109	2.0
19961026	19990213	70	ERS2	7940	ERS2	19964	80	2.3
19961130	19981031	70	ERS2	8441	ERS2	18461	111	1.9
19961130	19990213	70	ERS2	8441	ERS2	19964	82	2.2

Table 1.2: Continued.

| Date1 | Date2 | Track | Sat 1 | Orbit 1 | Sat 2 | Orbit 2 | Perp. | Δt |
YYYYMMDD	YYYYMMDD						Base. (m)	(yr)
19970104	20000129	70	ERS2	8942	ERS2	24974	28	3.1
19970104	20000408	70	ERS2	8942	ERS2	25976	92	3.3
19970104	19970802	70	ERS2	8942	ERS2	11948	2	0.6
19970104	19990703	70	ERS2	8942	ERS2	21968	28	2.5
19970802	20000129	70	ERS2	11948	ERS2	24974	30	2.5
19970802	20000408	70	ERS2	11948	ERS2	25976	94	2.7
19970802	19990703	70	ERS2	11948	ERS2	21968	26	1.9
19970906	19971011	70	ERS2	12449	ERS2	12950	7	0.1
19970906	19991225	70	ERS2	12449	ERS2	24473	75	2.3
19971011	19991225	70	ERS2	12950	ERS2	24473	68	2.2
19971220	20000129	70	ERS2	13952	ERS2	24974	129	2.1
19971220	20000408	70	ERS2	13952	ERS2	25976	65	2.3
19971220	19990320	70	ERS2	13952	ERS2	20465	67	1.2
19980404	19980822	70	ERS2	15455	ERS2	17459	100	0.4
19980404	19991120	70	ERS2	15455	ERS2	23972	108	1.6
19980509	19980926	70	ERS2	15956	ERS2	17960	9	0.4
19980509	19990529	70	ERS2	15956	ERS2	21467	116	1.1
19980509	19990807	70	ERS2	15956	ERS2	22469	25	1.2
19980718	19990911	70	ERS2	16958	ERS2	22970	84	1.1
19980822	19981205	70	ERS2	17459	ERS2	18962	85	0.3
19980822	19991120	70	ERS2	17459	ERS2	23972	8	1.2
19980926	19990529	70	ERS2	17960	ERS2	21467	125	0.7
19980926	19990807	70	ERS2	17960	ERS2	22469	34	0.9
19981031	19990213	70	ERS2	18461	ERS2	19964	29	0.3
19981031	19990529	70	ERS2	18461	ERS2	21467	73	0.6
19981205	19991016	70	ERS2	18962	ERS2	23471	91	0.9
19981205	19991120	70	ERS2	18962	ERS2	23972	77	1.0
19990213	19990529	70	ERS2	19964	ERS2	21467	102	0.3
19990314	20000924	478	ERS2	20372	ERS2	28388	108	1.5
19990314	19991219	478	ERS2	20372	ERS2	24380	109	0.7
19990320	20000408	70	ERS2	20465	ERS2	25976	132	1.1
19990529	19990807	70	ERS2	21467	ERS2	22469	91	0.2
19990703	20000129	70	ERS2	21968	ERS2	24974	56	0.6
19990703	19000408	70	ERS2	21968	ERS2	25976	120	0.8
19990703	19991016	70	ERS2	21968	ERS2	23471	125	0.3
19991010	20000507	478	ERS2	23378	ERS2	26384	72	0.5
20000129	20000617	70	ERS2	24974	ERS2	26978	57	0.4
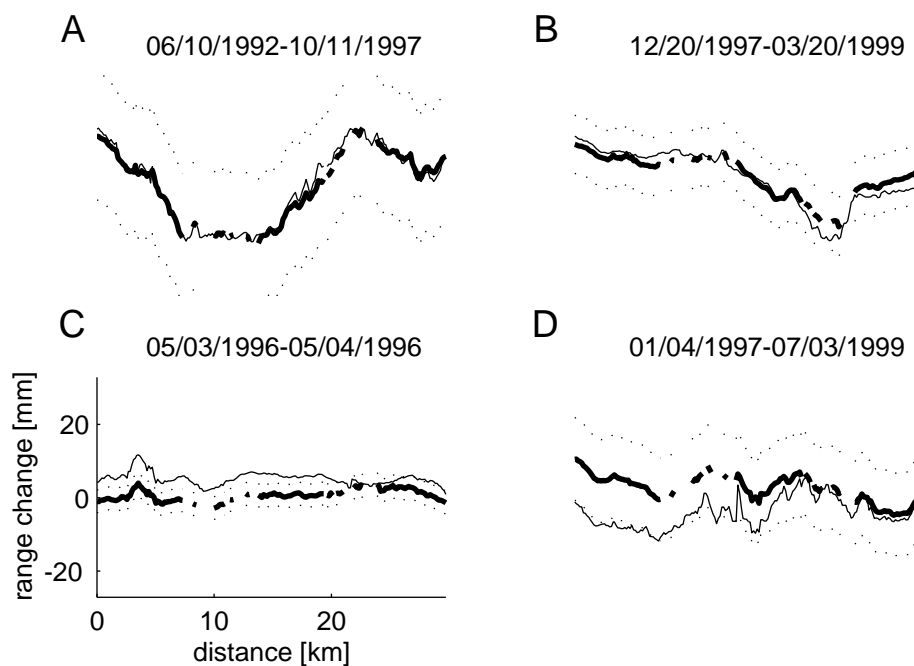
Figure 1.3: Profiles through the InSAR time series (heavy solid line) with error envelope (dotted lines) are compared to the range change for individual interferograms (thinner solid line) spanning the respective time interval. These plots provide a representative illustration of how closely the inversion reproduces the original InSAR data. The profiles are plotted along the upper west-east level line path A-A' in Figure 1.1. The time period for each interferogram is displayed above the profile. Most of the interferograms are fully reproduced as in (A and B). Several profiles show constant offsets or gradients between the interferograms and time series (C and D). These gradients are attributed to orbital or long-wavelength atmospheric artifacts that are reduced by the inversion.

pressure reduces the vertical effective stress on the skeletal matrix resulting in regional uplift. As much as 41±18 mm of uplift centered north of Sunnyvale is observed(see Figure 1.1 for location). Most of this uplift took place between 1992 and 1998 with a mean uplift rate of 6.4±2.2 mm/yr. Uplift is also observed in the Evergreen Basin located in the eastern portion of the Santa Clara valley. Significant subsidence relative to Oak Hill is also observed along the western margin of the valley. The southwestern portion of the valley shows insignificant uplift with no distinctive pattern. Continual uplift extends along several major tributaries, especially along Garabazas and Saratoga creeks.

The time series analysis also resolves a seasonal uplift pattern with the largest magnitude centered near San Jose (Figure 1.4b). The seasonal signal is sharply bounded on the east by a structure that aligns with the northward extension of the Silver Creek fault [*Ikehara et al.*, 1998]. Both ascending and descending interferograms show consistent deformation across this fault suggesting that the relative motion is vertical and not related to strike-slip fault motion. The fault appears as a sharp discontinuity in the deformation field of several interferograms that can be explained by differential subsidence across the structure. The Guadalupe river and Coyote creek delineate the west and east bounds of the seasonal deformation north of San Jose suggesting that the feature has some relationship with the drainage pattern. A seasonal subsidence pattern is also observed in the northwest portion of the region, however this signal is more complex and difficult to characterize.

1.4.1   Evaluation of Spatial Accuracy

To evaluate the spatial accuracy of the InSAR time series, results are compared with elevation changes measured using spirit leveling. Level line data were collected in the
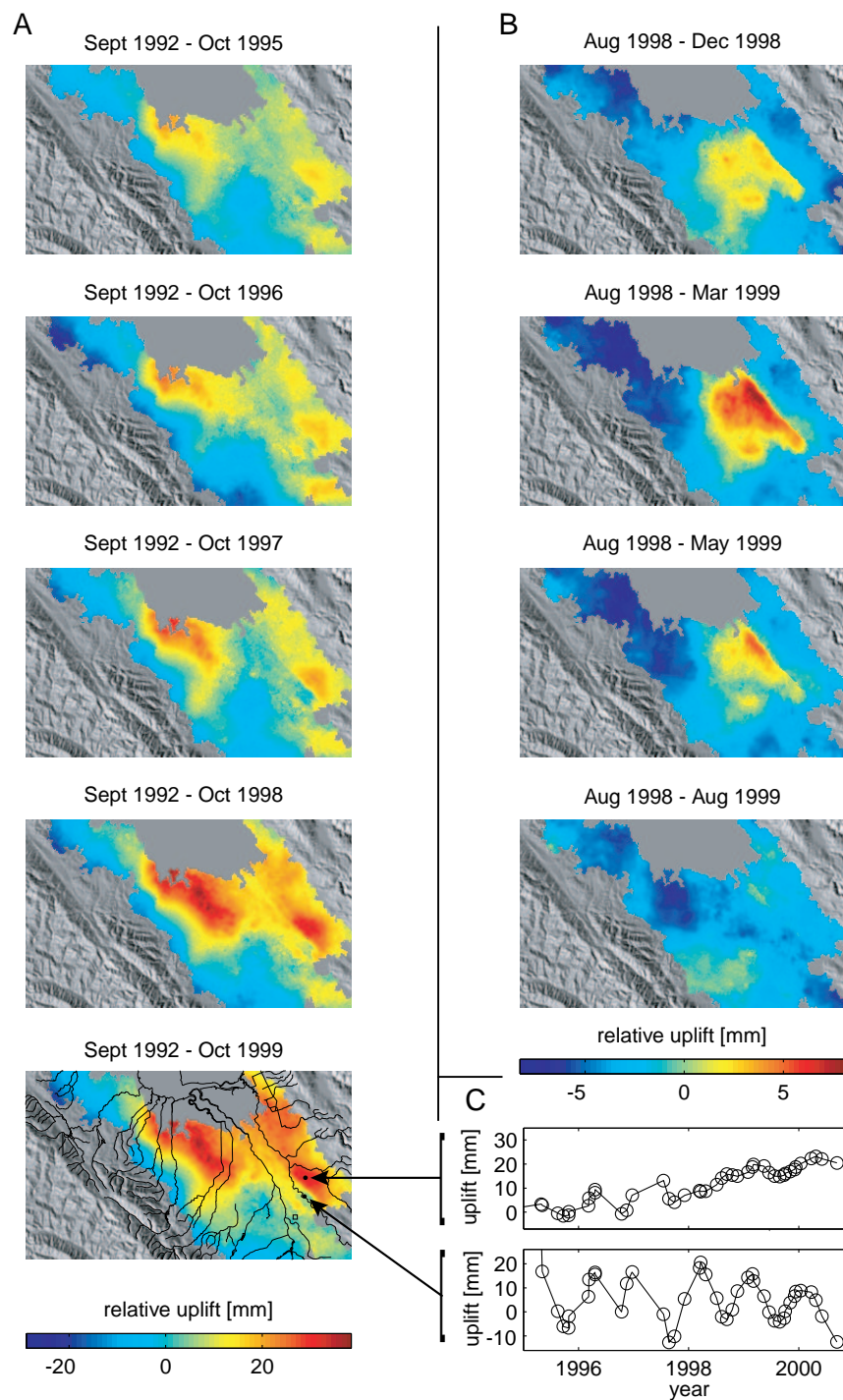
Figure 1.4: (A) Five frames from the InSAR time series show the pattern of net uplift since September of 1992. Uplift is centered north of Sunnyvale and east of the Silver Creek fault in the Evergreen Basin. Uplift is relative to Oak Hill (open square in final frame). The drainage network for the Santa Clara valley is also shown in the final frame. (B) The seasonal uplift pattern during a period from August of 1998 through August of 1999. (C) Time series at two points (dots in final frame of A) are compared to illustrate the seasonal versus long term deformation pattern. The points are separated by the Silver Creek fault which partitions the aquifer.

valley beginning in 1912 [*Poland and Ireland*, 1988]. Since 1989 the SCVWD performed yearly field observations along west-east and north-south profiles across the valley (Figure 1.1). In 1999 a new leveling route was added running west-east across the southern half of the valley and observations were increased to bi-yearly sampling. Cumulative deformation along each level line is compared to profiles across the InSAR time series (Figure 1.5). The shape of the profiles agrees well except for significant discrepancy between kilometers 0 to 5 in Figure 1.5b. Differences between the InSAR time series and the level data may reflect (1) additional subsidence during the time from when the level data was collected and when the SAR data was acquired, (2) artifacts in the InSAR data, or (3) propagating errors along the leveling line. Benchmarks in the leveling line may also experience benchmark instability that occurs in a region smaller than the spatial resolution of the interferogram.

1.4.2   Evaluation of Temporal Accuracy

Extensometers were installed in the valley by the USGS in the early 1960s to measure the compaction of sediments in the basin [*Lofgren*, 1961]. The SCWD currently maintains extensometers at SUNNY and MARTHA which are anchored at a depth of 306 and 183 m, respectively (see Figure 1.1 for location). The temporal signal of the time series can be evaluated by comparing the compaction measured by the extensometers and uplift history provided by the InSAR time series. Both the trend and the magnitude of the seasonal oscillation agree between the two data sets (Figure 1.6, a-b). The agreement between the extensometer and InSAR results suggests that all seasonal deformation is confined within the depth range of the extensometer boreholes and can be attributed to the compaction (or expansion) of the sediments.
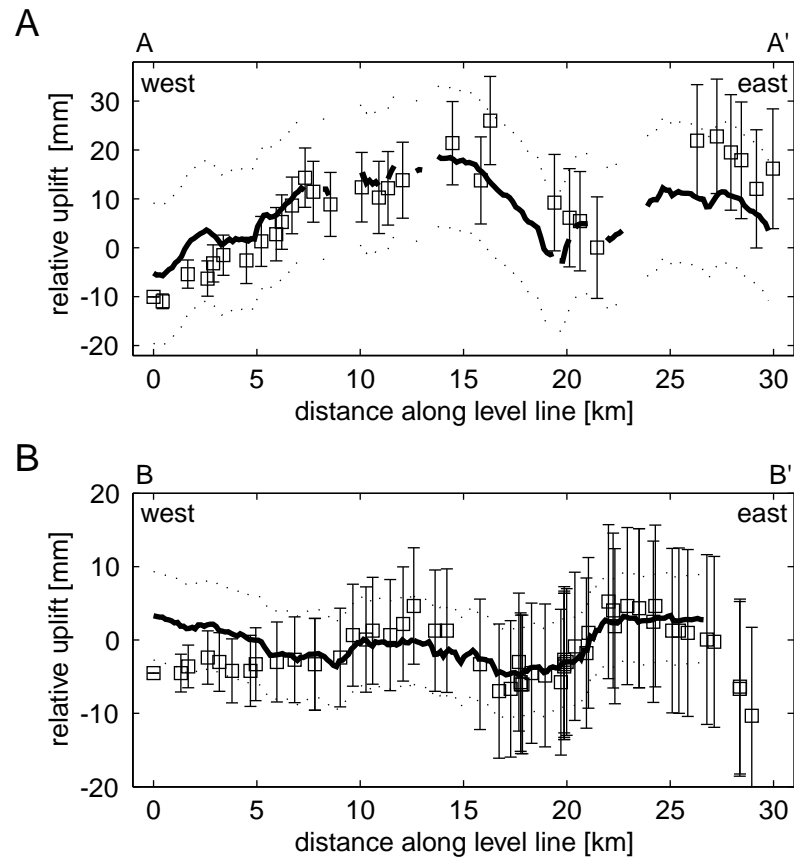
Figure 1.5: Level line data (open squares with error bars) are shown along two paths: (A) elevation change from April of 1995 to April of 1998 along a west to east path from Los Altos to Milpitas (A-A' in Figure 1.1), and (B) elevation change from April of 1999 to April of 2000 along a west to east path from Los Gatos to Alum Rock (B-B' in Figure 1.1). Profiles through the InSAR time series (solid line) show uplift relative to Oak Hill during similar time periods. Since a common vertical reference does not exist for both data sets, the level line data is arbitrarily shifted vertically so that the profiles can be compared to the InSAR data. Errors in elevation change relative to the western most benchmark accumulate along the leveling line according to 2.24 mm/$\sqrt{km}$. Gaps in the InSAR profile reflect regions where the phase is incoherent and, therefore, no data is available. The maximum change in topography (not shown) across the valley is 70 m and most of this change is located near the edges of the valley.
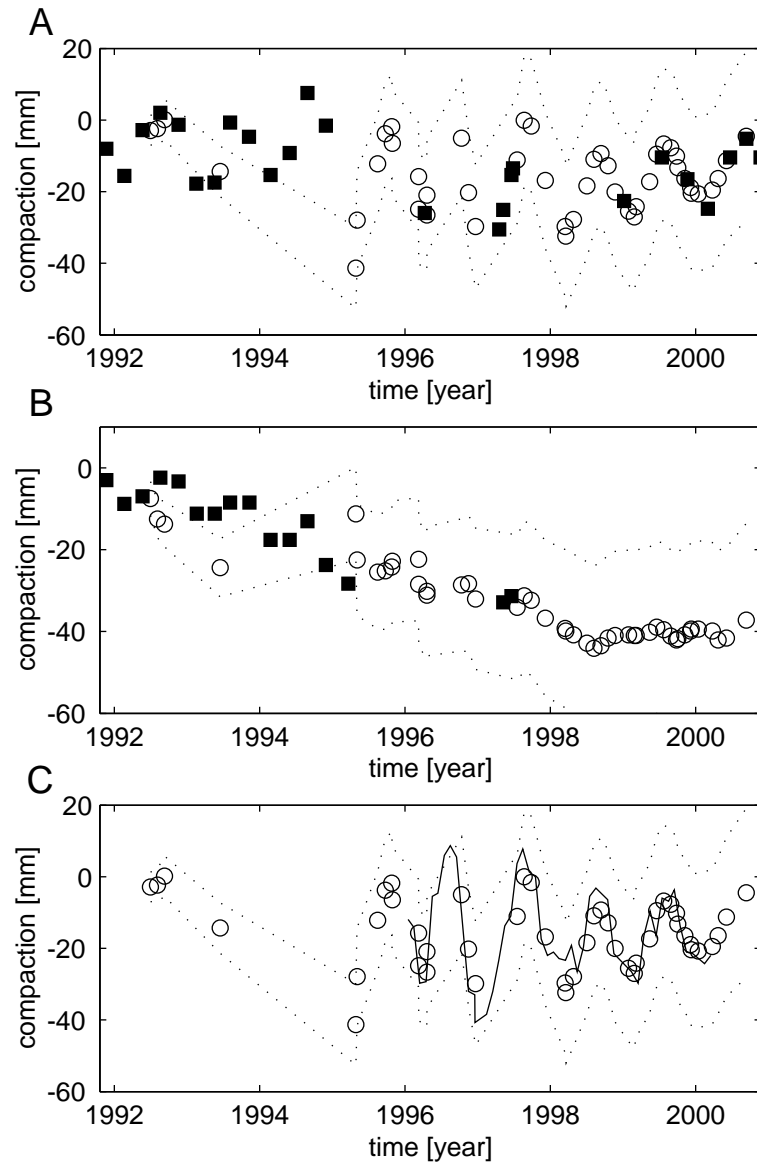
Figure 1.6: Extensometer observations (solid squares) are compared to vertical surface displacements observed from the InSAR time series (circles) with its associated error envelope (dotted lines) for the (A) MARTHA and (B) SUNNY instruments. (C) The InSAR time series is compared to well level depths that have been converted to compaction using the relationship discussed in Section 1.4.2 for a well adjacent to the MARTHA extensometer (well number 07S01E16C005, solid line). Well level data are collected approximately every month, providing a temporal resolution comparable to the InSAR time series.

Unfortunately, the extensometer data is not sampled as frequently as the InSAR data. Since the seasonal uplift is tied to the water level, the monthly fluctuations in the depth of water in wells are compared to vertical surface displacements. Well water levels and surface uplift are used to calculate the elastic skeletal storage coefficient, S_{ke}, for a given aquifer. The elastic skeletal storage coefficient describes the elastic response of the aquifer to a change in effective stress from the change in head, Δh, as measured by the change in water level found in wells [*Lohman*, 1961]. The change in water level is related to the change in compaction, Δb, according to $\Delta b = -\Delta h \times S_{ke}$. The InSAR time series is compared to the compaction calculated for a well located near San Jose using $S_{ke} = 1.5 \times 10^{-3}$ as determined by *Poland and Ireland* [1988] (Figure 1.6c). The inferred compaction and measured uplift signal are highly similar suggesting that the ongoing deformation is in the elastic regime.

1.5   Discussion

1.5.1   Reduction of InSAR Artifacts

Atmospheric heterogeneity is the most significant source of error when using In-SAR data to resolve crustal deformation [*Hanssen*, 2001]. The utilization of redundant data appears to be the best approach for minimizing these artifacts by allowing for the identification and exclusion of problematic scenes and averaging out uncorrelated errors [*Massonnet and Feigl*, 1998; *Sandwell and Price*, 1998]. To assess whether the time series inversion is successful at minimizing these artifacts, several sets of interferograms are examined that share a common SAR scene. The SAR scene acquired on October 26, 1996, provides a good illustration of an atmospheric disturbance (Figure 1.7). The apparent elevation change is

spatially correlated with a similar-magnitude range-change for all interferograms that share the common scene. The sign of the artifact flips depending on whether the scene is the first or second scene in the interferogram. While a signal associated with a single scene is in fact due to a sudden and completely reversed deformation event cannot be ruled out, temporal smoothing acts to reduce such excursions.

A direct inversion of the interferograms without imposing the smoothing constraint produces a time series that is rough and prone to sharp fluctuations from one time step to the next. However, the original interferograms are reproduced with very small residuals. Applying a temporal smoothing constraint significantly reduces the roughness at the expense of increasing the residuals (Figure 1.8). If the deformation signal is continuous and smooth given the temporal resolution of the time series, then the roughness ($\|\nabla^2 \mathbf{m}\|_2$) can be largely attributed to atmospheric errors (see Appendix A). Since deformation rates are not constant through time, solutions that are over-smoothed will begin to damp the time-varying deformation.

The choice of the smoothing weight, γ, is largely subjective. A cross-validation sum of squares (CVSS) as demonstrated by *Matthews and Segall* [1993] for determining the proper weight applied to the smoothing operator was attempted. The CVSS did not produce a minimum and therefore, did not constrain γ. A γ equal to 0.14 is chosen such that the residual sum of squares (RSS= $\|\mathbf{d} - \mathbf{Gm}\|_2$) is minimized while also minimizing any atmospheric artifacts that were identified through direct inspection of the interferograms. Auxiliary data sets, such as the extensometer and level line data in the Santa Clara valley, help to evaluate whether the model is over-smoothed. The smoothing parameter can also
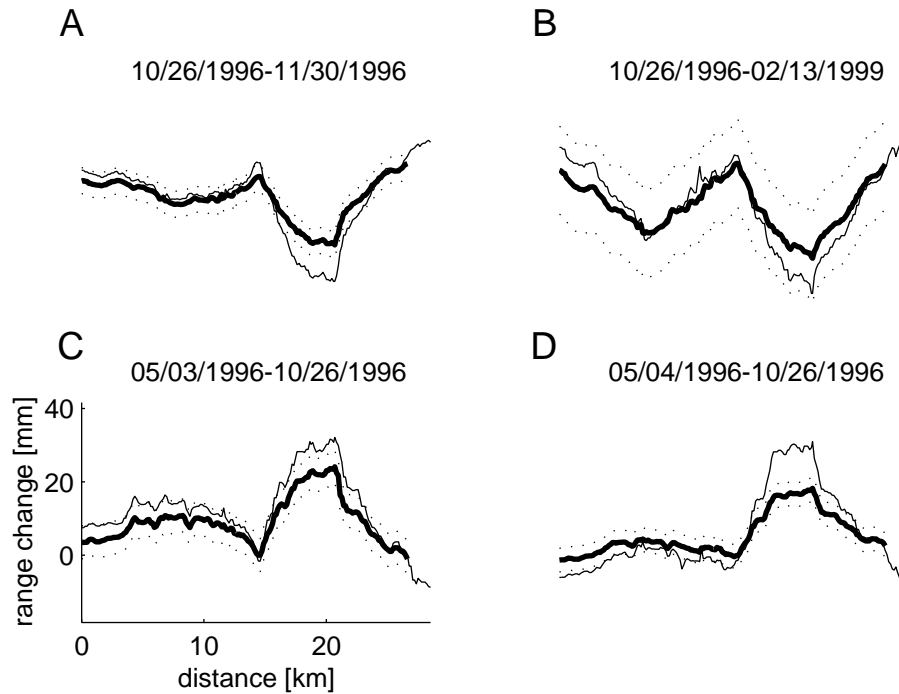
Figure 1.7: Profiles through the InSAR time series (heavy solid line) with error envelope (dotted lines) are compared to range change observations from the original interferograms (thinner solid line) along the lower west-east level line path B-B' (Figure 1.1). The time period for each interferogram is displayed above the profile. An atmospheric artifact that creates a range change delay of ∼10 mm is located at 20 km along the profile. The atmospheric delay occurs in the October 26, 1996, SAR acquisition and can be identified by examining those interferograms that use this SAR scene. Increasing the temporal smoothing parameter, γ, reduces this type of artifact.
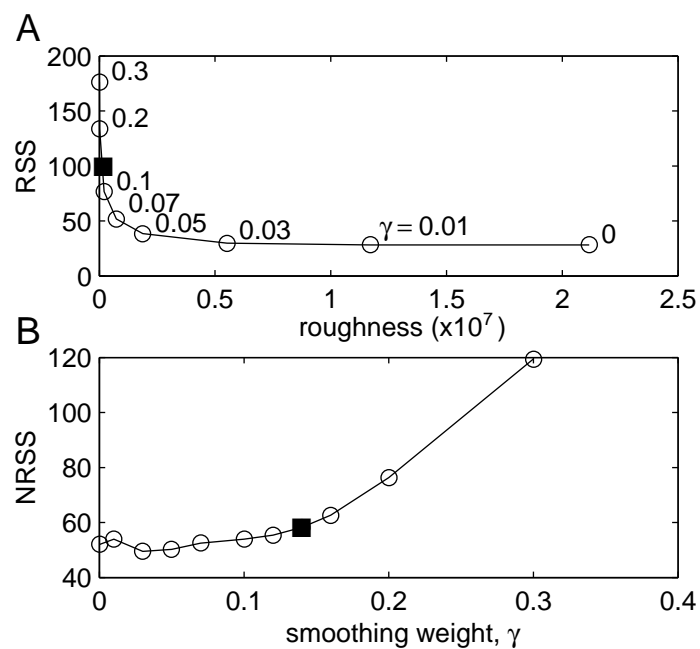
Figure 1.8: The value of the smoothing parameter, γ, is chosen by examining (A) the tradeoff between the residual sum of squares and the roughness, and (B) the increase in residual between the compaction data (Figure 1.6c) and the time series as a function of γ. Ultimately, (B) and the minimization of apparent atmospheric artifacts (see Figure 1.7) are used to choose a value of γ=0.14.

be evaluated by examining the trade-off curve between the RSS and the roughness of the model (Figure 1.8). A significant fraction of the roughness can be attributed to atmospheric artifacts which can produce a range-change of greater than 10 mm.

The time series methodology is unsuccessful at minimizing any systematic biases in the interferograms such as atmospheric delays that correlate with topography (for example, fog). As with any time series, a regular and dense sampling rate is required to fully characterize a non-linear signal. For example, the time series of the seasonal uplift near San Jose does not fully capture the large peak-to-trough amplitude of the compaction signal in the early part of 1997 because of the gap in available data (Figure 1.6c). The irregular acquisition of ERS1 and ERS2 data remains a limitation when performing a time-series analysis. Complementary data sets, such as continuous GPS sites [*Bawden et al.*, 2001], can provide valuable information between SAR scene acquisitions and help to calibrate the inversion when evaluating γ. Additionally, the ERS acquisitions largely consist of descending orbit data, limiting the potential for creating a separate time series of ascending SAR data to gain insight into the multi-dimensional displacement field.

1.5.2   Interpretation of Uplift and Subsidence Pattern

The spatial pattern of land subsidence observed during the first half of the twentieth century correlates with the overall uplift pattern observed from 1992 to 2000 (Figure 1.9a). From 1934 to 1960, maximum subsidence was centered north of Sunnyvale and in the region directly east of San Jose coincident with the seasonal deformation [*Poland and Ireland*, 1988; *Poland and Green*, 1962]. In the decade that followed, subsidence continued in the vicinity of San Jose. It is unclear why early level line studies did not observe the sharp

signal across the Silver Creek fault or significant deformation to the east. However, early leveling surveys likely did not have the temporal resolution to observe seasonal patterns.

The distribution of water bearing units suggests that the aquifer can be divided into two lateral hydrogeologic units: the forebay and the confined zone [*Iwamura*, 1995]. The forebay region includes the alluvial fans found along the perimeter of the valley where high, vertical permeabilities allow surface water to infiltrate the aquifer. Groundwater then flows horizontally into the confined zone, a region in the central part of the valley where water bearing units are capped by a thick layer of fine silts and clays. In the confined aquifer, different depositional environments associated with periods of low sea level produced interfingered beds of coarse and fine grained material. These low and high permeability units create a complex network where groundwater flows between units under different confining pressures.

The InSAR time-series results suggest that the confined region can be further subdivided into three domains based on the deformation pattern: two regions experiencing net uplift (1992-2000) centered in Sunnyvale and the Evergreen basin, and a central region dominated by seasonal deformation. The seasonal uplift is bounded on the west where the thickness of unconsolidated sediments decreases along the northwesterly-striking basement high extending from Edenvale Ridge and Oak Hill.

The magnitude of elastic rebound is expected to correlate with the thickness of unconsolidated alluvium, or the depth to basement assuming that Δh is translated to the full thickness. Unfortunately, the depth to basement is unconstrained for much of the valley; few of the wells reach consolidated bedrock. At several localities, such as in San Jose and

north of Sunnyvale, the depth to basement is believed to be in excess of 420 m [*Meade*, 1967; *California Department of Water Resources (CDWR)*, 1967]. Well data suggests that the depth to basement is highly variable throughout the San Francisco Bay region where faulting and erosion during periods of low sea level have created an irregular bedrock surface [*Atwater et al.*, 1977]. Deep sedimentary basins can be identified from the residual gravity field which reflects the heterogeneity in density of the upper crust. The isostatic residual gravity field of the bay region shows gravity lows along the east and west edges of the valley separated by a saddle located down the valley axis (Figure 1.9b) [*Roberts and Jachens*, 1993]. The saddle in the gravity field correlates with the seasonal deformation. The uplift observed north of Sunnyvale is not centered over the western gravity low. This suggests that the western low reflects the consolidated sediments of a Miocene basin [*Langenheim et al.*, 1997] which is not part of the aquifer system.

The thickness of the alluvium is not the only property of the aquifer that may control the elastic response. The heterogeneity of sediment type and the connectivity of permeable beds may also play a significant role. The effective time constants of flow depend on the thickness of interbeds and the vertical hydraulic diffusivity of aquitards [*Alley et al.*, 2002]. The petrology and grain size of sediments from well cores were catalogued in an effort to characterize the constituents of the aquifer system. *Meade* [1967] and *Johnson et al.* [1968] analyzed core samples from the Sunnyvale and San Jose extensometer sites. Fine sands and clays dominate the sediment found at the Sunnyvale site with grain sizes ranging from 0.001 to 0.2 mm. In San Jose, grain sizes were generally larger ranging from 0.004 to 1.5 mm with often abrupt transitions between fine and coarse deposits. Developing geologic
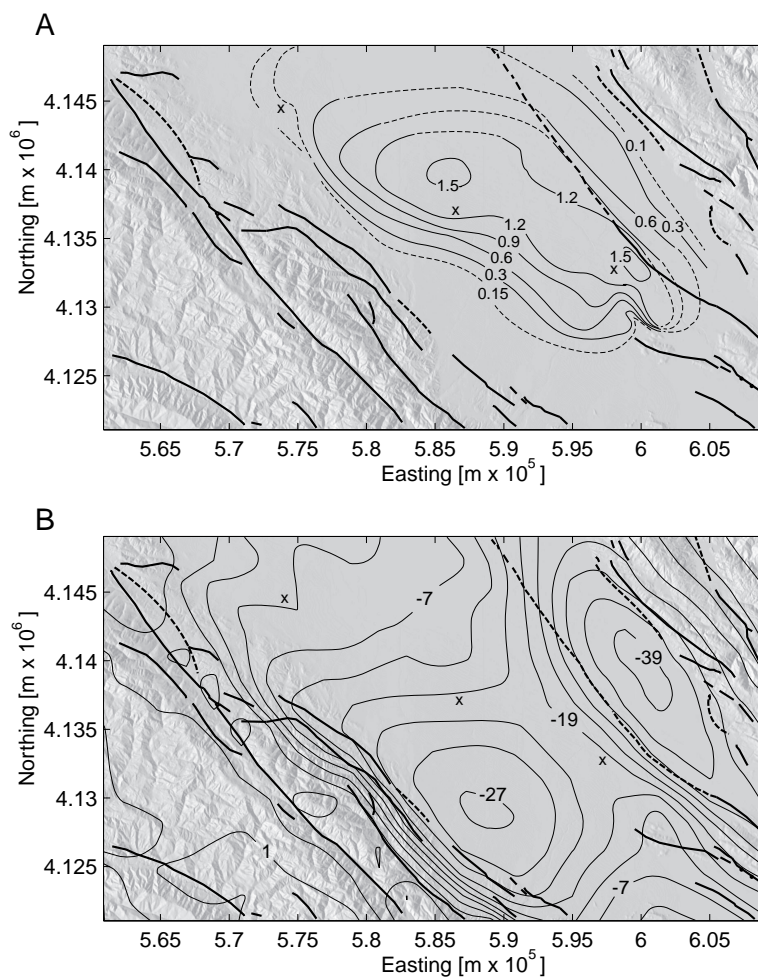
Figure 1.9: (A) Land subsidence observed from 1934 to 1960 is reproduced from *Poland and Ireland* [1988, Figure 19] using data collected by the National Geodetic Survey. Subsidence contours (thin lines, irregular intervals) are in units of m, dashed where poorly controlled. Regional faults and major cities are shown as in Figure 1.1. (B) The isostatic residual gravity field from *Roberts and Jachens* [1993] reflects basement structure. Gravity contour intervals (thin lines) are in 4 mgal units. A gravity low in the Evergreen Basin correlates with the secular uplift pattern. Seasonal uplift is centered over the saddle in the gravity field.

cross sections from well logs can be difficult because stratigraphic units may not correlate, especially if the units have an appreciable dip. *Johnson* [1995] used statistical correlations between well-perforation indicators to determine the lateral extent of water-bearing units. Coarse-grained units were found to be correlated over a wider area near San Jose than in Sunnyvale with an average bed thickness of 2.5 versus 1.3 m, respectively.

Despite the difficulty in correlating units from one well to the next, well log data and hydraulic head levels at different depths identified a sequence of productive water-bearing units identified as the Agnew aquifer [*CDWR*, 1967; *Johnson*, 1995]. The deposition of these units is associated with the ancestral drainage of the Coyote creek and the Guadalupe river, both of which transport sediment down the valley axis on the way to the bay [*Meade*, 1967; *CDWR*, 1967]. Seasonal uplift and subsidence shown in Figure 1.4b outlines a tabular region that broadens towards the north and may reflect the seasonal recharge of the Agnew aquifer. The InSAR data is not sufficient to resolve whether recharge has occurred in the shallow or deep sequence of the Agnew aquifer. The southern end of the seasonal uplift signal is co-located with the southernmost limit of the confined zone. Recharge of the basin is accommodated through the flow of subsurface water from the Coyote valley located to the south of the Santa Clara valley. Subsurface water flows through a narrow alluvial channel between Oak Hill and the Edenvale Ridge before cascading into the deeper aquifer [*CDWR*, 1967].

The long term uplift pattern also suggests that the permeable beds extend along stream channels to the west; however, these regions do not exhibit much seasonal deformation. The subsidence along the west side of the valley observed in Figure 1.4a outlines

the Santa Clara formation which is traditionally characterized as the recharge zone. The coarser sediment found in the San Jose well log implies higher hydraulic conductivities. The large seasonal uplift pattern in San Jose may be explained by a system where the seasonal influx of groundwater is redistributed over short periods of time. In contrast, the aquifer north of Sunnyvale and in the Evergreen basin may be characterized by lower hydraulic conductivities because of a greater percentage of fine sediment and clay layers resulting in the slow influx of groundwater into these parts of the aquifer.

The uplift pattern observed using the InSAR time series highlights the spatial complexity of the aquifer system in the Santa Clara valley. The temporal and spatial pattern of uplift and subsidence afforded by InSAR provides important constraints on the lateral distribution of water bearing units and the time scales over which the groundwater is exchanged. Ultimately, knowing the lateral extent and connectivity of water bearing units will improve numerical studies which attempt to model the mechanics of the aquifer system [for example, *Wilson and Gorelick*, 1996; *Leake*, 1990; *CDWR*, 1985; *Helm*, 1977].

1.5.3   The Silver Creek Fault

The unconsolidated alluvium conceals much of the fault network present in the Franciscan bedrock below the Santa Clara valley. The identification of these faults provides important information that could ultimately be used to evaluate the seismic hazard for the region [*Rogers and Williams*, 1974]. The Silver Creek fault represents one such structure that has received attention because it passes near downtown San Jose. The Silver Creek fault was originally identified as a west-dipping thrust fault separating geologic units of the Santa Clara Formation and the Franciscan Complex in exposed bedrock to the south.

Crittenden [1951] postulated that the fault continued beneath the alluvium to the north, although evidence indicating whether the fault has exhibited movement since the Holocene was inconclusive [*CDWR*, 1967; *Rogers and Williams*, 1974; *Bryant*, 1981; *Catchings et al.*, 2000]. The mapping of artesian head levels has long been known to be a useful way of identifying faults which partition hydrologic systems [*Tolman*, 1937]. However, the existence and location of the fault trace has been difficult to ascertain from hydrologic, geomorphic, or geophysical analyses. The fault trace is constrained within a 200-meter-wide zone where the deformation is localized. The zone of deformation is chosen by looking for inflection or knick points in the range-change profile. Deformation is evenly distributed within the zone, although discrete jumps in phase are observed at some locations.

The differential subsidence across the fault captured by InSAR provides important constraints on the maturity of the fault as well as its control on groundwater flow in the aquifer. Faults can act as low permeability barriers that retard fluid flow across the structure or they can act as conduits [*Caine et al.*, 1996]. The disparate uplift pattern across the Silver Creek fault suggests that it acts as a barrier. The fault may bisect sections of the Agnew aquifer and prevent recharge from the south or west. This can be accomplished either when lithologic units of different permeability are juxtaposed during faulting [e.g., *Maclay and Small*, 1983] or from the grain size reduction from shear in the fault core [*Teufel*, 1987]. Ultimately a geochemical analysis of the groundwater from both sides of the fault may be necessary to fully evaluate to what degree the aquifer is fully partitioned.

The development of the fault zone into a hydrologic barrier suggests that the fault has undergone significant slip since the deposition of the Quaternary alluvial units. Using

high-resolution gravity and magnetic data, *Jachens et al.* [2002] suggest that the Evergreen basin is formed from the extensional right-stepover between the northern extension of the Silver Creek fault and the southern extension of the Hayward fault. While the differential uplift across the fault could also be related to a distinct increase in alluvial thickness, the sharp lineament in the observed deformation argues for a fault zone that penetrates the alluvium.

1.6 Conclusions

It is demonstrated how a complex, time-dependent signal can be extracted from a large InSAR data set. In the Bay Area, long term as well as seasonal signals of crustal deformation are resolved. Vertical deformation in the Santa Clara valley is dominated by secular uplift north of Sunnyvale and in the Evergreen Basin, and a seasonal pattern of uplift and subsidence near San Jose. The Silver Creek fault is identified by differential subsidence distributed over a localized zone and may represent an important barrier in the hydrologic system. The deformation pattern can be used to constrain the temporal and spatial characteristics of the aquifer mechanics in the Santa Clara valley.

The time-series methodology does not parameterize the mode of deformation, whether it be linear, non-linear, or sinusoidal. The inversion also acts to reduce atmospheric and orbital artifacts inherent in each interferogram. InSAR time series can overcome many of the limitations encountered when working with individual interferograms. It provides an important tool that aids in the interpretation of complex deformation patterns with applications toward the study of tectonic, hydrologic, and volcanic systems.

1.7 Acknowledgements

Bibliography

Alley, W., Healy, R., LaBaugh, J. W., and T. E. Reilly, Flow and storage in groundwater systems, *Science, 296,* 1985-1990, 2002.

Amelung, F., Galloway, D.L., Bell, J.W., Zebker, H.A., and R. J. Laczniak, Sensing the ups and downs of Las Vegas–InSAR reveals structural control of land subsidence and aquifer-system deformation, *Geology, 27,* 483-486, 1999.

Atwater, B. F., Hedel C. W., and E. J. Helley, Late Quarternary depositional history, Holocene sea-level changes, and vertical crustal movement, southern San Francisco Bay, California, *U.S. Geol. Surv. Prof. Pap., 1014,* 1-15, 1977.

Bawden, G. W., Thatcher, W., Stein, R. S., Hudnut, K. W., and G. Peltzer, Tectonic contraction across Los Angeles after removal of ground water pumping effects, *Nature, 412,* 812-815, 2001.

Beauducel, F., Briole, P., and J. Froger, Volcano-wide fringes in ERS synthetic aperture radar interferograms of Etna (1992-1998): Deformation or tropospheric effect?, *J. Geophys. Res., 105,* 16,391-16,402, 2000.

Bryant, W. A., Southeast segment of Hayward, Evergreen, Quimby, Silver Creek, and Piercy fault, *Calif. Div. of Mines and Geology Fault Evaluation Report FER-106,* 20 pp., 1981.

Bürgmann, R., Rosen, P., and E. Fielding, Synthetic Aperture Radar Interferometry to measure earth's surface topography and its deformation, *Annu. Rev. Earth Planet. Sci., 28,* 169-209, 2000a.

Bürgmann, R., Schmidt, D., Nadeau,R. M., d'Alessio, M., Fielding, E., Manaker, D., McEvilly, T. V., and M. H. Murray, Earthquake potential along the northern Hayward fault, California, *Science, 289,* 1178-1182, 2000b.

Caine, J. S., Evans, J. P., and C. B. Foster, Fault zone architecture and permeability structure, *Geology, 24,* 1025-1028, 1996.

California Department of Water Resources, Reconnaissance investigation of ground water storage in Santa Clara valley to increase yield of the State Water Project, 308 pp., 1985.

California Department of Water Resources, Evaluation of groundwater resources, South San Francisco Bay, appendix A: Geology, Bulletin 118-1, 153 pp., 1967.

Catchings, R. D., Goldman, M. R., Gandhok, G., Rymer, M. J., and D. H. Underwood, Seismic imaging evidence for faulting across the northwestern projection of the Silver Creek fault, San Jose, California, *U.S. Geol. Surv. Open File Rep., 00-125*, 29 pp., 2000.

Clark, W. O., Ground water in Santa Clara valley, California, *U. S. Geol. Surv. Water-Supply Pap., 519*, 209 pp., 1924.

Crittenden, M. D., Geology of the San Jose-Mount Hamilton area, California, *Calif. Div. of Mines Bull., 157*, 1951.

Ferretti, A., Prati, C., and F. Rocca, Permanent scatterers in SAR interferometry, *IEEE T. Geosci. Remote, 39*, 1, 8-20, 2001.

Fielding, E. J., Blom, R. G., and R. M. Goldstein, Rapid subsidence over oil fields measured by SAR interferometry, *Geophys. Res. Lett., 25,* 3215-3218, 1998.

Gabriel, A. K., Goldstein, R. M., and H. A. Zebker, Mapping small elevation changes over large areas-differential radar interferometry, *J. Geophys. Res., 94,* 9183-9191, 1989.

Galloway, D.L., Hudnut, K.W., Ingebritsen, S.E., Phillips, S.P., Peltzer, G., Rogez, F., and P. A. Rosen, Detection of aquifer system compaction and land subsidence using interferometric synthetic aperture radar, Antelope valley, Mojave Desert, California, *Water Resour. Res., 34,* 2573-2585, 1998.

Goldstein, R. M., and C. L. Werner, Radar interferogram filtering for geophysical applications, *Geophys. Res. Lett., 25,* 4035-4038, 1998.

Harris, R. A., and P. Segall, Detection of a locked zone at depth on the Parkfield, California, segment of the San Andreas fault, *J. Geophys. Res., 92,* 7945-7962, 1987.

Hanssen, R. F., *Radar interferometry: data interpretation and error analysis,* Kluwer Academic, Boston, Ma., 308 pp., 2001.

Helm, D. C., Estimating parameters of compacting fine-grained interbeds within a confined aquifer system by a one-dimensional simulation of field observations, *International Symposium on Land Subsidence, 2d, Anaheim, California, December 1976, 121,* 145-156, 1977.

Hoffmann, J., Zebker, H., Galloway, D., and F. Amelung, Seasonal subsidence and rebound in Las Vegas valley, Nevada, observed by synthetic aperture radar interferometry, *Water Resour. Res., 37,* 1551-1566, 2001.

Ikehara, M. E., Galloway, D. L., Fielding, E., Bürgmann, R., Lewis, A. S., and B. Ahmadi, InSAR imagery reveals seasonal and longer-term land-surface elevation changes influenced by ground-water levels and fault alignment in Santa Clara valley, California, *EOS Trans. AGU,* 45, F37, 1998.

Iwamura, T. I., Hydrogeology of the Santa Clara and Coyote valleys ground water basins, California, *in* Sangines, E. S., Anderson, D. A., and A. V. Busing, Recent Geologic Studies in the San Francisco Bay Area, Pacific Section of the Society of Economic Paleontologists and Mineralogists, 76, 173-192, 1995.

Jachens, R. C., Wentworth, C. M., Graymer, R. M., McLaughlin, R. J., and F. C. Chuang, A 40-km-long concealed basin suggests large offset on the Silver Creek fault, Santa Clara valley, California, *Abstracts with Program, Geol. Soc. Am., Cordilleran Section, 98th Annual Meeting, Corvallis, Oregon,* 34(5), 99, 2002.

Johnson, N. M., Deterministic and stochastic approaches for evaluating multiple scales of Santa Clara valley hydrostratigraphy, *in* Sangines, E. S., Anderson, D. A., and A. V. Busing, Recent Geologic Studies in the San Francisco Bay Area, Pacific Section of the Society of Economic Paleontologists and Mineralogists, 76, 193-208, 1995.

Johnson, A. I., Moston, R. P., and D. A. Morris, Physical and hydrologic properties of water-bearing deposits in subsiding area in central California, *U.S. Geol. Surv. Prof. Pap., 497-A,* 71 pp., 1968.

Jennings, C. W., Fault activity map of California and adjacent areas: with locations and ages of recent volcanic eruptions, *Calif. Div. Of Mines and Geology,* map no. 6, 1:750,000, 1994.

Lanari, R., De Natale, G., Berardino, P., Sansosti, E., Ricciardi, G. P., Borgstrom, S., Capuano, P., Pingue, F., and C. Troise, Evidence for a peculiar style of ground deformation inferred at Vesuvius volcano, *Geophys. Res. Lett., 29(9),* 10.1029/2001GL014571, 2002.

Langenheim, V. E., Schmidt, K. M., and R. C. Jachens, Coseismic deformation during the 1989 Loma Prieta earthquake and range-front thrusting along the southwestern margin of the Santa Clara valley, California, *Geology, 25,* 1091-1094, 1997.

Leake, S. A, Interbed storage changes and compaction in models of regional groundwater flow, *Water Resour. Res., 26,* 1939-1950, 1990.

Lienkaemper, J., and J. Galehouse, Revised long-term creep rates on the Hayward fault, Alameda and Contra Costa Counties, California, *U.S. Geol. Surv. Open File Rep., 97-690,* 1997.

Lisowski, M., Savage, J. C., and W. H. Prescott, The velocity-field along the San-Andreas fault in central and southern California, *J. Geophys. Res., 96,* 8369-8389, 1991.

Lofgren, B. E., Measurement of compaction of aquifer systems in areas of land subsidence, *U.S. Geol. Surv. Prof. Pap., 424-B,* 49-52, 1961.

Lohman, S. W., Compression of elastic artesian aquifers, *U.S. Geol. Surv. Prof. Pap., 424-B,* 47-49, 1961.

Maclay, R. W., and T. A. Small, Hydrostratigraphic subdivisions and fault barriers of the Edwards Aquifer, south-central Texas, *J. Hydrol., 61,* 127-146, 1983.

Massonnet, D., and K. L. Feigl, Radar interferometry and its application to changes in the earth's surface, *Rev. Geophys., 36,* 441-500, 1998.

Massonnet, D., Holzer, T., and H. Vadon, Land subsidence caused by the East Mesa Geothermal Field, California, observed using SAR interferometry, *Geophys. Res. Lett., 24,* 901-904, 1997.

Matthews, M. V., and P. Segall, Statistical inversion of crustal deformation data and estimation of the depth distribution of slip in the 1906 earthquake, *J. Geophys. Res., 98,* 12153-12163, 1993.

Meade, R. H., Petrology of sediments underlying areas of land subsidence in central California, *U.S. Geol. Surv. Prof. Pap., 497-C,* 83 pp., 1967.

Menke, W., *Geophysical Data Analysis: Discrete Inverse Theory,* Academic Press, San Diego, California, 289 pp., 1989.

Poland, J. F., and G. H. Davis, Land subsidence due to withdrawal of fluids, *Rev. Eng. Geol., 2,* 187-269, 1969.

Poland, J. F., and J. H. Green, Subsidence in the Santa Clara valley, California, a progress report, *U. S. Geol. Surv. Water-Supply Pap., 1619-C,* 16 pp., 1962.

Poland, J. F., and R. L. Ireland, Land Subsidence in the Santa Clara valley, California, as of 1982, *Mechanics of Aquifer Systems, U.S. Geol. Surv. Prof. Pap., 497-F,*61 pp., 1988.

Roberts, C. W., and R. C. Jachens, Isostatic residual gravity map of the San Francisco Bay area, *U.S. Geol. Surv. Geophys. Invest. Map GP-1006,* scale 1:286 500, 1993.

Rogers, T. H., and J. W. Williams, Potential seismic hazards in Santa Clara County, California, *California Division of Mines and Geology, Special Report, 107,* 39 pp., 6 plates, 1974.

Sandwell, D. T., and E. Price, Phase gradient approach to stacking interferograms, *J. Geophys. Res., 103,* 30183-30204, 1998.

Teufel, L. W., Permeability changes during shear deformation of fractured rock, *28th U. S. Sympos. Rock Mech.,* 473-480, 1987.

Tolman, C. F., Ground Water, New York, McGraw-Hill, first edition, 593 pp., 1937.

Watson, F. M., Bock, Y., and D. T. Sandwell, Satellite interferometric observations of displacements associated with seasonal ground water in the Los Angeles basin, *J. Geophys. Res.*, *107*, 1029/2001JB000470, 2002.

Williams, S., Bock, Y., and P. Fang, Integrated satellite interferometry: Tropospheric noise, GPS estimates and implications for interferometric synthetic aperture radar products, *J. Geophys. Res.*, *103*, 27051-27067, 1998.

Wilson, A. M., and S. Gorelick, The effects of pulsed pumping on land subsidence in the Santa Clara valley, California, *J. Hydrol.*, *174*, 375-396, 1996.

Wentworth, C. M., Blake, Jr., M. C., McLaughlin, R. J., and R. W. Graymer, Preliminary geologic description of the San Jose 30 x 60 minute quadrangle, California, *U.S. Geol. Surv. Open File Rep.*, *98-795*, 1999.

Zebker, H. A., Rosen, P. A., and S. Hensley, Atmospheric effects in interferometric synthetic aperture radar surface deformation and topographic maps, *J. Geophys. Res.*, *102*, 7547-7563, 1997.

Chapter 2

The interplay between creep and land subsidence along the southern Hayward fault

2.1 Introduction

The Niles District of Fremont, California, has long been known as a geologically active and complex region (Figure 2.1). Local residents first experienced the region's full seismic potential in 1868 when a **M6.8** earthquake ruptured along what was then known as the Niles-Irvington fault. As urban development spread throughout the twentieth century, residents observed that buildings and other structures that spanned the fault were continuously offset by surface creep. Today, the Niles-Irvington fault is referred to as the Hayward fault, an 80-km-long structure that continues north to San Pablo Bay. Whereas geomorphic and surface creep observations identify the fault on the surface, microseismicity has provided insight into the fault structure at depth [*Waldhauser and Ellsworth*, 2002]. Along the southern half of the Hayward fault, the seismicity diverges from the surface trace. The seismicity at depth continues to the east across the Mission step-over region where

slip from the Calaveras fault is transferred to the Hayward fault [*Andrews et al.*, 1993]. While no clear expression of a through-going fault is found at the surface, the seismicity suggests that the central Calaveras and the southern Hayward fault form one continuous, sub-vertical structure below a depth of 6 km. Four **M** ∼5 events occurred in the vicinity of the Calaveras-Hayward fault junction from 1858 to 1864 [*Toppozada et al.*, 1981; *Bakun*, 1999]. The kinematics of this sequence suggests a possible causative relationship with the **M** 6.8 earthquake on the southern Hayward fault in 1868.

While the majority of the Hayward fault exhibits surface deformation in the form of relatively steady right-lateral creep, the trace of the fault near Fremont exhibits transient and often complex deformation. A time-averaged creep rate of ∼9 mm/yr on the southernmost 5 km of the fault appears to be consistent for much of the twentieth century [*Lienkaemper and Galehouse*, 1997]. This high rate is striking because it is nearly twice the creep rate observed along the rest of the fault and has been difficult to explain with previous fault models [*Simpson et al.*, 2001; *Bürgmann et al.*, 1998]. A geologic rate rate of ∼9 mm/yr suggests that insignificant slip deficit has accumulated along the southernmost section of the fault [*Lienkaemper et al.*, 1991]. During the 1990's, this section of the fault experienced a dramatic reduction in creep rate in response to the **M**6.9, 1989 Loma Prieta earthquake [*Lienkaemper et al.*, 2001].

The seismic hazard associated with the Hayward fault has encouraged greater study of the fault system, including monitoring efforts using GPS, borehole seismometers, creepmeters, strainmeters, and alignment arrays [e.g., *Bilham and Whitehead*, 1997; *Lienkaemper et al.*, 1991]. These data provide information about slip that occurs on the
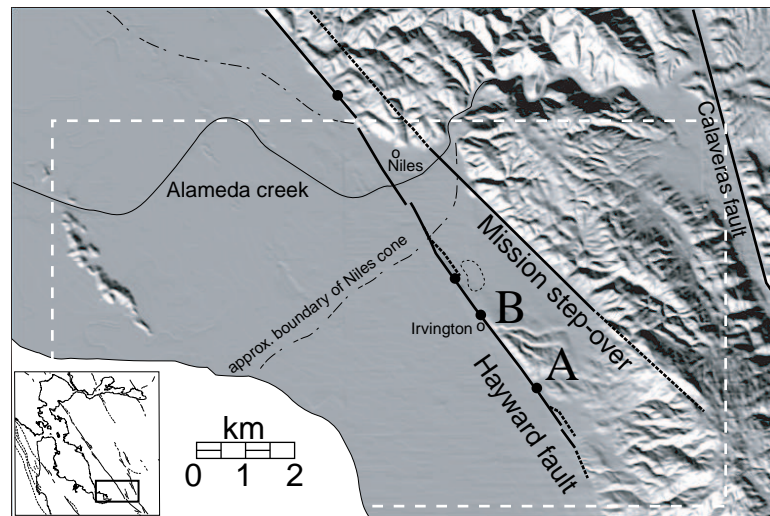
Figure 2.1: A shaded relief map of the Niles District in Fremont, California, shows the location of the southern Hayward fault relative to the Calaveras fault. Microseismicity follows along the Mission step-over. Alameda creek is responsible for creating the Niles alluvial fan. The approximate boundary of the alluvial fan as described by *Clark* [1915] is shown with a dash-dot line. The white-dotted box shows the extent of the InSAR data shown in later figures.

fault at depth producing deformation at the surface. Unfortunately, existing data sets provide a sparse sampling of the surface deformation. The spatial coverage of Interferometric Synthetic Aperture Radar (InSAR) data allows for the improved visualization of the surface deformation by increasing the spatial extent of coverage. *Bürgmann et al.*[1998] first interpreted InSAR data for the region. Using one interferogram, they hypothesized that vertical deformation may be significant as the fault terminates south of Fremont. In this paper, as many as 108 interferograms in addition to other existing data sets are used to evaluate the crustal deformation in the Niles district of Fremont.

2.2   Temporally and Spatially Complex Deformation

Over the past decade InSAR has become a powerful technique for measuring crustal deformation. Nine years of data collection by the ERS1/2 satellite of the European Space Agency have produced an opportunity to image secular, seasonal, and transient deformation at unprecedented spatial and temporal resolution. Developing the necessary tools to deal with this data set is imperative for minimizing artifacts and correctly interpreting the complex deformation. A time-series analysis is performed along the southern Hayward fault to resolve the time-dependent deformation. The time-series analysis inverts a collection of interferograms for the incremental range-change between SAR scene acquisitions. I invert 108 interferograms, all of which have perpendicular orbit baselines of less than 200 m, using the time series analysis described in Chapter 1. Figure 2.2 shows the temporal distribution of those interferograms that span the time period from June of 1992 to June of 2000. Interferograms are produced using the Repeat Orbit Interferometric Pack-

age (ROI PAC) developed at Caltech/JPL. Data are processed using 8 looks in range and 40 looks in azimuth resulting in a pixel dimension of 150 m.

The resulting time series of the region show the time-dependent range-change signal. Surface creep is best visualized by plotting the time-dependent range-change between two reference locations on opposite sides of the fault. The offset in range-change across the fault as a function of time is determined by averaging 9 pixels on either side of the fault and taking the difference. Assuming that the signal represents right-lateral creep, the range-change is projected onto a horizontal, fault-parallel vector. Approximately 3.3 mm of right-lateral offset produces 1 mm of range-change. The surface creep observed across a 1 km baseline at location A in Figure 2.1 is presented in Figure 2.3. The time series is evaluated by comparing it to existing data sets. Using an alignment array, *Lienkaemper et al.* [1997] observed left-lateral creep after the 1989 Loma Prieta earthquake followed by an 18 mm right-lateral creep event in the early months of 1996 (Figure 2.3a). While the magnitude of the left-lateral response ($\sim$3 mm of strike-slip motion) is too subtle for the InSAR data to resolve, the larger creep event is clearly indicated by the inversion. This result is noteworthy because the creep event is not well constrained by any individual interferogram. The creep event was observed at several alignment array locations along a $\sim$4 km stretch of the fault. The northern extent of the creep event was at a creepmeter located to the north (site B, Figure 2.1) were 4.5 mm was observed. The InSAR time series at this site is shown in Figure 2.3b, although no offset is resolved in the InSAR time series. A small seasonal signal is resolved in the final years of the time series where the temporal sampling improves. This seasonal signal is attributed to the differential swelling of sediments on either side of the
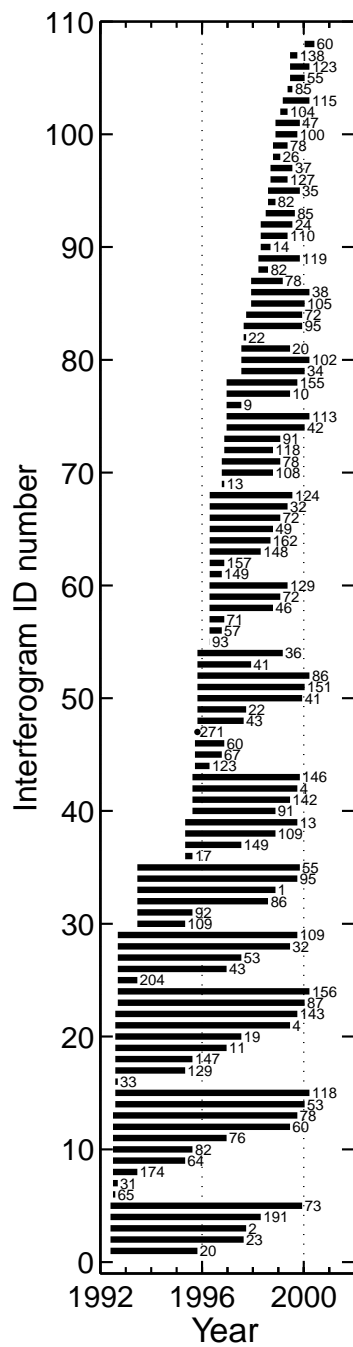
Figure 2.2: A total of 108 descending interferograms are used in the time-series analysis. Each horizontal bar represents the time period spanned by an interferogram with the perpendicular baseline (in meters) printed to the right. InSAR data were collected by ERS1 and ERS2 satellite along track 70, frame 2853.

fault producing a small vertical component with a peak-to-peak amplitude of ∼3 mm.

The frames of the time series can be examined to visualize the spatial extent of the deformation. Two examples from the time series are shown where significant deformation is localized in time (Figure 2.4a-b). These frames correspond to a time period that is not spanned by an actual interferogram. During a three year period from 1993 to 1996, localized deformation is found to the east of the fault near Irvington where a sharp offset in range-change is located along the fault trace. A broad region of increased range is observed to the west. This time period includes the creep event observed by the alignment array data.

A distinctly different pattern is observed from 1998 to 1999. An increase in range is observed on the east side of the fault at the outlet of Niles canyon. The increase in range (from blue to red) across the fault would correspond to either left-lateral creep or vertical motion with the east side down. Because the InSAR data resolves only one component of the deformation, the data used to produce the time series is not able to differentiate vertical and horizontal deformation without additional constraints.

The combination of ascending and descending SAR data, which are accquired using slightly different orbital geometries, can be used to determine the two-dimensional deformation field if the third dimension can be independently constrained. For strike-slip faults, the vertical and fault parallel deformation can be determined by assuming that the fault normal displacement is negligable. Given that the fault strikes at N35^{o}W, the ascending satellite orientation (with a look azimuth of 76°) will be less sensitive to fault parallel movement than the descending orientation (with a look azimuth of 284°). The range-change will also be positive or negative depending on whether right-lateral creep is
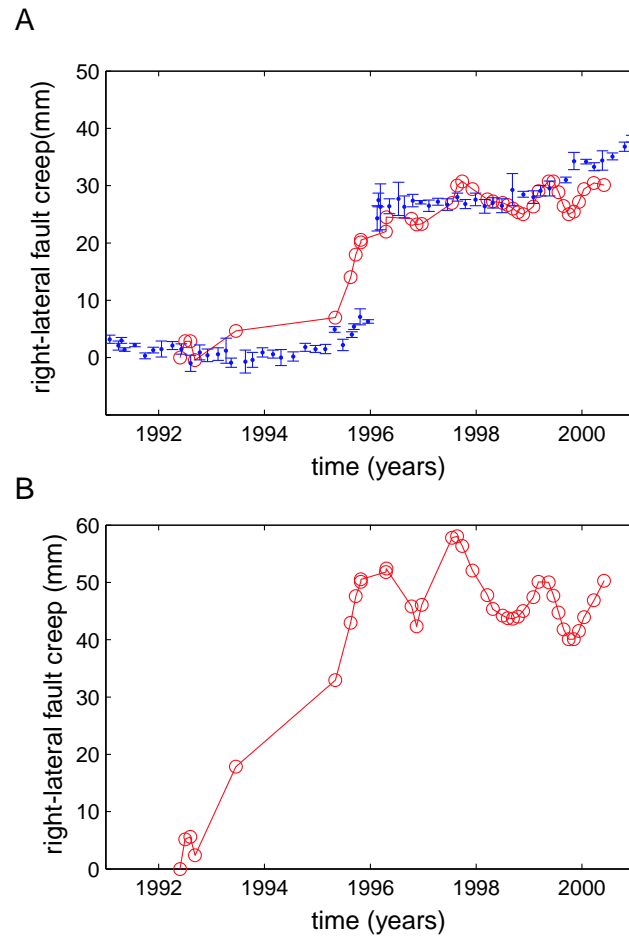
Figure 2.3: (A) The InSAR time series (circles) is compared to alignment array data (dots and error bars) on the southern Hayward fault at Camellia Drive (site A in Figure 2.1)[*Lienkaemper et al.*, 2001]. An 18 mm creep event was observed in February of 1996. The InSAR time series is multiplied by a factor to convert the range-change to fault parallel motion. (B) The time series is shown for a site further north along the fault (site B in Figure 2.1). A seasonal signal is resolved after 1996.
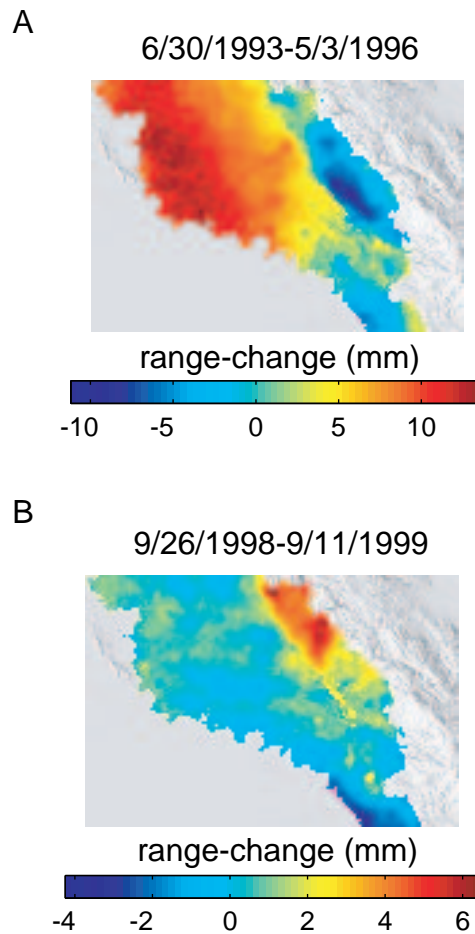
Figure 2.4: Two frames from the InSAR time series (color) are displayed over a shaded relief image of the topography (gray). The region shown corresponds to the white-dotted box in Figure 2.1. (A) The range-change from June 30, 1993 to May 3, 1996 captures the spatial extent of the deformation. Deformation to the east of the fault is related to the 1996 creep event. Deformation to the west outlines the net subsidence of the Niles alluvial fan. (B) The range-change over a one year period from September 26, 1998 to September 11, 1999 shows a localized signal near the outlet of Niles canyon. The analysis of several ascending interferograms suggests that this signal includes a vertical component.

projected onto the descending or ascending look vector, respectively. Additionally, the range-change is more sensitive to vertical than horizontal surface displacements because the satellite looks down at a steep angle of 23° off vertical.

Unfortunately, no ascending data were collected before 1995 and due to the paucity of ascending data in later years, only 12 interferograms are produced from the ascending SAR data. The time series result shown in Figure 2.4b and the available ascending data suggest that the range-change data are best explained by a component of vertical deformation near Niles in 1998. The strike-slip and dip-slip surface components along the fault trace are calculated by decomposing an ascending (3/23/1996-8/1/1999) and a descending (5/4/1996 - 8/7/1999) interferogram (Figure 2.5). The strike-slip component is well resolved and is consistent with the alignment array observations during this time period. A dip-slip component (east side down) of 10 mm is resolved near Niles while no dip-slip component is found to the south. Because of the steep gradient in phase near the fault trace, it is difficult to unwrap the data within several 100 meters of the fault trace for the ascending interferogram. However, the wrapped interferogram suggest that a discrete step in phase is found at the fault trace.

The InSAR time series and the decomposition of the range-change into strike-slip and dip-slip components all indicate complex, transient deformation along the southern Hayward fault.
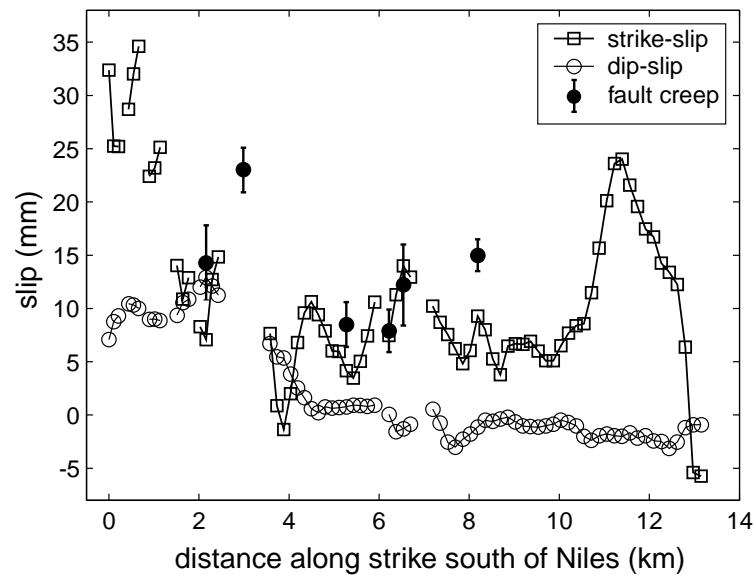
Figure 2.5: The vertical and fault-parallel components along the trace of the Hayward fault are determined by inverting a set of ascending and descending interferograms. The ascending interferogram spans from 3/23/1996 to 8/1/1999 and the descending interferogram spans from 5/4/1996 to 8/7/1999. The range-change signal decorrelates near the fault trace. Therefore, the vertical and fault parallel components are determined for a 1 km baseline across the fault. Error bars show the alignment array data of surface creep listed in Table 2.2 for the 1996-1999 time period.

2.3   Aseismic Slip Distribution

Assuming that the observed deformation is attributed to the Hayward fault, I invert for the slip distribution using a bounded variable least squares formulation [*Stark and Parker*, 1995]. Inversions are performed for two periods, the first from 1992 to 1997 and the second from 1996 to 1999. Two independent, descending interferograms were chosen from the 108 that were processed in the region (Figure 2.6). The two interferograms span a similar time period from 1992 to 1997 (Table 2.1). Cummulative surface creep during this time period is estimated from the data of *Lienkaemper et al.* [2001] and included as a constraint in the inversion (Table 2.2). The surface creep is determined by differencing the first and last measurement that best approximates the time span of the interferograms. Right-lateral slip is constrained between 0 and 0.1 m while the dip-slip component is constrained between $\pm$ 0.05 m. A Laplacian smoothing constraint is used to stabilize the inversion [*Harris and Segall*, 1987]. A smoothing weight of 400 is used in the inversion (Figure 2.7).

Displacement Green's function are calculated using the boundary element code POLY3D [*Thomas*, 1993] which allows for angular dislocations. The fault surface is discretized into triangular elements. In the top 4 km, the non-planar fault surface dips $\sim 65^o$ to the east so as to join with the microseismicity diverging from the surface trace. Vertical subfaults continue to a depth of 12 km. An additional discretized fault surface is placed to the north of Niles along the Hayward fault and extends from the surface to a depth of 4 km. Slip on these subfaults is constrained to a value consistent with 5 mm/yr to account for surface creep on the adjacent section of the fault. Below this creeping section, the fault is presumed to be locked at depth [*Lienkaemper et al.*, 1991; *Waldhauser and Ellsworth*,
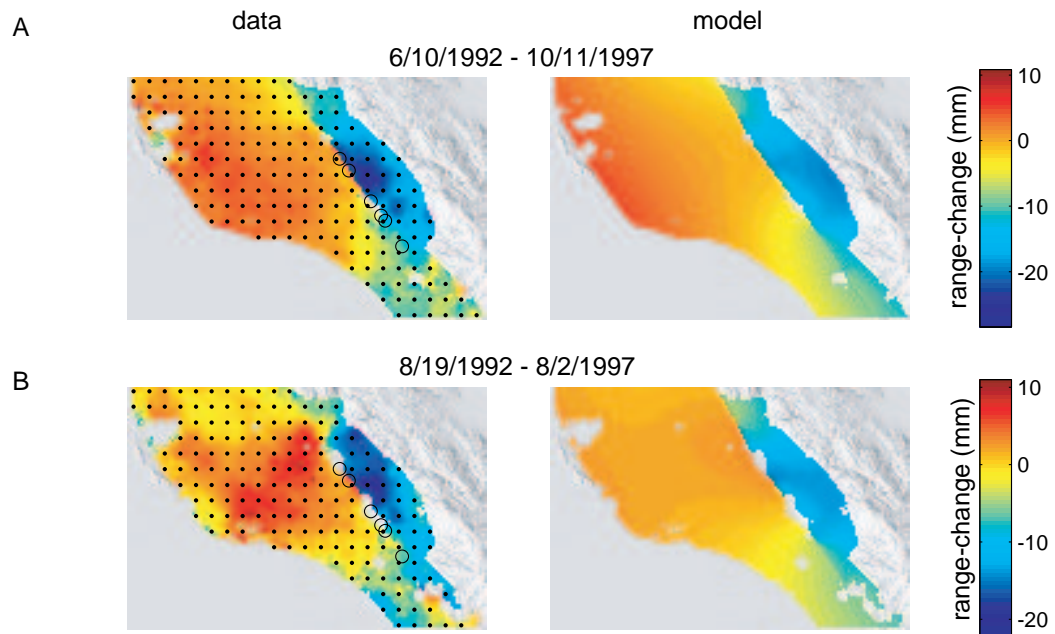
Figure 2.6: Two descending interferograms (left column) are inverted to determine the aseismic slip during the period from 1992 to 1997. The InSAR data are subsampled (black dots) at a resolution of 1 km. Surface creep observations measured by *Lienkaemper et al* [2002] at several alignment array sites (open black circles) are used as an additional constraint. The predicted range-change for the inversion is shown to the right of each interferogram. The difference in appearance between the predicted range-change plots is caused by the difference in tilt and offset of the two interferograms.

Table 2.1: Interferograms used in the inversion for distributed aseismic slip.

Date1 YYYYMMDD	Date2 YYYYMMDD	Track	Frame	Sat1	Orbit1	Sat2	Orbit2	Perpend. Base. (m)	Δt (yr)
				Inversion 1992-1997					
19920610	19971011	70	2853	ERS1	4724	ERS2	12950	3	5.4
19920819	19970802	70	2853	ERS1	5726	ERS2	11948	13	5.0
				Inversion 1996-1999					
19960323	19991010	478	747	ERS1	24514	ERS2	23378	14	3.5
19960324	20000507	478	747	ERS2	4841	ERS	226384	192	4.1
19960503	19990529	70	2853	ERS1	25108	ERS2	21467	126	3.1
19960504	19990807	70	2853	ERS2	5435	ERS2	22469	127	3.3
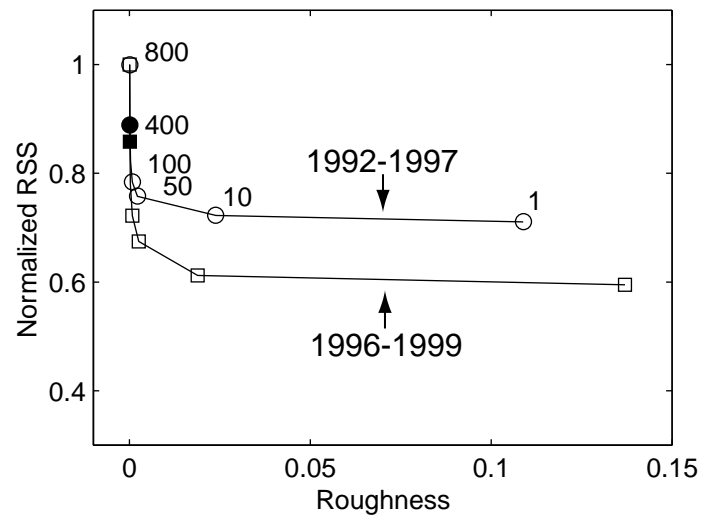
Figure 2.7: The smoothing weight is evaluated by examining the tradeoff between the normalized residual sum of squares (RSS) and the model roughness for each inversion. Models that are rough do a better job of fitting the data resulting in a smaller RSS. However, smoother models are preferred at the expense of increasing the RSS. The choice of smoothing parameter is designated with a filled symbol.

2002; *Simspon et al.*, 2001]. Three additional model parameters solve for an offset and linear tilt across each interferogram. This is done to account for a regional gradient that might be associated with an error in the orbital baseline of the satellite or a low frequency atmospheric artifact.

The resulting slip distribution resembles clockwise rotation of the east side of the fault relative to the west side with an up-dip displacement of 45 mm north of Niles and down-dip displacement of 25 mm near the southern edge of the parameterized fault plane (Figure 2.8a). The transition from up-dip to down-dip displacement is centered directly below Irvington at a depth of ~7 km. Strike-slip displacement with a magnitude of 35 mm is found at a depth of 10 km to the north of Niles. A second patch of strike-slip displacement with a magnitude of 38 mm is resolved in the top 4 km and extends along strike between Niles and Irvington. Insignificant strike-slip displacement is resolved south of Irvington during this period.

A similar inversion is performed for the time period from 1996 to 1999 using 4 independent interferograms (2 ascending and 2 descending, Table 2.1). The 4 original interferograms are shown in Figure 2.9. Cumulative surface creep over this time period is estimated from *Lienkaemper et al.*[2001] as discussed above and used as an additional constraint. The inversion resolves a maximum strike-slip displacement of 45 mm at depth on the southern portion of the fault (Figure 2.8b). The strike-slip displacement south of Irvington is in contrast to the 1992-1997 period where no strike-slip displacement was observed on this portion of the fault. The dip-slip pattern of up-dip displacement north of Niles and down-dip displacement south of Irvington is similar to that found from 1992-
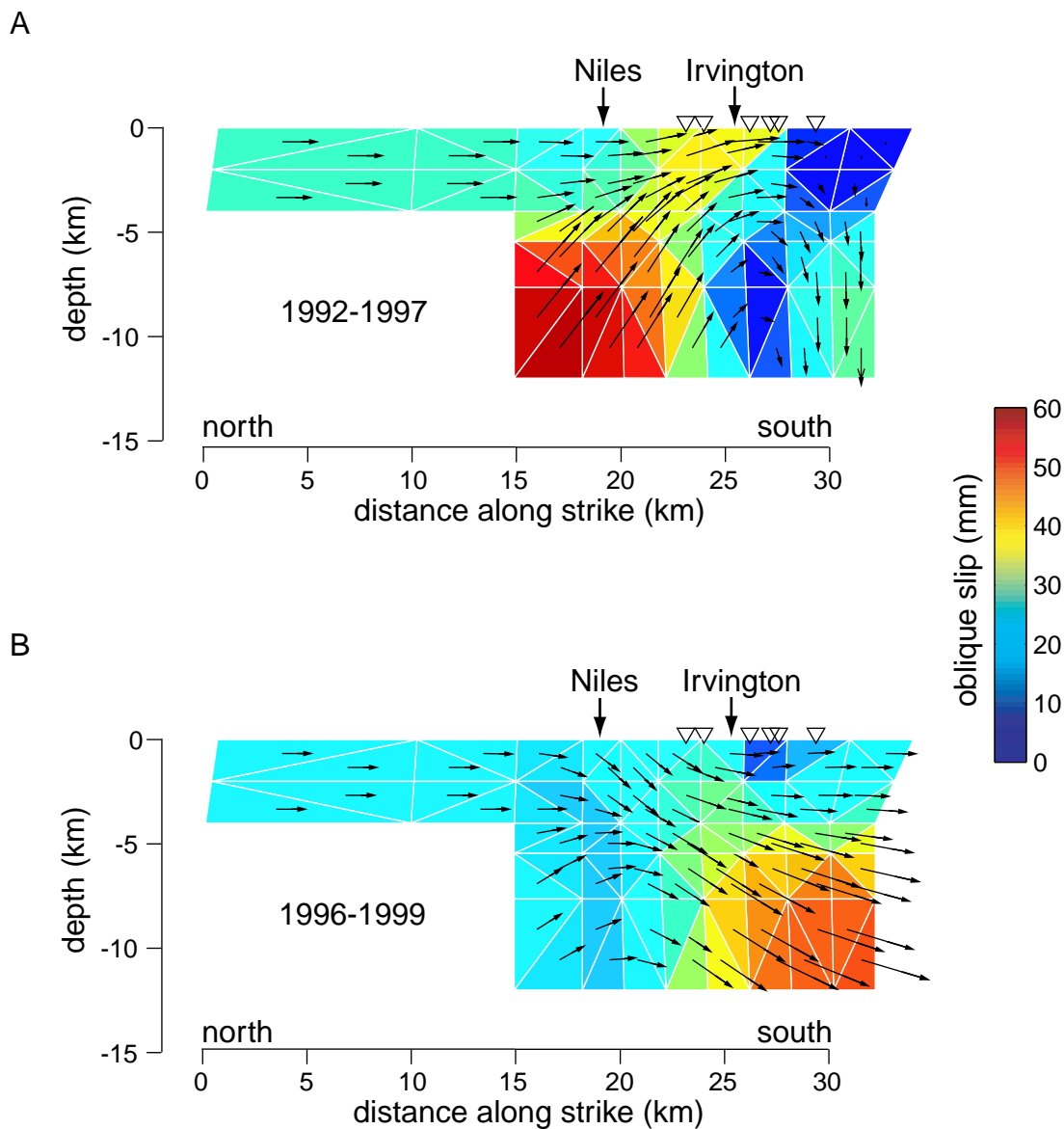
Figure 2.8: The oblique slip distribution along the southern Hayward fault is shown for two time periods: (A) 1992 to 1997 and (B) 1996 to 1999. The arrows show the displacement of the east side of the fault relative to the west side. The individual interferograms used in the inversion and the model predictions are shown in Figures 2.6 and 2.9. Table 2.2 lists the surface creep observations included in the inversion and the location of these measurements along strike are shown above (open triangles). North of Niles, the Hayward fault is assumed to be locked at depth.

1997, however the magnitudes are significantly reduced. A component of east side down displacement on the order of 16 mm is found in the top few kilometers near Niles.

2.4 Discussion

There exist several caveats when interpreting the slip distribution for the two time periods. Beginning with the Loma Prieta earthquake in 1989, the southern Hayward fault entered a transient state where surface creep rates greatly diminished from that observed prior to 1989. Therefore the inversion results do not characterize the long-term aseismic slip distribution on the fault. Additional concerns arise from the unknown fault geometry of the Mission step-over region. It is unclear how the surface trace of the Hayward fault connects to the active seismicity at depth. The fault plane is parameterized to end south of Fremont, consistent with the mapping of the active surface trace of the Hayward fault. The relocated seismicity of *Waldhauser and Ellsworth* [2002] delineates a continuos fault at depth that connects to the Calaveras fault. Our parameterization does not allow for slip to occur to the south, which may effect the distribution.

Strike-slip displacement at <4 km depth below Irvington during the 1992-1997 time period and shallow dip-slip displacement near Niles between 1996 and 1999 explain the primary crustal deformation signal observed in the InSAR data. However, the inversion results suggest additional complexity at depth. Because the InSAR data extends along the surface to a distance of less than 4 km from the trace of the fault, the inversions can only be expected to resolve slip in the top few kilometers of the fault. However, slip on the deep portions of the fault (below 5 km) do help to model some of the long wavelength features
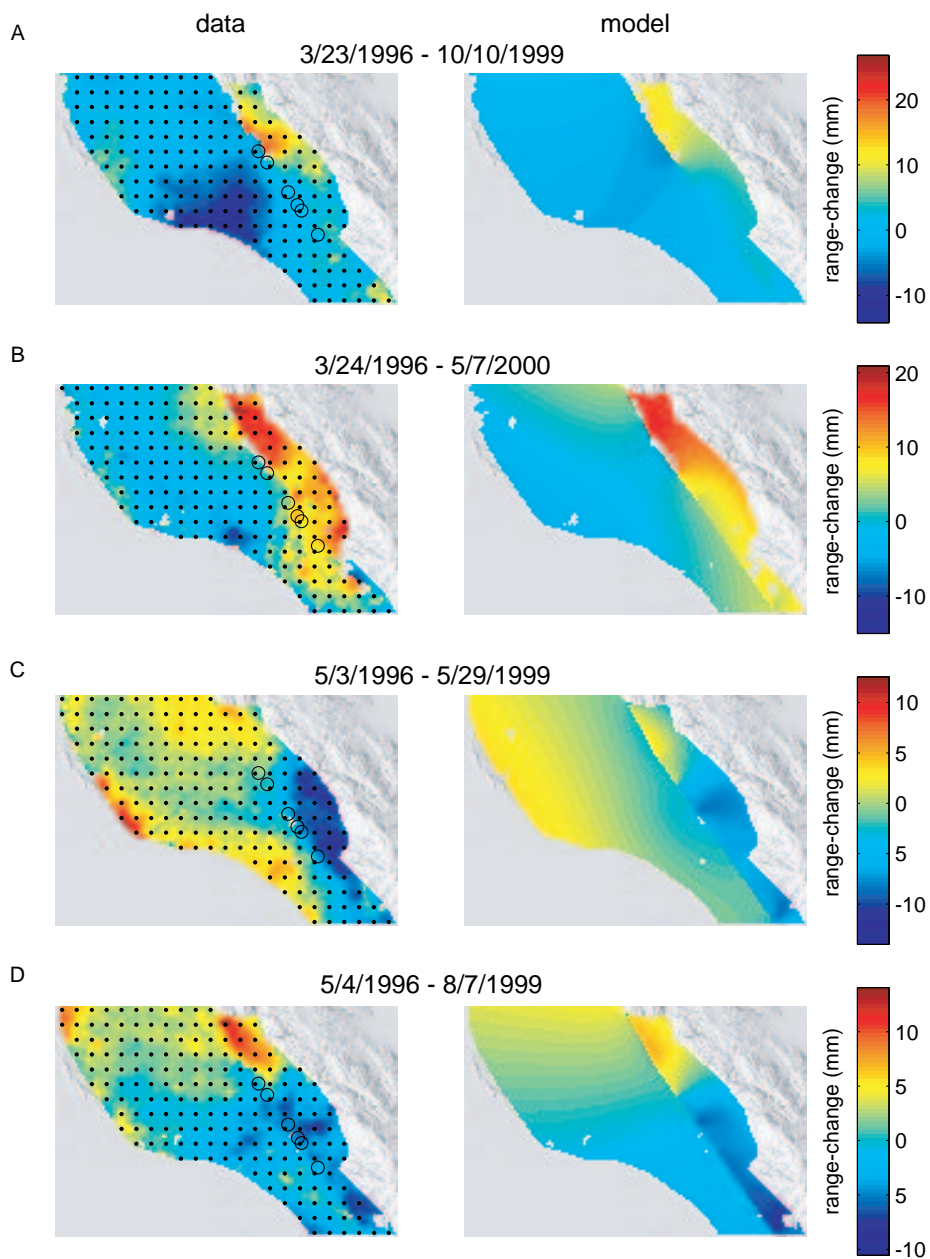
Figure 2.9: InSAR data (left column) and predicted range-change (right column) are shown for the inversion of InSAR data from 1996 to 1999. Two ascending (A-B) and two descending (C-D) interferograms are used in the inversion. See the caption of Figure 2.6 for additional information.

in the InSAR data.

For the time period from 1992 to 1997, the inversion has difficulty modeling the elevated range-change to the west of the Hayward fault extending towards the San Francisco Bay. It is this signal that gives rise to the complex dip-slip displacement pattern at depth in the inversion. The increase in range-change on the westernmost edge of the InSAR data is also accommodated by the transition from 0 to 35 mm of slip from south to north at depth.

During the 1996 to 1999 time period, vertical deformation at the surface is easier to establish with the availability of both ascending and descending InSAR data. Although the Hayward fault is primarily a strike-slip system, historical evidence does exist for localized vertical deformation of tectonic origin across the fault in this region. Eyewitness accounts of the 1868 earthquake report that the east side of the fault subsided near Niles [*Clark*, 1915]. *Lawson* [1908] also noted the vertical throw of the fault when documenting the surface rupture. The modeling of deformation near the ends of a fault also require significant dip-slip and vertical deformation [*Bürgmann et al.*, 1998].

However, the vertical surface deformation along the fault could also be attributed to land subsidence where the decrease in pore pressure in the alluvium leads to the compaction of the sediments. The proximity of the inferred vertical ground movement to an outlet of a major watershed and a large aquifer provide a potential source for the vertical range-change signal.

2.4.1   Land Subsidence of the Niles Fan

Ground water is supplied to the region via Alameda Creek, the primary drainage for a 1.6×10^3 km^2 watershed which includes the Livermore and Sunol valleys [*California Department of Water Resources*, 1967]. Discharge from the creek over the past 600 kyr has produced the Niles alluvial fan located at the mouth of Niles Canyon [*Koltermann and Gorelick*, 1992]. Several large aquifers extend out under the San Francisco Bay from this locality. Movement on the fault bisects the alluvial fan and has diverted the path of Alameda Creek as evidenced by several abandoned stream channels [*Clark*, 1915].

The differential level of the water table in wells on opposite sides of the Hayward fault first identified it as a barrier to subsurface fluid flow. The analysis of well levels over a four month period by *Clark* [1915] revealed that subsurface water travels in an asymmetric fashion along the Hayward fault following the seasonal recharge of water. High permeabilities on the east side of the fault result in the quick recharge of wells. Because the fault appears impermeable, the only source of water for wells on the west side of the fault comes from Alameda creek. For the wells west of the fault, those that are closest to Alameda creek are first to recover following the seasonal influx of surface water. Therefore, the expected pattern of seasonal, differential land subsidence near Irvington is for the east side of the fault to uplift in the winter and subside in the summer. Differential subsidence near Niles is expected to be minimal given that both sides of the fault are supplied by the same water source, and thus, uplift or subside in unison. The secular pattern of land subsidence is difficult to predict without long term records of well levels. However, net subsidence or uplift is expected to outline the shape of the primary confined aquifer defined

by the Niles alluvial fan.

The deformation along the southern San Francisco Bay is likely related to land subsidence of the aquifer system. Several interferograms exhibit a range-change pattern that mimics the shape of the Niles alluvial fan (Figure 2.4a). Near the apex of the fan, a small seasonal signal is observed in the InSAR time series on both sides of the fault. In the latter months of 1998, the 10 mm vertical signal observed in the InSAR data suggest land subsidence on the east side of the Hayward fault (Figure 4b). This signal would reduce the right-lateral creep as observed along the satellite's line-of-sight in several descending interferograms. The spatial pattern suggests that the deformation is localized to the east side of the fault. The location of the subsidence at the outlet of the canyon argues for a hydrologically related process; Although, the subsidence appears to be a transient event unrelated to the seasonal cycle of deformation.

2.4.2 The 1996 Creep Event

The 18 mm creep event was clearly observed in the alignment array data of *Lienkaemper et al.* [2002]. The event was observed at 4 locations which suggests that the creep event extended 1.7-3.7 km along strike. The alignment array observations constrain the event to occur between 12/16/1995 and 2/17/1996. However, *Lienkaemper et al.* [1997] suggest that the event occurred around the 7th of February. However, no corresponding strain event was measured by several dilatational strainmeters located within 6 km of the event (M. Johnston, personal communication). This would suggest that the size of the creep event was below the detection threshold of the dilatational strainmeters and likely occurred on a patch extending from the surface to a depth no greater than several

100 m [*Johnston and Linde*, 2002].

Such a small event would also be difficult to resolve in the InSAR data given the spatial resolution of interferograms. Despite the small inferred size of the creep event, a localized deformation pattern is found in those interferograms spanning the time period. The slip distribution for the 1992-1997 period resolves a 38 mm patch of slip at a depth of 4 km below the surface creep event. The InSAR time series shown in Figure 2.3 places the creep event in the later part of 1995 whereas the alignment array data observed the event in early 1996. The inspection of individual interferograms show that no discrete offset is observed in the early months of 1996, which is consistent with a shallow creep event. The InSAR time series shown in Figure 2.3 is determined across a 1 km baseline which would be more sensitive to slip at greater depths than the alignment array data. This suggests that a deeper transient event may have occurred in 1995 which eventually propagated to the surface in the early months of 1996.

2.5   Conclusions

In this paper, InSAR data are used to visualize the localized deformation from 1992 to 2000 along the southern Hayward fault. A surface creep event observed in the early months of 1996 may have initiated with a transient aseismic event in late 1995. Inversions for the aseismic slip distribution suggest that the transient event occurred in the top few kilometers of the fault. Land subsidence of the Fremont aquifer and the Niles alluvial fan best explains the increase in range-change to the west of the Hayward fault. The detailed analysis of well water levels may provide additional answers. However, insufficient data

exists to evaluate the hydrology of the region during the time period of interest. A more perplexing vertical signal is observed in 1998 near Niles. While it is difficult to attribute the vertical deformation to solely a tectonic or hydrologic origin, it is possible that both played a role. An abnormally high influx of water to the ground water system during the winter of 1998 may have altered the mechanical properties of the fault surface. Alternatively, an increase in crustal or fault zone pore pressures may have been sufficient to alter the stress condition on the fault and instigate aseismic creep.

Table 2.2: Surface creep constraints used in the inversions for distributed slip.

location	time period	observed (mm)	predicted (mm)
	Inversion 1992-1997		
Subfaults[a]	1992-1997	26.0	-
Rockett	1992.568-1997.989	32.7±3.0	33.2
Union	1993.019-1997.647	36.6±2.4	38.3
Pine[b]	1993.022-1997.647	44.9±0.9	35.9
Camellia[b]	1992.432-1997.647	28.7±1.4	35.9
Parkmeadow[b]	1992.432-1997.797	24.7±1.3	35.9
Mission	1993.189-1997.644	6.6±1.7	8.2
	Inversion 1996-1999		
Subfaults[a]	1996-1999	17.5	-
Rockett	1996.361-2000.060	14.3±3.5	17.4
Union	1996.210-1999.679	±2.1	19.6
Pine[b]	1996.191-1999.696	8.5±2.1	10.4
Canellia[b]	1996.361-1999.849	7.9±2.0	10.4
Parkmeadow[b]	1996.361-2000.079	12.2±3.8	10.4
Mission	1996.210-1999.699	15.0±1.5	14.9

[a]Slip constraint for subfaults north of Niles consistent with 5 mm/yr of creep.
[b]Located on an identical subfault.

Bibliography

Andrews, D. J., Oppenheimer, D. H., and J. J. Lienkaemper, The Mission link between the Hayward and Calaveras faults, *J. Geophys. Res., 98,* 12083-12095, 1993.

Bakun, W. H., Seismic Activity of the San Francisco Bay Region, *Bull. Seism. Soc. Am., 89,* 764-784, 1999.

Bilham, R., and S. Whitehead, Subsurface creep on the Hayward fault, Fremont, California, *Geophys. Res. Lett., 24,* 1307-1310, 1997.

Bürgmann, R., Fielding, E., and J. Sukhatme, Slip along the Hayward fault, California, estimated from space-based synthetic aperture radar interferometry, *Geology, 26,* 559-562, 1998.

California Department of Water Resources, Evaluation of groundwater resources, South San Francisco Bay, appendix A: Geology, Bulletin 118-1, 153 p., 1967.

Clark, W. O., Ground-water resources in the Niles cone and adjacent areas, California, *U. S. Geological Survey Water-Supply Paper 345-H*, 127-168, 1915.

Harris, R. A., and P. Segall, Detection of a locked zone at depth on the Parkfield, California, segment of the San Andreas fault, *J. Geophys. Res., 92,* 7945-7962, 1987.

Johnston, M. J. S., and A. T. Linde, Implications of crustal strain during conventional, slow, and silent earthquakes, *in* International Handbook of Earthquake and Engineering Seismology, 81A, 1-17, 2002.

Koltermann, C. E., and S. M. Gorelick, Paleoclimatic signature in terrestrial flood deposits, *Science, 256,* 1775-1782, 1992.

Lawson, A. C. (Ed.), *The California Earthquake of April 18, 1906, Report of the State Earthquake Investigation Commission,* vol. 1, Carnegie Inst. of Washington, Washington, D. C., 1908.

Lienkaemper, J. J., Map of recently active traces of the Hayward fault, Alameda and Contra Costa counties, California, *U. S. Geolol. Surv.,* Map MF-2196, 1992.

Lienkaemper, J. J., and G. Borchardt, Holocene slip rate on the Hayward fault at Union City, California, *J. Geophys. Res., 101,* 6099-6108, 1996.

Lienkaemper, J. J., Borchardt, G., and M. Lisowski, Historic creep rate and potential for seismic slip along the Hayward fault, California, *J. Geophys. Res., 96,* 18261-18283, 1991.

Lienkaemper, J. J., and J. Galehouse, Revised long-term creep rates on the Hayward fault, Alameda and Contra Costa Counties, California, *U.S. Geol. Surv. Open File Rep., 97-690,* 1997.

Lienkaemper, J. J, and J. Galehouse, New evidence doubles the seismic potential of the Hayward fault, *Seism. Res. Lett., 69,* 519-523, 1998.

Lienkaemper, J. J., Galehouse, J. S., and R. W. Simpson, Creep response of the Hayward Fault to stress changes caused by the Loma Prieta earthquake, *Science, 276,* 2014-2016, 1997.

Lienkaemper, J. J., Galehouse, J. S., and R. W. Simpson, Long-term monitoring of creep rate along the Hayward fault and evidence for a lasting creep response to 1989 Loma Prieta earthquake, *Geophys. Res. Lett., 28,* 2265-2268, 2001.

Simpson, R. W., Lienkaemper, J. J., and J. S. Galehouse, Variations in creep rate along the Hayward Fault, California, interpreted as changes in depth of creep, *Geophys. Res. Lett., 28,* 2269-2272, 2001.

Stark, P. B., and R. L. Parker, Bounded variable least squares: an algorithm and applications, *J. Comp. Stat., 10,* 129-141, 1995.

Thomas, A. L., POLY3D: A three-dimensional, polygonal element, displacement discontinuity boundary element computer program with applications to fractures, faults, and cavities in the earth's crust, Masters Thesis, Stanford University, 62 pp., 1993.

Tolman, C. F., Ground Water, McGraw-Hill Book Company, Inc., 593 p., 1937.

Waldhauser, F., and W. L. Ellsworth, Fault structure and mechanics of the Hayward fault, California, from double-difference earthquake locations, *J. Geophys. Res., 107,* 10.1029/2000JB000084, 2002.

Chapter 3

Distribution of aseismic slip-rate on the Hayward fault inferred from seismic and geodetic data

3.1 Introduction

Several faults within the San Andreas fault system have long been known to exhibit interseismic creep at the surface, including the central San Andreas fault, the Maacama fault, the Concord fault, the Calaveras fault, and the Hayward fault [*Galehouse*, 2002]. However, the underlying factors that explain why these faults exhibit surface creep and others do not are not understood. The range of faulting behavior is not limited to steady, interseismic creep or coseismic rupture. The detection of slow earthquakes along subduction zones [*Dragert et al.*, 2001; *Miller et al.*, 2002], transient aseismic slip events on the central San Andreas fault [*Linde et al.*, 1996, 1992], and postseismic afterslip [e.g., *Smith and Wyss*, 1968; *Bilham et al.*, 1989; *Bürgmann et al.*, 2002] have demonstrated that a greater percentage of accumulated strain is released through aseismic processes than was previously appreciated.

The spectrum of fault behavior ranging from seismic to aseismic end members may be controlled by the material properties of the fault zone that translate into variations in frictional properties. Slip behavior can be interpreted under a rate-and-state friction framework. Originating from experimental work on rock friction, rate-and-state friction is an empirical, mathematical representation of the frictional interaction between two surfaces [*Marone*, 1998]. For real fault systems, the factors that determine whether two rock surfaces slip under an applied stress are difficult to isolate due to the complexity of the system. However, rate-and-state friction suggests that the stiffness of the surrounding rock and the constitutive properties of the fault surface and gouge zone dictate the slip behavior [*Marone and Scholz*, 1988]. The presence of clay lithologies or the thickness of the gouge zone are examples of factors that may control the frictional response. Faults that exhibit velocity-strengthening are associated with stable creep while velocity-weakening behavior leads to stick-slip behavior.

Other investigators have shown that material heterogeneity is not required to establish a heterogeneous slip-rate distribution that persists over multiple earthquake cycles (*Horowitz and Ruina*, 1989). A complex and long-lasting stress state could be responsible for variations in slip behavior. Evidence for a heterogeneous stress state on faults is well documented [*Rivera and Kanamori*, 2002]. Geometric complexities, such as bends in the fault, produce stress concentrations that persist until the fault can straighten itself by shearing asperities.

One approach for identifying which factors control fault behavior on real fault systems is to correlate the spatial variations in fault behavior with the heterogeneity of

fault properties or characteristics. This requires that the distribution of fault behavior, such as the interseismic slip-rate distribution, can be resolved using geophysical data. By inverting trilateration data on the Parkfield segment of the San Andreas fault, *Harris and Segall* [1987] resolved the transition from the locked to the creeping section and spatially correlated the distribution with earlier earthquakes. Their result was later confirmed by more recent GPS data [*Murray et al.*, 2001]. However the resolving power of geodetic data to infer slip on faults at depth remains limited. Recently developed space geodetic techniques, such as InSAR, and cross-correlation relocation techniques of seismicity have helped to provide a new level of detail.

The Hayward fault in the San Francisco Bay Area presents itself as a candidate system for the study of aseismic fault behavior because a wide range of complimentary data sets are readily available. The Hayward fault is a major strand of the San Andreas fault system accommodating nearly 25% of the deformation across the plate boundary (Figure 3.1). The fault exhibits a diversity of slip behaviors including large coseismic rupture, frequent micro-seismicity, and aseismic creep. Surface creep is observed along the entire length of the fault in the range of 3-9 mm/yr and the rates appear to be consistent over the past several decades [*Lienkaemper et al.*, 1998]. The geologic slip-rate on the fault is estimated at $\sim$9 mm/yr [*Lienkaemper and Borchardt*, 1996; *Lienkaemper et al.*, 1991; *Williams*, 1995]. The difference between the geologic and contemporary creep rates suggests that a slip deficit exists and that the accumulating elastic strain will presumably be released in a future earthquake.

Assessing the seismic potential and developing our understanding of the fault has
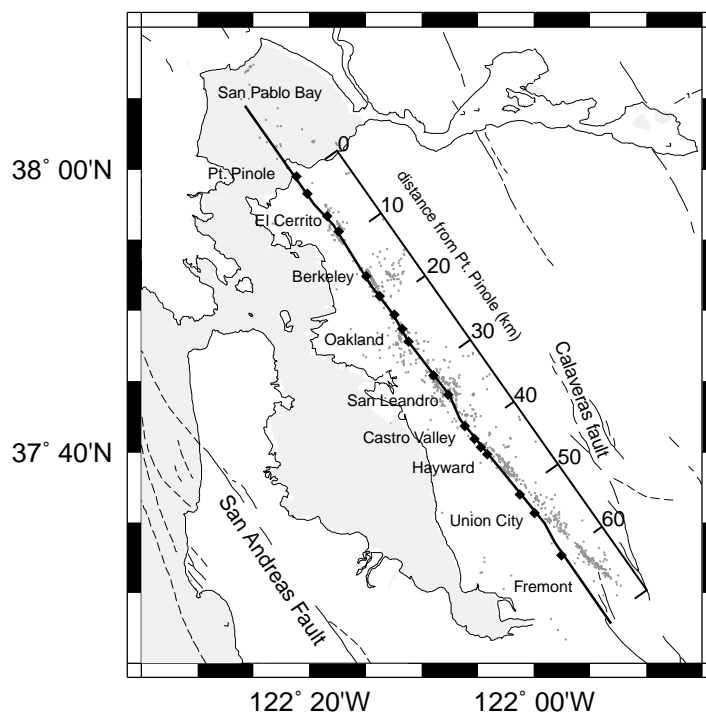
Figure 3.1: A map of the San Francisco Bay Area shows the major faults in the region including the San Andreas, Hayward, Calaveras, and Greenville faults. The surface trace of the modeled Hayward fault is shown with a bold line. The background seismicity (gray dots) and the location of surface creep observations (solid squares) are also shown. The scale bar marks the distance along the fault from Pt. Pinole.

been the topic of several previous studies. The established model for the Hayward fault consists of a fault that is locked at depth. Stress imposed by slip on neighboring faults and across the plate boundary drives aseismic slip in the shallow subsurface of the fault producing the creep observed at the surface. *Savage and Lisowski* [1993] developed a friction model to relate the depth of creep and the rate of stress accumulation to the surface creep rate. They estimate that enough strain is accumulating per century for at least a **M6.8** event for the entire length. *Lienkaemper and Galehouse* [1998] used revised surface creep measurements to upgrade the seismic potential of the fault to **M7**. Using space-geodetic data, *Bürgmann et al.* [2000] inverted directly for the depth of creep on the northern segment of the Hayward fault. They argue that based on seismic data and forward boundary element models (BEM), this segment of the fault may be mechanically distinct from the southern Hayward fault and may not release accumulated strain in coseismic events. *Simpson et al.* [2001] used BEM to relate the along-strike variation in the surface creep rate to the depth of creep. They identify several regions where the fault is likely locked at depth. *Malservisi et al.* [2001] used a visco-elastic finite element model driven by far-field plate velocities to provide a more realistic representation of the loading conditions on the Hayward fault. Through a series of forward models, they find creep to extend to greater depths than that predicted using elastic models driven by slip on deep dislocations. By analyzing the microseismicity on the fault, *Wyss* [2001] mapped the location of locked asperities using the local recurrence time. *Waldhauser and Ellsworth* [2002] also attempt to identify regions where aseismic slip is restrained, or the fault is locked, based on the distribution of the background seismicity which they relocate using cross-correlation techniques.

The most significant earthquake to occur on the Hayward fault in historic times was a $\mathbf{M}6.8$ event in 1868 [*Lienkaemper et al.*, 1991; *Toppozada and Borchardt*, 1998]. The event likely nucleated on the southern portion of the fault and ruptured as far north as Berkeley (at km 20, distance referenced from Pt. Pinole) [*Yu and Segall*, 1996; *Lawson*, 1908]. No earthquake greater than $\mathbf{M}_L 4.5$ has been observed on the Hayward fault since seismic instrumentation was installed in the early twentieth century [*Oppenheimer et al.*, 1992]. However, paleoseismic data suggest that several large earthquakes have produced surface rupture on both the northern and southern portions of the Hayward fault [*Hayward fault Paleoearthquake Group*, 1999; *Lienkaemper et al.*, 1999]. The lack of significant seismic moment release on the northern segment of the fault within recorded history has raised concern that this segment may be overdue for a large earthquake. The *Working Group on California Earthquake Probabilities* [1999] identified the Hayward fault as a significant potential threat to the loss of life and property in California. The hazard associated with such an event is significant because the Hayward fault passes beneath several urban communities in the San Francisco Bay Area.

In Chapter 2, the time-dependent, localized deformation on the southern Hayward fault was addressed. In this chapter, the analysis of *Bürgmann et al.*[2000] is expanded to incorporate updated geodetic and seismic data sets and extend the modeling over the northern 50 km of the fault. An inversion for the aseismic slip-rate distribution is performed using data from Interferometric Synthetic Aperture Radar (InSAR), the Global Positioning System (GPS), slip-rate estimates from characteristic repeating earthquake (CRE) sequences, and surface slip-rate observations. The inversion results provide evidence for a heteroge-

neous slip-rate distribution consisting of locked and creeping patches.

3.2 Fault Zone Structure and Geometry

The active surface trace of the Hayward fault is well documented from both geomorphic evidence and from the offset of man-made structures [*Lienkaemper*, 1992]. The fault generally strikes N35^{o}W; however, several salients indicate a more complex fault structure. Starting from the north end of the fault, San Pablo Bay (km -10) resides in an extensional basin formed in a right step-over from the Hayward fault to the Rodgers Creek fault. Despite attempts to determine the fault structure below San Pablo Bay using reflection seismology, gravity [*Chapman and Bishop*, 1988], and stratigraphic cross sections [*Wright and Smith*, 1992], a complete description of the fault structure north of Pt. Pinole (km 0) remains inconclusive. However, it is believed that the Hayward and Rodgers Creek faults join at depth. Moving south, high-resolution seismic relocations performed by *Waldhauser and Ellsworth* [2002] delineate a sub-vertical fault plane. Near Berkeley (km 18), seismic clusters illuminate several off-fault, sub-parallel structures. A diffuse zone of seismicity is observed near Oakland (km 20-30) with no clear organization. A cluster of seismicity beneath San Leandro (km 33) shows a complex fault surface that resembles an inverted flower structure. South of Castro Valley (> km 40), the seismicity at depth and the surface expression of the fault diverge suggesting that the upper few kilometers of the fault dips steeply to the east. The angular offset of the seismicity from the surface trace and the complex nature of the fault surface revealed through the relocations of *Waldhauser and Ellsworth* [2002] suggest that surface displacements are best modeled using a non-planar surface.

3.3 Method

GPS and InSAR data are inverted for the slip-rate on sub-vertical dislocations in an elastic half-space using the boundary element code POLY3D [*Thomas*, 1993]. The formulation of *Comninou and Dundurs* [1975] for an angular dislocation allows for a more complex geometry than the commonly used rectangular dislocation [*Okada*, 1985]. Surface creep rates and creep rates determined from characteristic repeating microearthquake sequences are used as additional constraints in the inversion. The deformation rate is assumed to be constant over the time spanned by the various data sets. While evidence for episodic aseismic transients have become more common with an increase in observational data and the greater scrutiny of the data sets, surface creep rates appear constant along the northern portion of the fault. No significant fault transients are known to have occurred on the northern and central Hayward fault during the time period of interest. Only the southern most few kilometers of the Hayward fault (km 63-68) exhibit transient behavior which appears to be related to the stress perturbation and recovery imposed by the 1989 Loma Prieta earthquake [*Lienkaemper et al.*, 1997; *Lienkaemper et al.*, 2001]. In this chapter, the analysis focuses on the Hayward fault north of Union City (km 0-50) where the creep rates appear constant.

A weighted inversion is performed using a bounded variable least squares (BVLS) approach [*Stark and Parker*, 1995] which minimizes the L2 norm, $\|W(d-Gm)\|_2 + \|\gamma\nabla^2 m\|_2$ where m is the strike-slip component on each subfault, G is the design matrix which contains the displacement Green's functions, and d is the data. The design matrix, G is constructed for surface displacement and creep data as described in *Harris and Segall* [1987]. The various

data sets are weighted so that W contains the available covariance information. Given the diversity in data used in this analysis, it is also useful to apply a factor that weights the data sets relative to one another. A smoothing constraint is imposed using the Laplacian smoothing operator, ∇^2, and the relative strength of the smoothing is determined by γ.

The Hayward fault is represented by an 80-km-long by 12-km-deep fault plane discretized into 283 triangular subfaults with an average dimension of 3 km. The Hayward fault is meshed in this way in order to accommodate the divergence of the microseismicity at depth and the mapped surface trace as well as to incorporate subsurface salients which may affect the near-fault data. Additional model parameters include four deep, vertical dislocations located beneath the San Andreas, Hayward, Calaveras, and Greenville faults. Each deep fault extends far enough away from the modeled Hayward fault so as to avoid fault edge effects. The deep dislocations accommodate the regional strain gradient across the plate boundary. The BVLS approach allows for the right-lateral slip-rate to be bound within a range consistent with geologic estimates. Subfaults on the Hayward fault are bound between 0 and 12 mm/yr, which incorporates the inferred geologic rate of 9 mm/yr plus 3 mm/yr of error [*Lienkaemper et al.*, 1991]. Each deep dislocation is bound between 0 and 30 mm/yr. North of Point Pinole, little data exists that constrains the contemporary creep rate of the fault. The fault model is extended beneath San Pablo Bay and a zero slip condition is assigned to subfaults north of Pt. Pinole (km -10 to 0).

3.3.1 GPS Data Set

Surface displacements are measured using GPS from continuous stations maintained by the BARD network and campaign data collected by the USGS and UC Berkeley

from 1991 to 1999 [*Bürgmann et al.*, 2000]. All GPS data were processed using the Bernesse processing package. The horizontal components from 44 stations along with the full covariance matrix are used in the inversion (Figure 4.14 and Table 3.1).

3.3.2 InSAR Data Set

InSAR data provide a spatially continuous sampling of the deformation field along the line-of-sight from the satellite. Interferograms are produced using the Repeat Orbit Interferometry Package (ROI PAC) developed at JPL/Caltech. SAR data collected by the ERS1/2 satellite of the European Space Agency are processed using 8 looks in range and 40 looks in azimuth resulting in a pixel dimension of 150 m. Topography is removed using a 30-meter USGS digital elevation model. A dislocation model constrained by the GPS data is used to remove the interseismic gradient from each interferogram. Any remaining linear gradient, attributed to orbital errors, is removed and the interseismic signal is added back. The magnitude of the interseismic gradient is inconsequential in the inversion in that three model parameters are included that solve for the best fitting regional tilt and offset when fitting the InSAR data. Coherent InSAR data is limited to urban regions located primarily on the west side of the Hayward fault (Figure 3.2). Coverage extends across the fault in Pinole (km 0-5), Castro Valley (km 38-44), and Fremont (km 58-65). A more detailed account of the InSAR processing procedure can be found in Chapter 1.

A range-change rate is calculated by inverting 9 independent interferograms (i.e. interferograms which do not share common SAR data) for a linear rate. Only interferograms with a perpendicular baseline of less than 200 m and a temporal baseline of greater than 3 years were considered in this analysis. A final subset of interferograms were chosen such that

Table 3.1: GPS velocities used in the inversion.

| Station | Longitude | Latitude | Data (mm/yr) | | | Model (mm/yr) | |
			East	North	EN_{corr}	East	North
BRIB	-122.4551	37.8053	0	0	0	0	0
PRES	-122.3662	37.8100	-6.0±1.6	8.7±1.6	-25.6	-6.0	9.3
NAVY	-122.4189	37.8531	-4.4±1.9	9.1±2.1	-16.4	-5.0	8.0
PBL1	-122.4476	37.8909	-8.2±2.0	6.2±2.1	1.8	-5.3	8.1
TIBB	-122.2220	37.8836	-3.6±1.7	8.9±1.7	3.4	-5.3	7.9
BAPK	-122.2652	37.8718	1.2±2.2	3.4±2.2	-68.3	-0.7	2.0
UCBK	-122.1282	37.9369	-3.2±2.3	7.3±2.3	-34.0	-3.4	6.4
HILL	-122.3945	37.1830	2.2±2.1	0.5±2.2	-25.7	0.5	-1.1
PIGN	-122.3595	37.2284	-13.5±1.6	19.2±1.6	-21.1	-13.4	20.6
HLMR	-122.2841	37.2737	-11.2±1.5	22.1±1.5	-18.2	-12.9	19.9
HAUL	-122.2163	37.3123	-13.0±1.6	16.2±1.6	-17.7	-11.4	17.9
TRUE	-122.1672	37.3245	-9.6±1.5	14.0±1.5	-12.7	-9.1	14.8
PAWT	-122.1534	37.2902	-8.0±1.5	12.6±1.5	-14.0	-7.6	12.8
BM10	-122.1733	37.4269	-8.5±1.5	13.8±1.5	-16.4	-8.0	13.3
DURA	-122.1233	37.3627	-7.6±1.6	8.5±1.6	-0.0	-6.1	10.6
FOOT	-122.0349	37.4263	-6.1±1.5	9.6±1.5	-20.0	-6.1	10.7
BEND	-121.9737	37.4801	-5.0±1.5	6.6±1.5	-14.8	-4.1	8.1
Z137	-121.9188	37.5067	-4.2±1.6	6.1±1.6	-10.8	-2.8	6.2
ANTE	-121.8713	37.4989	-0.2±1.5	-0.0±1.6	-18.4	0.5	0.9
ALLI	-121.8698	37.5413	-0.9±1.6	-3.4±1.6	-27.8	0.7	0.8
SHER	-121.8099	37.5940	2.5±1.6	1.8±1.7	-38.3	1.6	-0.4
SANA	-121.7025	37.6218	2.3±1.7	-3.8±1.8	-53.8	3.0	-3.5

Table 3.1: Continued.

Station	Longitude	Latitude	Data (mm/yr)			Model (mm/yr)	
			East	North	EN$_{corr}$	East	North
USG7	-121.6754	37.6942	4.4±2.2	-7.7±2.5	-95.9	4.2	-6.4
BM11	-121.5663	37.7553	4.1±2.0	-8.6±2.1	-87.4	4.7	-7.4
MEDA	-122.5039	37.5091	5.0±1.9	-9.0±2.0	-60.1	5.1	-8.4
WHAL	-122.4562	37.5268	-10.1±2.2	17.3±2.4	-7.2	-11.9	17.9
PALB	-122.4581	37.6094	-9.3±2.1	14.5±2.2	-12.7	-10.6	16.1
SWEE	-122.3822	37.5922	-8.1±1.8	13.4±1.9	-28.3	-9.0	13.7
PEEE	-122.1837	37.6908	-6.2±2.4	9.0±2.5	-17.3	-7.7	11.9
SLBB	-122.1512	37.7097	-3.7±2.4	3.6±2.4	-7.6	-4.6	6.7
EBBB	-122.0692	37.7324	-0.2±3.1	2.6±3.2	-50.3	-3.8	6.0
CAS2	-122.0615	37.8150	1.2±1.5	-0.6±1.6	-10.0	-0.5	0.5
ROC2	-121.9949	37.7383	1.1±1.8	-2.6±1.8	-3.4	0.3	-1.0
WEID	-121.7925	37.9215	3.2±2.9	-5.5±3.0	-2.1	0.7	-1.6
JOBE	-121.7224	37.9540	5.2±2.3	-8.6±2.4	-43.1	4.5	-8.1
MINN	-123.0008	37.6972	4.5±2.3	-9.6±2.4	12.9	4.7	-8.5
FARB	-122.3899	37.1871	-13.2±1.5	21.5±1.5	-0.2	-14.4	20.9
PPT1	-122.1733	37.4269	-15.5±2.2	19.5±2.3	-0.7	-13.3	20.5
SUAA	-122.4199	37.9466	-7.3±1.8	10.0±1.7	6.0	-6.1	10.6
MOLA	-122.1406	37.6526	-2.6±1.7	8.4±1.7	2.2	-4.7	6.7
WINT	-122.1193	37.7241	-6.1±1.4	6.1±1.4	-0.6	-4.6	6.5
CHAB	-122.2463	37.9631	-2.5±1.5	2.1±1.6	-1.2	-1.4	2.0
NUNE	-121.9148	37.8819	1.8±2.9	5.3±2.9	9.2	-1.0	1.2
DIAB	-122.1525	37.9194	2.4±2.2	-7.5±2.3	18.4	3.3	-6.3

range-change rate [mm/yr]
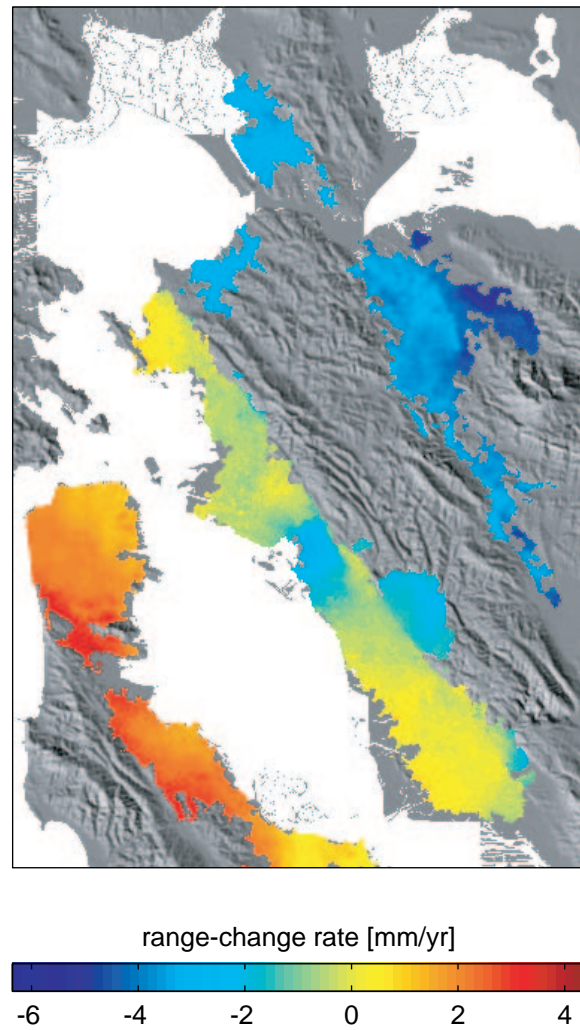
-6   -4   -2   0   2   4

Figure 3.2: A linear range-change rate is determined from 9 independent interferograms in the Bay Area from 1992 to 2000. A shaded relief map is shown in the background. InSAR data spans the fault at several locations, although coherence is limited primarily to developed regions for interferograms longer than a few months.

no SAR scene is duplicated in any of the interferograms. This ensures that interferograms with longer temporal baselines are preferentially selected and that atmospheric artifacts associated with any individual SAR scene are minimized. The final subset of interferograms used in this analysis is presented in Table 3.2. The average temporal baseline of the selected interferograms is 4.5 years, with the longest being 7 years. The relative errors are included in the weighted inversion by constructing a covariance matrix with the diagonal elements equal to 3 mm/yr and the off-diagonal elements set to zero.

The InSAR data are subsampled in a regular grid with a spacing of 1.5 km between points for regions within 15 km of the Hayward fault. At distances greater than 15 km, the InSAR data are subsampled at a 3 km spacing, resulting in a cumulative sampling of 211 points. Each subsampled point represents an average of 9 surrounding pixels in an effort to avoid outliers. For the inversion, InSAR data are truncated south of Union City (> km 50) to avoid time-dependent deformation on the southern Hayward fault. Data on the west side of the fault near San Leandro (km 28-34) are also excluded from the inversion because the deformation is believed to include uplift of a Pliocene basin [*Marlow et al.*, 1999] due to groundwater recharge.

3.3.3   Surface Creep Rates

Surface creep rates are obtained from alignment array measurements along the Hayward fault (Figure 3.3c) [*Lienkaemper et al.*, 1991; *Lienkaemper and Galehouse*, 1997]. The average creep rate along the fault is 5 mm/yr with a distinctive low near Oakland (km 20-30) and anomalous high of 9 mm/yr (pre-Loma Prieta earthquake rate) south of Fremont(km 65-70). Four creepmeters are also located along the fault [*Bilham and White-*

Table 3.2: List of stacked interferograms. Data collected by the ERS1/2 spacecraft along frames 2835-2853.

Date1 YYYYMMDD	Date2 YYYYMMDD	Track	Sat 1	Orbit 1	Sat 2	Orbit 2	Perpendicular Baseline (m)	Δt (yr)
19920420	19951026	342	ERS1	3994	ERS2	2701	74	3.5
19920610	19971011	70	ERS1	4724	ERS2	12950	3	5.3
19920923	19991016	70	ERS1	6227	ERS2	23471	100	7.0
19930301	19980423	342	ERS1	8503	ERS2	15727	38	5.1
19930405	19990930	342	ERS1	9004	ERS2	23242	68	6.4
19930614	19970508	342	ERS1	10006	ERS2	10717	136	3.8
19960329	19991120	70	ERS1	24607	ERS2	23972	89	3.6
19960504	19990529	70	ERS2	5435	ERS2	21467	36	3.0
19970104	20000408	70	ERS2	8942	ERS2	25976	92	3.3

head, 1997]. The three creepmeters located north of Fremont all exhibit quasi-constant creep rates. Updated rates averaged over 5 to 30 years of data at 18 sites measured by *Lienkaemper et al.* [2001] are used in the inversion (Table 3.3).

3.3.4 Seismic Repeater Rates

Characteristic repeating earthquakes (CREs), or repeaters, are small magnitude events (**M**1-2) with regular recurrence intervals and identical event locations. These event sequences have waveforms with high cross-correlation values (>0.98). *Nadeau et al.* [1995] first identified CREs along the San Andreas fault near Parkfield. *Nadeau and Johnson*[1998] interpreted these events to represent small asperities that are loaded by creep on adjacent portions of the fault. One of the implications of this model is that a relatively large moment release for a small asperity size suggests a high stress drop. *Sammis and Rice* [2001] argue that these events may not represent small strong asperities, but rather outline the boundary between locked and creeping regions. An alternative explanation was also proposed by *Beeler et al.*[2001] where the asperity undergoes both coseismic and aseismic slip.

Nadeau and McEvilly [1999] developed an empirical relationship from the seismic data set in Parkfield to estimate the slip-rate at the event location based on the seismic moment release. More recently, CREs have been identified on the Hayward fault and are used to infer the slip-rate at depth (Figure 3.3a) [*Bürgmann et al.*, 2000]. Regardless of the slip-rates estimated using this technique, the presence of the CRE sequences implies that nearby regions of the fault are creeping aseismically and that deep sections of the Hayward fault are not fully locked. Slip-rates from 35 CRE sequences are used as an additional constraint in the inversion (Table 3.4).
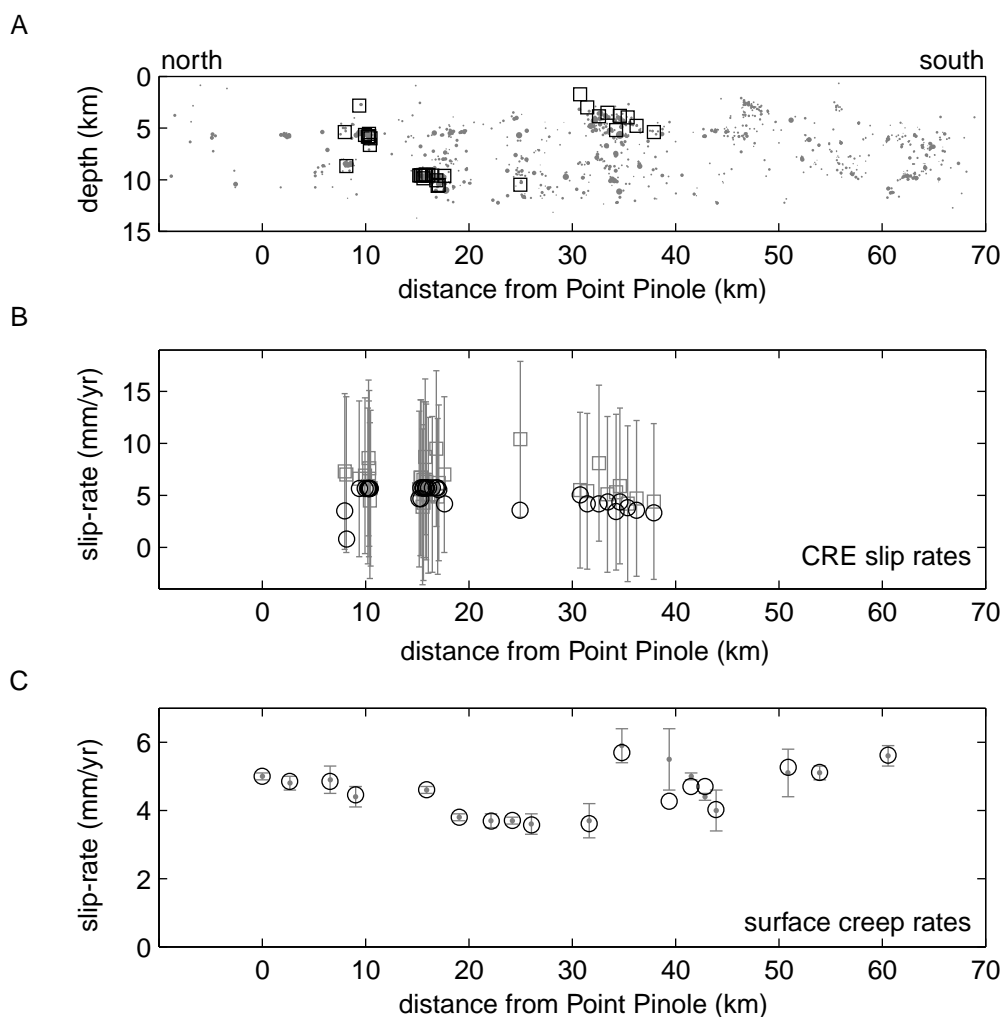
Figure 3.3: (A) The relocated seismicity (gray dots) of *Waldhauser and Ellsworth* [2002] is projected onto the Hayward fault. Characteristic repeating earthquake (CRE) sequences are clustered beneath El Cerrito (km 10), Berkeley (km 18), and San Leandro (km 33) (open squares). (B) Slip-rates inferred from the CRE sequences are plotted with their error estimates (gray open squares with error bars). The slip-rates are compared to model results (bold open circles) for the slip-rate distribution in Figure 3.6b. (C) Surface creep-rate measurements (gray dots with error bars) collected by *Lienkaemper et al.*[2001] are displayed according to their location along the Hayward fault. Model results (bold open circles) correspond to the slip-rate distribution of Figure 3.6b.

3.4   Inversion Results

The available data sets contribute in different ways to the model resolution of the inversion. The model resolution for the combined data sets show that model parameters are well resolved in the top portion of the fault plane and become less resolved below ~6 km, except where CRE estimates are available. Poorly resolved sections of the model include the region at depth south of Union City (> km 50) and north of Pt. Pinole (< km 0). The individual contribution from the GPS and InSAR data are evaluated by performing independent inversions. The sparse, yet precise nature of the GPS data provide good constraint on the slip-rates for the deep faults while providing minimal constraint to the discretized Hayward fault except where a GPS station is close to the surface trace of the fault (Figure 3.4a). The inversion of the GPS data prefer >8 mm/yr near Berkeley and Fremont in the top few kilometers of the fault. These locations correlate with regions where GPS stations are located near the fault trace (at km 15, 35, and 65). The InSAR data provide better resolution on the Hayward fault. Inversions using only the InSAR data prefer 4-8 mm/yr in the full depth extent below Pt. Pinole (km 0) and >10 mm/yr south of Union City (> km 50) (Figure 3.4b). However, these regions are also characterized by low model resolution.

The residual sum of squares (RSS) as a function of the relative weighting between the GPS and InSAR data sets shows that the GPS data are largely insensitive to shallow slip imposed by the InSAR data (Figure 3.5a). The InSAR data are weighted by a factor of 2 relative to the GPS data. The surface and CRE determined slip-rates provide a direct constraint on the corresponding subfault. Therefore, these data are distinctively different
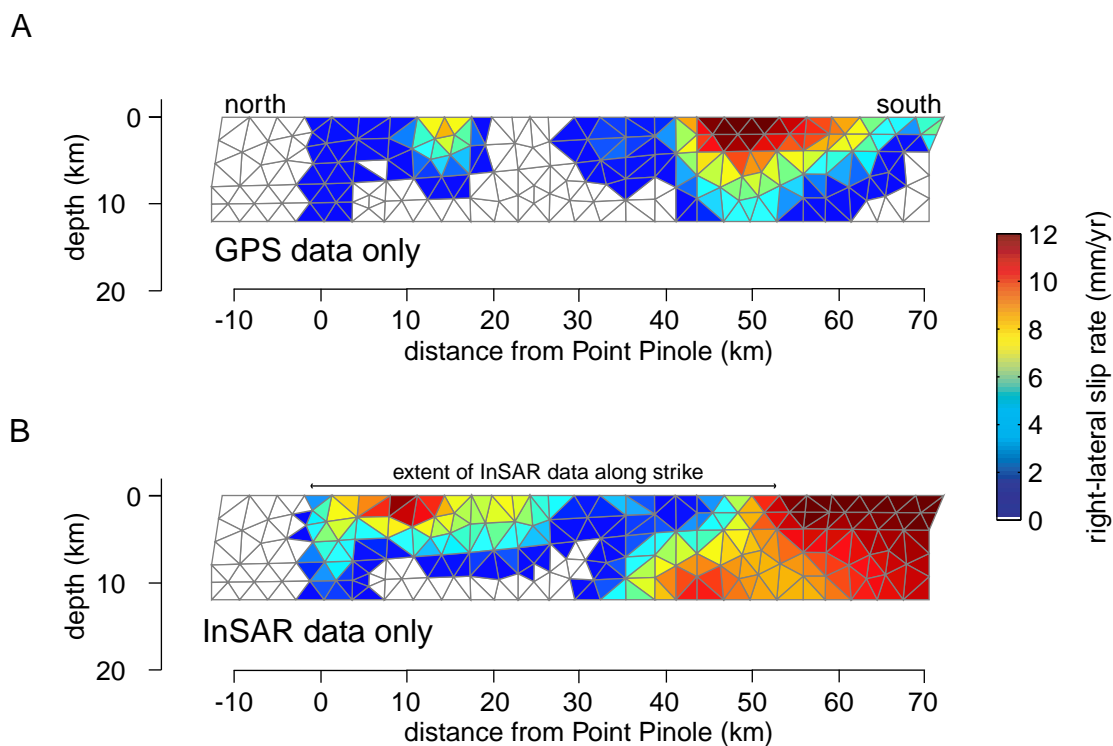
Figure 3.4: The slip distribution using (A) only the GPS data and (B) only the InSAR data establishes the contribution from each data set. Triangular subfaults with zero inferred slip-rate are plotted in white. Zero slip-rate is imposed on subfaults north of Pt. Pinole ($<$ km 0).

from surface displacement-rate observations from GPS and InSAR which are mapped to slip-rate on the subfault using the elastic Green's functions. Holding the relative weighting of the GPS and InSAR data fixed, the weight applied to the surface and CRE slip-rate estimates are chosen such that the fit to the GPS and InSAR data does not degrade significantly (Figure 3.5b). The inclusion of the surface and CRE determined creep rates increase the RSS of the GPS and InSAR data by $\sim 1\%$ relative to an inversion using solely the GPS and InSAR data. The relative weights of the surface creep rates and the CRE rates are 0.4 and 0.8, respectively.

The inversion result utilizing all data shows a heterogeneous slip-rate distribution. Results are presented for three smoothing weights (Figure 3.6a-c). The smoothing weight, γ, is evaluated from the tradeoff between model roughness, $\|\nabla^2 \mathbf{m}\|_2$, and the residual sum of squares (Figure 3.6d). A rate of <1 mm/yr is found below and to the north of the San Leandro seismic cluster (km 33). This feature is consistent regardless of the relative weights of the data sets or the degree of smoothing. The 6 mm/yr rate found adjacent to the Berkeley seismic cluster (km 18) at a depth of $\sim$10 km is largely constrained by the CRE slip estimates. The slip-rates for the deep dislocations correspond to 6.6±2.2, 21.9±1.6, 17.1±4.7, and 2.5±4.5 mm/yr for the Hayward, San Andreas, Calaveras, and Greenville faults, respectively. These slip-rates remain consistent regardless of the choice of smoothing parameter and are largely dependent on the weight chosen for the InSAR data relative to the GPS data. While these rates agree reasonably well with previously published rates, they are not the focus of this study and only serve the purpose of constraining the regional deformation field.
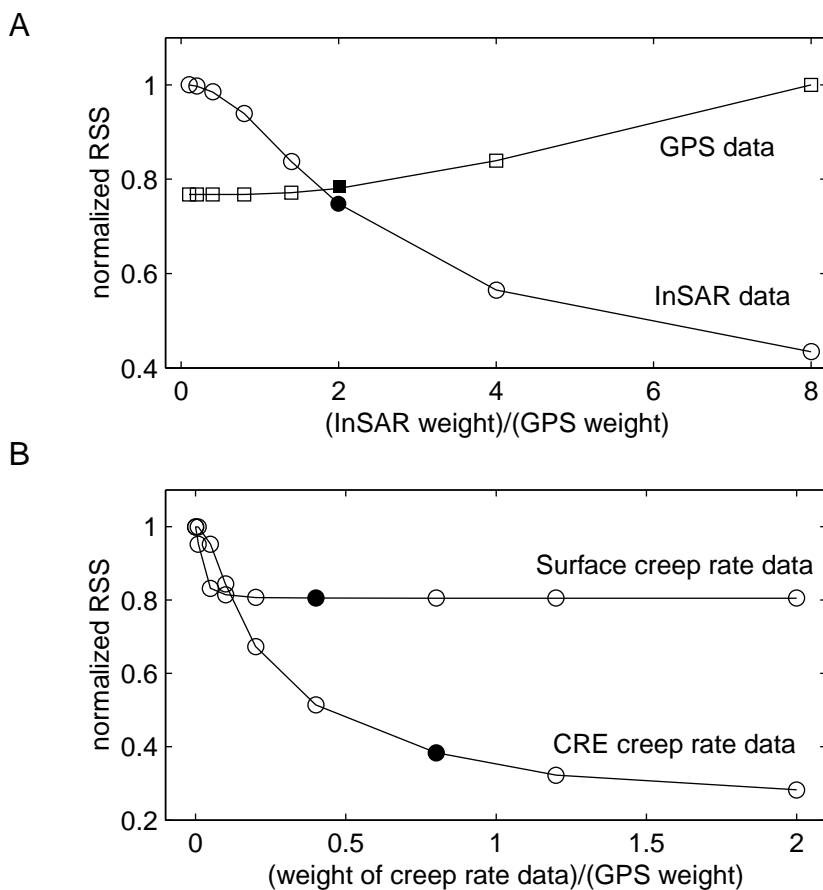
Figure 3.5: (A) The relative weighting of the InSAR data to the GPS data is determined by examining the normalized residual sum of squares (RSS) for the two data sets. Parameter choices used in the inversion are represented by a closed circle or square. A weight of 2 is chosen for the InSAR data. (B) A similar analysis is performed to determine the weighting applied to the slip-rates from both surface observations and CRE estimated rates. A weighting factor of 0.4 and 0.8, respectively, is chosen for each data set.

A

B

C

D
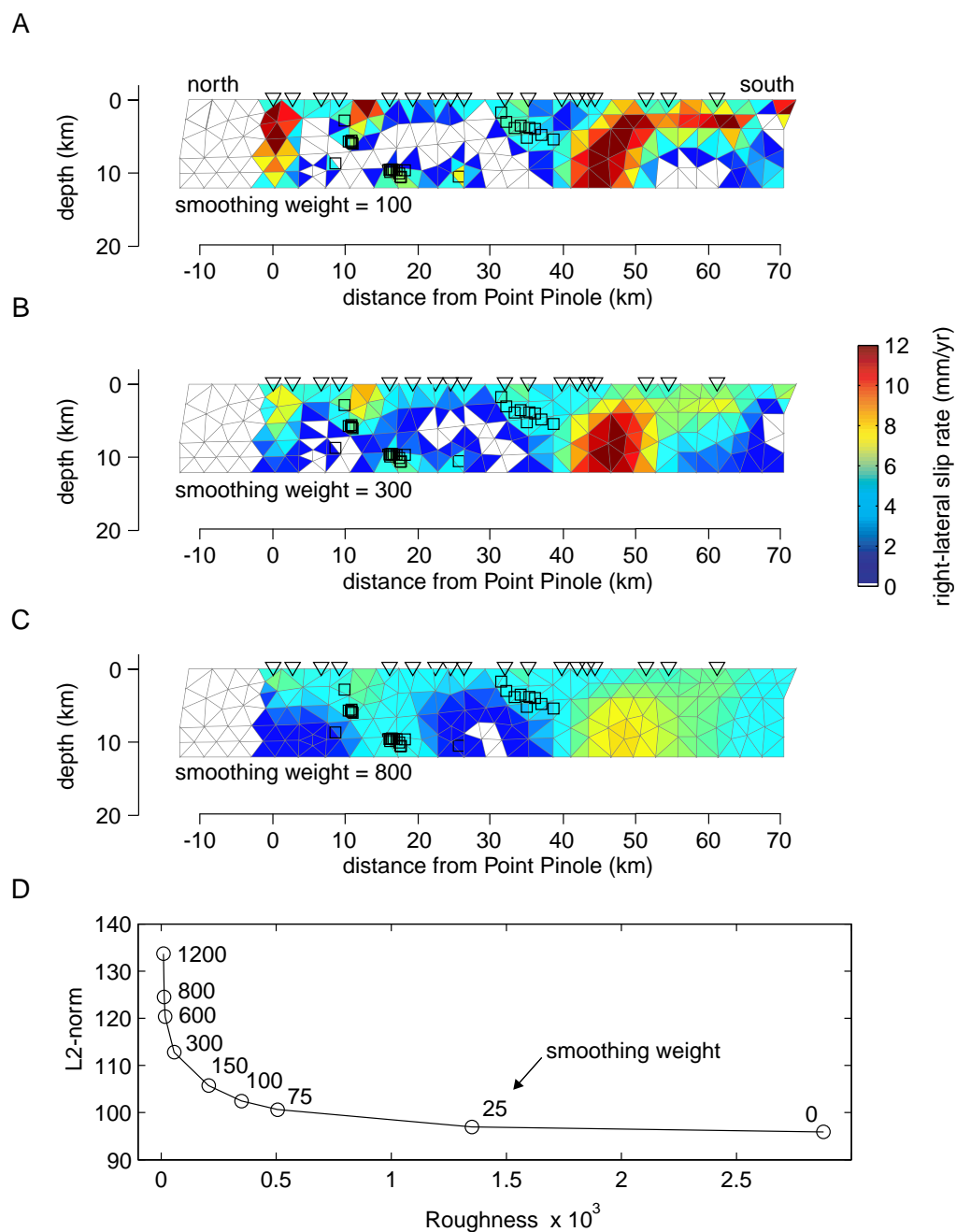
Figure 3.6: The combined data set are inverted for the slip-rate distribution on the Hayward fault. Results for three different smoothing weights are shown: (A) γ=100, (B) γ=300, and (C) γ=800. Open triangles and open squares denote the location of surface and CRE determined slip-rates. InSAR data is used between 0 and 50 km along the strike of the fault. (D) The smoothing weight, γ, is evaluated by plotting the trade-off between the weighted RSS and the roughness of the model parameters.

The fits to the various data sets for the slip-rate distribution using γ=300 are shown in Figure 3.3b-c and Figure 3.7. The surface creep data are well modeled. However, an anomalous, high rate of >6 mm/yr is observed where a gap in the surface creep observations exists (at km 12). This appears to be driven by the pair of GPS data that span the fault at Berkeley. The greatest misfit in the GPS data exists at stations along the northern Hayward fault, although this misfit is within the error of the observation. InSAR residuals are greatest across the northern Hayward fault where the model under-predicts the offset in range-change rate across the fault.

Waldhauser and Ellsworth [2002] suggest that the Hayward fault microseismicity outlines four quiescent regions that represent locked asperities (see Figure 10 in *Waldhauser and Ellsworth* [2002]). They hypothesize that the seismic lineations found within the El Cerrito and Berkeley clusters (km 10 and 18) delineate an elongated asperity extending along the northern 20 km of the fault within a depth range of 6-8 km. Additional proposed asperities are located north of the San Leandro cluster (km 30), at depth below Hayward (km 40-50), and a small asperity beneath Fremont (km 62). This model is tested by imposing a zero-slip constraint on subfaults that correspond to the identified regions (Figure 3.8b). Additional slip-rate is forced into the shallow portion of the fault resulting in concentrations as high as 9 mm/yr. While the L2-norm increases with the additional constraints, the weighted variance, (L2-Norm)/(degrees of freedom), improves (Table 3.5). A F-test is performed to determine whether the change in fit is significant given the change in the degrees of freedom. There exists some flexibility in the calculation of the F-ratio depending on how the smoothing constraint and zero-slip constraints are used to determine the degrees
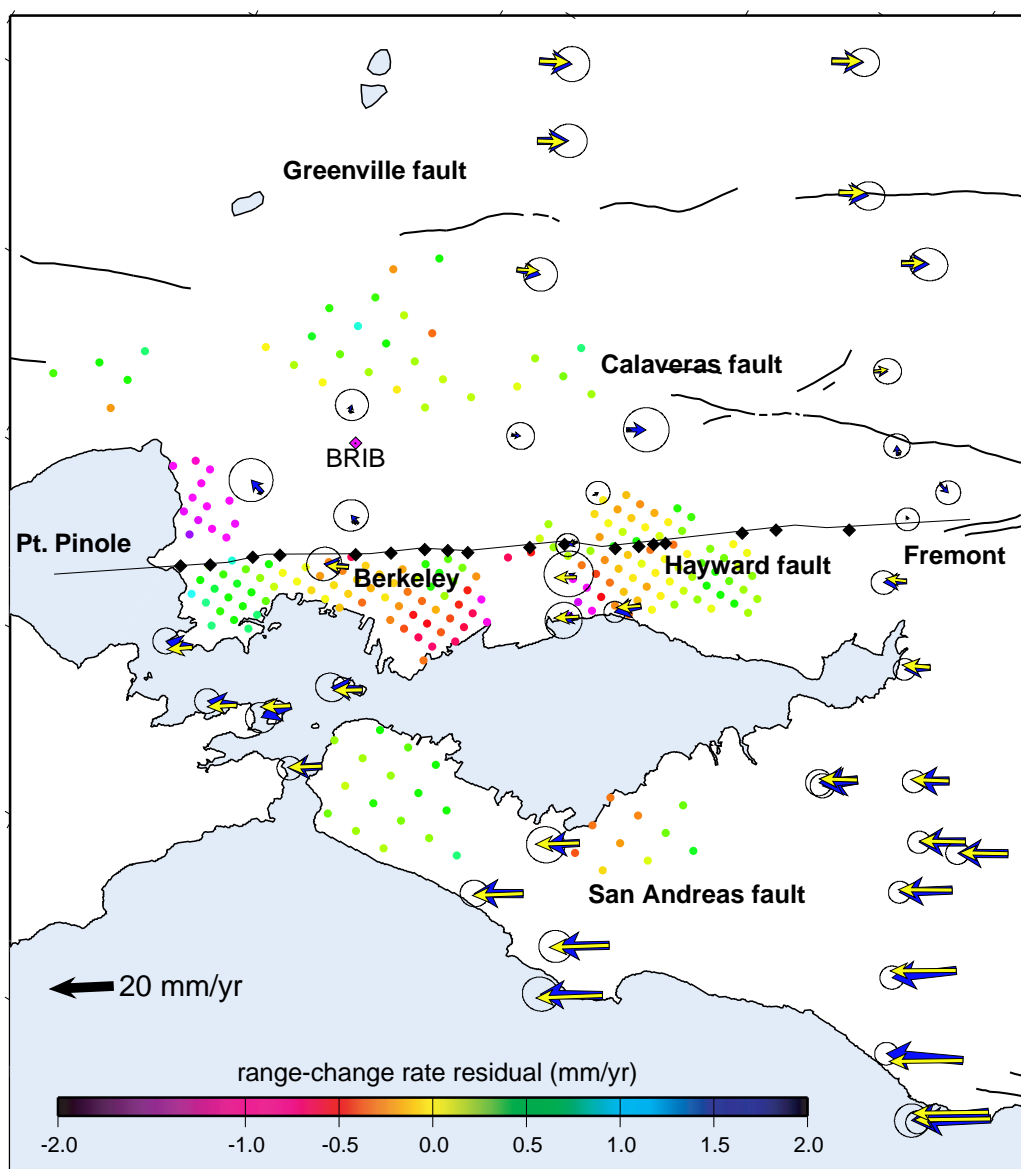
Figure 3.7: GPS data (blue arrows) and their 2-sigma error ellipses are compared to the predicted velocities (gold arrows). InSAR residuals (colored dots) show that misfits are generally less than ±1 mm/yr of range-change rate. Model predictions correspond to the distribution shown in Figure 3.6b.

of freedom. Smoothing and zero-slip constraints are parameterized as independent data constraints in determining the F-ratio. The F-ratio for the models in Figures 3.8a and 3.8b is found to be 1.09. Ratios less than 1.18 are within the 95% confidence interval, suggesting that statistically these models cannot be differentiated and the increase in the L2-norm could simply reflect random fluctuations in the data. While localized locked patches may exist as suggested by *Wadlhauser and Ellsworth,* [2002], the data are not sufficient to resolve the slip-rate distribution at the necessary level of detail.

Given that the geodetic data are insensitive to slip at the base of the seismogenic zone, I evaluate whether the data can be modeled solely by slip in the upper few kilometers of the fault. An inversion is performed where zero slip is enforced on all subfaults below a depth of 7 km (Figure 3.8c). The slip-rate distribution looks very similar to the distribution found for Figure 3.8b. However, additional slip-rate is forced to the subsurface south of km 40. The F-ratio for the model with no slip below 7 km versus an unconstrained model is found to be 1.23. The 95% confidence ratio is 1.17 suggesting that these models are statistically distinct. The improvement in fit is attributed to the redistribution of slip-rate from the 7-12 km depth section on the Hayward fault to the deep dislocation. Slip-rate on the deep dislocation beneath the Hayward fault increases from 6.6±2.2 mm/yr to 7.7±1.9 mm/yr which better fits the far-field GPS data. Removing the zero slip constraint on subfaults at depth on the northern Hayward fault (Figure 3.8d) results in a F-ratio of 1.16. However, the improvement may not be statistically significant given that the 95% confidence threshold is 1.18.

A unrestricted model

B after *Waldhauser and Ellsworth* [2002]

C locked below 7 km depth

D locked south of Berkeley
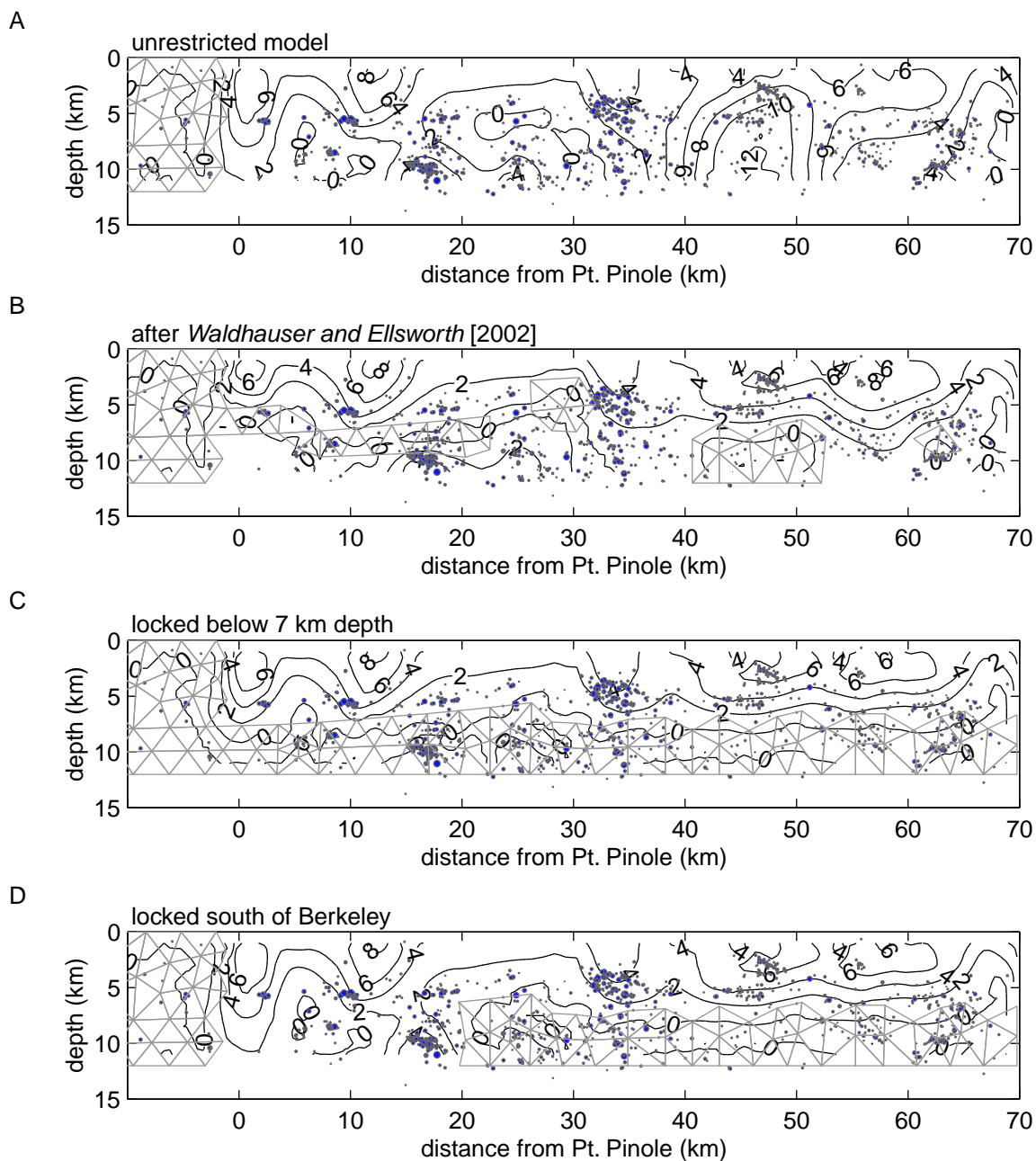
Figure 3.8: The slip-rate distribution shown for various model parameterizations. Slip-rate is contoured in intervals of 2 mm/yr. Subfaults constrained to zero slip are shown as gray triangles. (A) The contoured slip-rate distribution of Figure 3.6b is compared to the relocated seismicity (gray dots) of *Waldhauser and Ellsworth* [2002]. (B) Zero slip-rate is imposed on subfaults that correspond with the asperities suggested by *Waldhauser and Ellsworth* [2002]. (C) Zero slip is imposed on subfaults below a depth of 7 km to assess the sensitivity of the data to slip-rate on the lower portion of the fault. (D) Finally, slip-rate at depth on the northern Hayward fault is evaluated by locking the fault south of Berkeley (km 20).

3.5   Discussion

The distribution of aseismic slip-rate on the Hayward fault suggests spatially variable fault behavior consistent with the findings of previous studies [*Lienkaemper et al.*, 1991; *Simpson et al.*, 2001]. A slip-rates <1 mm/yr likely represents regions where the fault is not slipping either because the fault is locked or because slip is restrained. Locked sections may represent the nucleation site or the rupture area of future large earthquakes. The <1 mm/yr region below Oakland and at depth on the southern Hayward fault (km 20-35) agree with findings by *Simpson et al.* [2001], *Wyss* [2001], and *Waldhauser and Ellsworth* [2002, asperities B and C in Figure 10].

The inversion places >7 mm/yr on the northern portion of the fault plane beneath Pt. Pinole (km 0). The slip-rate patch extends from the top to the bottom of the model and is flanked to the south by a <2 mm/yr slip-rate patch at kilometer 10. This alternating pattern may reflect the asymmetric coverage of InSAR data on the east side of the fault. However, all of the individual data sets prefer an appreciable slip-rate at depth below Pt. Pinole (km 0). The model under-predicts the offset in range-change across the fault at Pinole by as much as 1 mm/yr. With higher smoothing strengths, inversion results converge to a model where the upper 6 km of the northern Hayward fault, extending to greater depth near the Berkeley seismic cluster (km 18), slips at ~5 mm/yr. Hopefully, recently collected GPS data at new benchmarks may help to provide additional constraints.

Inspection of the InSAR data near Pt. Pinole (km 0) is consistent with block-like motion across the fault. A localized increase in range-change from ~4 mm/yr to ~6 mm/yr is found along the west side of the fault from Berkeley to Pt. Pinole is resolved by the

InSAR data (Figure 3.2). It is possible that the range-change signal across the fault includes a vertical component. Approximately 1 mm/yr of range-change rate would correspond to 3.5 mm/yr of right-lateral deformation or 1.07 mm/yr of vertical deformation. However, no offset at the trace of the fault is found in the few ascending interferograms, suggesting that the displacements are predominately horizontal. Land subsidence of the region to the west of the fault would increase the range-change and imply a higher rate of right-lateral offset. However, no clear evidence for a long-term land subsidence signal is observed. A fog bank whose extent would be limited by the uplifted hills to the west would also increase the range-change if the fog coincided with the acquisition of the second SAR scene in a given interferogram. The InSAR data for this region are collected at 11am or 12pm local time when the fog has typically retreated to the coast. While the >7 mm/yr slip-rate below Pt. Pinole is high compared to the surface creep-rate observations, convincing evidence is not available to discredit the InSAR data across the northern Hayward fault.

The low slip-rate of <2 mm/yr below Oakland and San Leandro (km 20-40) remains a robust feature of the inversion and suggests that this region is locked. While it is difficult to infer the variation in geology at depth along the fault, evidence does exist for a large mafic body along this segment. Using magnetic and gravity data, *Ponce et al.* [*in press*] resolve a tabular, mafic body that dips 75-80° to the northeast and extends to depths greater than 6 km. The microseismicity locates along the western edge of the mafic body. *Ponce et al.* [*in press*] propose that the mafic body, composed of gabbro which outcrops on the surface, acts to impede slip at depth. In the top few kilometers, aseismic slip occurs where the fault bisects the mafic body. Although it is difficult to know the location of the

active trace at depth with respect to the gabbro, these observations argue that material properties play a role in aseismic versus seismic behavior.

The presence of a large rigid body could also control the geometry of the through going fault. The geometry of the fault as revealed by high-resolution seismic relocations outline a complex surface at depth. Geometric irregularities in the fault surface would result in a heterogeneous stress field and may be responsible for the variability in slip-rate. However, it is difficult to test this hypothesis without a greater understanding of the exact fault structure at depth. *Waldhauser and Ellsworth* [2002] discuss how the microseismicity appears to cluster along the fault at regular intervals. Perhaps this suggests that we are currently observing a snapshot in the evolving state of the Hayward fault zone.

3.6   Conclusions

The inversion of space-geodetic data, surface creep-rate measurements, and CRE slip-rate estimates reveals a heterogeneous slip-rate distribution. Slip-rates <2 mm/yr are found to correlate with the presumed source region of the 1868 earthquake on the southern Hayward fault and suggest that strain is currently accumulating at depth on this section of the fault. The fact that the source region of the 1868 earthquake remains locked suggests that the coseismic release of strain is the characteristic mode of deformation on this segment. Regions that exhibit interseismic slip are less likely to be the point of nucleation for future ruptures. However it is unknown whether these regions may release accumulated slip deficit in a coseismic event or through accelerated creep.

Calculating the actual seismic potential of the Hayward fault is problematic be-

cause the characteristic mode of deformation is not known for much of the fault. The 1868 earthquake along the central portion of the fault argues that this section of the fault is capable of producing large events. Paleoseismic data on the Hayward fault suggests that large events on the northern segment are possible [*Hayward Fault Paleoearthquake Group*, 1999]. However the issue of whether interseismic surface creep, afterslip, or coseismic surface rupture can be unequivocally differentiated in a trench has yet to be resolved [*Kelson and Baldwin*, 2001]. If the northern segment is incapable of initiating a large event, it remains unclear how the fault might respond during a rupture on the Rodgers Creek fault to the north or on the southern portion of the Hayward fault. Perhaps the cessation of rupture near Oakland for the 1868 earthquake [*Yu and Segall*, 1996] demonstrates the presence of a natural boundary such as the mafic body as suggested by *Ponce et al.* [*in press*]. Unfortunately, no record of the creep rate on the northern Hayward exists following that 1868 event. If accelerated creep had been observed on the fault, then the mode of strain release for the northern Hayward would likely be resolved.

3.7 Acknowledgments

Table 3.3: Surface creep data from *Lienkaemper et al.* [2001] and the model result.

Longitude	Latitude	Creep Rate (mm/yr)	Model (mm/yr)
-122.3546	37.9891	5.0±0.1	5.0
-122.3379	37.9690	4.8±0.2	4.8
-122.3083	37.9425	4.9±0.4	4.9
-122.2918	37.9246	4.4±0.3	4.5
-122.2506	37.8719	4.6±0.1	4.6
-122.2304	37.8484	3.8±0.1	3.8
-122.2090	37.8264	3.7±0.2	3.7
-122.1975	37.8101	3.7±0.1	3.7
-122.1882	37.7951	3.6±0.3	3.6
-122.1504	37.7546	3.7±0.5	3.6
-122.1285	37.7319	5.9±0.5	5.7
-122.1045	37.6950	5.5±0.9	4.3
-122.0899	37.6798	5.0±0.1	4.7
-122.0804	37.6703	4.4±0.1	4.7
-122.0727	37.6627	4.0±0.6	4.0
-122.0222	37.6143	5.1±0.7	5.3
-122.0008	37.5925	5.1±0.2	5.1
-121.9607	37.5422	5.6±0.3	5.6

Table 3.4: Deep slip-rates inferred from characteristic repeating earthquake sequences.

Longitude	Latitude	Depth (km)	Slip-rate (mm/yr)	Model (mm/yr)
-122.1463	37.7463	3.85	8.1±7.5	4.2
-122.2808	37.9156	6.63	4.5±7.5	5.7
-122.1634	37.7570	1.73	5.5±7.5	5.0
-122.2428	37.8766	9.55	6.3±7.5	5.7
-122.2448	37.8794	9.57	3.9±7.5	5.7
-122.2455	37.8806	9.56	6.7±7.5	5.7
-122.1177	37.7223	4.79	4.7±7.5	3.6
-122.1048	37.7112	5.39	4.4±7.5	3.3
-122.1249	37.7278	3.96	4.2±7.5	3.8
-122.2464	37.8820	9.58	5.6±7.5	4.7
-122.1322	37.7360	5.18	5.3±7.5	3.5
-122.2826	37.9136	5.98	5.7±7.5	5.7
-122.1298	37.7332	3.81	5.9±7.5	4.3
-122.1398	37.7410	3.52	5.1±7.5	4.3
-122.2850	37.9153	5.81	5.9±7.5	5.7
-122.2442	37.8788	9.85	4.3±7.5	5.7
-122.2897	37.9355	8.68	7.0±7.5	0.8
-122.2380	37.8670	10.59	4.9±7.5	5.7
-122.2458	37.8809	9.58	6.7±7.5	4.7
-122.2328	37.8629	9.62	7.0±7.5	4.2
-122.2372	37.8664	10.51	6.2±7.5	5.5
-122.2418	37.8749	9.55	5.0±7.5	5.7
-122.2395	37.8719	9.60	5.1±7.5	5.7
-122.1986	37.8010	10.47	10.4±7.5	3.6
-122.2836	37.9149	5.56	6.6±7.5	5.7
-122.1559	37.7536	3.00	5.4±7.5	4.2
-122.2841	37.9144	5.80	7.6±7.5	5.7
-122.2875	37.9169	5.67	6.9±7.5	5.7
-122.2443	37.8786	9.54	6.5±7.5	5.7
-122.2430	37.8768	9.49	6.5±7.5	5.7
-122.2958	37.9185	2.83	6.6±7.5	5.7
-122.3031	37.9300	5.39	7.3±7.5	3.5
-122.2377	37.8687	10.05	9.5±7.5	5.7
-122.2844	37.9148	5.84	8.6±7.5	5.7
-122.2434	37.8773	9.54	8.7±7.5	5.7

Table 3.5: Statistical data for inversion results.

Description[b]	RSS(mm^2)/N^a				L2-Norm	L2-Norm/DOF^c
	InSAR	GPS	Surface rates	CRE rates		
GPS only	-	2.369	-	-	-	0.690
InSAR only	0.151	-	-	-	-	0.066
Unrestricted Model	0.216	2.594	0.100	5.375	112.8	0.297
After *Waldhauser and Ellsworth*[2002]	0.236	2.568	0.096	5.455	115.8	0.273
Zero slip below ∼7 km	0.227	2.556	0.094	3.743	112.6	0.242
Locked south of Berkeley	0.227	2.568	0.094	5.007	114.5	0.256

^{a}N = number of data.

^{b}Results for a smoothing weight of 300.

^{c}DOF = (number of constraints - number of model parameters).

Bibliography

Andrews, D. J., Oppenheimer, D. H., and J. J. Lienkaemper, The Mission link between the Hayward and Calaveras faults, *J. Geophys. Res., 98,* 12083-12095, 1993.

Bakun, W. H., Seismic Activity of the San Francisco Bay Region, *Bull. Seism. Soc. Am., 89,* 764-784, 1999.

Bawden, G. W., Thatcher, W., Stein R. S., Hudnut K. W., and G. Peltzer, Tectonic contraction across Los Angeles after removal of ground water pumping effects, *Nature, 412,* 812-815, 2001.

Beeler, N. M., Lockner, D. L., and S. H. Hickman, A simple stick-slip and creep-slip model for repeating earthquakes and its implications for microearthquakes at Parkfield, *Bull. Seism. Soc. Am., 91,* 1797-1804, 2001.

Bilham, R., Surface slip subsequent to the 24 November 1987 Superstition Hills, California, earthquake monitored by digital creepmeters, *Bull. Seism. Soc. Am., 79,* 424-450, 1989.

Bilham, R., and S. Whitehead, Subsurface creep on the Hayward fault, Fremont, California, *Geophys. Res. Lett., 24,* 1307-1310, 1997.

Bürgmann, R., Ergintav, S., Segall, P., Hearn, E., McClusky, S., Reilinger, R., Woith, H., and J. Zschau, Time-dependent distributed afterslip on and deep below the Izmit earthquake rupture, *Bull. Seism. Soc. Am., 91,* 126-137, 2002.

Bürgmann, R., Schmidt, D., Nadeau, R. M., d'Alessio, M., Fielding, E., Manaker, D., McEvilly, T. V., and M. H. Murray, Earthquake potential along the northern Hayward Fault, California, *Science, 289,* 1178-1182, 2000.

Chapman, R. H., and C. C. Bishop, Bouguer gravity map of California: Santa Rosa, 1x2-degree sheet, scale 1:250,000, *Reg. Geol. Map Ser. Map 2B,* Calif. Div. Mines and Geol., Sacramento, 1988.

Comninou, M., and J. Dundurs, Angular dislocations in a half space, *J. Elasticity, 5,* 203-216, 1975.

Dragert, H., Wang, K. L., and T. S. James, A silent slip event on the deeper Cascadia subduction interface, *Science, 292,* 1525-1528, 2001.

Galehouse, J. S., Data from theodolite measurements o f creep rates on San Francisco Bay Region faults, California: 1979-2001, *U.S. Geol. Surv. Open File Rep., 02-225*, 2002.

Graymer, R. W., Jones, D. L., and E. E. Brabb, Geologic map of the Hayward fault zone, Contra Costa, Alameda, and Santa Clara Counties, California: A digital database, *U.S. Geol. Surv. Open File Rep., 95-597*, 1995.

Graymer, R. W., Neogene development of the Hayward fault zone- A different perspective on an active strike-slip fault, unpublished manuscript.

Harris, R. A., and P. Segall, Detection of a locked zone at depth on the Parkfield, California, segment of the San Andreas fault, *J. Geophys. Res., 92*, 7945-7962, 1987.

Hayward fault Paleoearthquake Group, Timing of paleoearthquakes on the northern Hayward fault- preliminary evidence in El Cerrito, California, *U.S. Geol. Surv. Open File Rep., 99-318*, 1999.

Horowitz, F. G., and A. Ruina, Slip Patterns in a spatially homogeneous fault model, *J. Geophys. Res., 94*, 10279-10298, 1989.

Kelson, K. I., and J. N. Baldwin, Can paleoseismic techniques differentiate between aseismic creep and coseismic rupture?, *Seism. Soc. of America, 96th Annual Meeting, San Francisco, Ca.*, 2001.

Lawson, A. C. (Ed.), *The California Earthquake of April 18, 1906, Report of the State Earthquake Investigation Comission,* vol. 1, Carnegie Inst. of Washington, Washington, D. C., 1908.

Lienkaemper, J. J., Map of recently active traces of the Hayward fault, Alameda and Contra Costa counties, California, *U. S. Geolol. Surv.,* Map MF-2196, 1992.

Lienkaemper, J. J., and G. Borchardt, Holocene slip rate on the Hayward fault at Union City, California, *J. Geophys. Res., 101*, 6099-6108, 1996.

Lienkaemper, J. J., Borchardt, G., and M. Lisowski, Historic creep rate and potential for seismic slip along the Hayward fault, California, *J. Geophys. Res., 96*, 18261-18283, 1991.

Lienkaemper, J. J., and J. Galehouse, Revised long-term creep rates on the Hayward fault, Alameda and Contra Costa Counties, California, *U.S. Geol. Surv. Open File Rep., 97-690*, 1997.

Lienkaemper, J. J, and J. Galehouse, New evidence doubles the seismic potential of the Hayward fault, *Seism. Res. Lett., 69*, 519-523, 1998.

Lienkaemper, J. J., Galehouse, J. S., and R. W. Simpson, Creep response of the Hayward Fault to stress changes caused by the Loma Prieta earthquake, *Science, 276*, 2014-2016, 1997.

Lienkaemper, J. J., Galehouse, J. S., and R. W. Simpson, Long-term monitoring of creep rate along the Hayward fault and evidence for a lasting creep response to 1989 Loma Prieta earthquake, *Geophys. Res. Lett., 28,* 2265-2268, 2001.

Lienkaemper, J. J., and P. L. Williams, Evidence for surface rupture in 1868 on the Hayward fault in north Oakland and major rupturing in prehistoric earthquakes, *Geophys. Res. Lett., 26,* 1949-1952, 1999.

Linde, A. T., Gladwin, M. T., Johnston, M. J. S., and R. L. Gwyther, A slow earthquake sequence on the San Andreas fault, *Nature, 383,* 65-68, 1996.

Malservisi, R., Gans, C., and K. P. Furlong, Numerical modeling of creeping faults and implications for the Hayward fault, California, submitted to *Tectonophysics*, 2001.

Marlow, M. S., Jachens, R. C., Hart, P. E., Carlson, P. R., Anima, R. J., and J. R. Childs, Development of San Leandro synform and neotectonics of the San Francisco Bay block, Claifornia, *Marine Petrl. Geology, 16,* 431-442, 1999.

Marone, C., Laboratory-derived friction laws and their application to seismic faulting, *Annu. Rev. Earth Planet. Sci., 26,* 643-696, 1998.

Marone, C., and C. H. Scholz, The depth of seismic faulting and the upper transition from stable to unstable slip regimes, *Geophys. Res. Lett., 15,,* 621-624, 1988.

Marone, C., Raleigh, C. B., and C. H. Scholz, Frictional behavior and constitutive modeling of simulated fault gouge, *J. Geophys. Res., 95,* 7007-7025, 1990.

Miller, M. M., Melbourne, T., Johnson, D. J., and W. Q. Sumner, Periodic slow earthquakes from the Cascadia subduction zone, *Science, 295,* 2423, 2002.

Murray, J. R., Segall, P., Cervelli, P., Prescott, W., and J. Svarc, Inversion of GPS data for spatially variable slip-rate on the San Andreas fault near Parkfield, California, *Geophys. Res. Lett., 28,* 359-362, 2001.

Nadeau, R. M., Foxall W., and T. V. McEvilly, Clustering and periodic recurrence of microearthquakes on the San Andreas fault at Parkfield, California, *Science, 267,* 503-507, 1995.

Nadeau, R. M., and L. R. Johnson, Seismological studies at Parkfield VI: Moment release rates and estimates of source parameters for small repeating earthquakes., *Bull. Seism. Soc. Am., 88,* 790-814, 1998.

Nadeau, R. M., and T. V. McEvilly, Fault slip rates at depth from recurrence intervals of repeating microearthquakes, *Science, 285,* 718-721, 1999.

Okada, Y., Surface deformation due to shear and tensile faults in a half-space, *Bull. Seism. Soc. Am., 75,* 1135-1154, 1985.

Oppenheimer, D. H., Wong, I. G., and F. W. Klein, The seismicity of the Hayward fault, California, *in* Borchardt et al., eds., Proceedings of the second conference on earthquake hazards in the eastern San Francisco Bay Area, Calif. Depart. Of Conserv., Div. Of Mines and Geology Special Bull., 113, 91-100, 1992.

Ponce, D. A., Hildenbrand, T. G., and R. C. Jachens, Gravity and Magnetic expression of the San Leandro gabbro with implications for the geometry and evolution of the Hayward fault zone, northern California, *Bull. Seism. Soc. Am.,* , in press, 2003.

Rubin, A. M., Aftershocks of microearthquakes as probes of the mechanics of rupture, *J. Geophys. Res., 107(7),* 10.1029/2001JB000496, 2002.

Rubin, A. M., Gillard, D., and J.-L. Got, Streaks of microearthquakes along creeping faults, *Nature, 400,* 635-641, 1999.

Rivera, L., and H. Kanamori, Spatial heterogeneity of tectonic stress and friction in the crust, *Geophys. Res. Lett., 29(6),* 10.1029/2001GL013803, 2002.

Sammis, C. G., and Rice, J. R., Repeating earthquakes as low-stress-drop events at a border between locked and creeping fault patches, *Bull. Seism. Soc. Am., 91,* 532-537, 2001.

Savage, J. C., and M. Lisowski, Inferred depth of creep on the Hayward fault, central California, *J. Geophys. Res., 98,* 787-793, 1993.

Simpson, R. W., Lienkaemper, J. J., and J. S. Galehouse, Variations in creep rate along the Hayward Fault, California, interpreted as changes in depth of creep, *Geophys. Res. Lett., 28,* 2269-2272, 2001.

Smith, S. W., and M. Wyss, Displacement on the San Andreas fault subsequent to the 1966 Parkfield earthquake, *Bull. Seism. Soc. Am., 58,* 1955-1973, 1968.

Stark, P. B., and R. L. Parker, Bounded variable least squares: an algorithm and applications, *J. Comp. Stat., 10,* 129-141, 1995.

Thomas, A. L., POLY3D: A three-dimensional, polygonal element, displacement discontinuity boundary element computer program with applications to fractures, faults, and cavities in the earth's crust, Masters Thesis, Stanford University, 62 pp., 1993.

Toppozada, T. R., and G. Borchardt, Re-evaluation of the 1836 'Hayward Fault' earthquake and the 1838 San Andreas Fault earthquake, *Bull. Seism. Soc. Am., 88,* 140-159, 1998.

Toppozada, T. R., Real, C. R., and D. L. Parke, Preparation of isoseismal maps and summaries of reported effects for pre-1900 California earthquakes, Calif. Div. of Mines and Geol., *open file report 81-11 SAC,* 182 pp., 1981.

Waldhauser, F., Ellsworth, W. L., and A. Cole, Slip-parallel seismic lineations on the northern Hayward fault, California, *Geophys. Res. Lett., 26,* 3525-3528, 1999.

Waldhauser, F., and W. L. Ellsworth, Fault structure and mechanics of the Hayward fault, California, from double-difference earthquake locations, *J. Geophys. Res.*, *107*, 10.1029/2000JB000084, 2002.

Williams, P. L., Features and dimensions of the Hayward fault zone in the Strawberry and Blackberry creek area, Berkeley, California, *Lawrence Berk. Lab Pub. 36852*, 1995.

Working Group on California Earthquake Probabilities, Earthquake probabilities in the San Francisco Bay region: 2000 to 2030–A summary of findings, *U.S. Geol. Surv. Open File Rep., 99-517*, 1999.

Wright, T. L., and N. Smith, Right step from the Hayward fault to the Rodgers Creek fault beneath San Pablo bay, *in* Borchardt et al., eds., Proceedings of the second conference on earthquake hazards in the eastern San Francisco Bay Area, Calif. Depart. Of Conserv., Div. Of Mines and Geology Special Bull., 113, 407-417, 1992.

Wyss, M., Locked and creeping patches along the Hayward fault, California, *Geophys. Res. Lett., 28*, 3537-3540, 2001.

Yu, E., and P. Segall, Slip in the 1868 Hayward earthquake from the analysis of historical triangulation data, *J. Geophys. Res., 101*, 16101-16118, 1996.

Chapter 4

Finite Fault Inversion of the 1989 Loma Prieta Earthquake Incorporating Complex Fault Geometry

4.1 Introduction

At the time of the 1989 Loma Prieta earthquake (**M** 6.9), no previous event had provided such a complete data set to study the source kinematics of large events. This distinction was quickly eclipsed by the 1992 Landers, the 1994 Northridge, and the 1999 Hector Mine earthquakes. Although these more recent events provided superior data sets, Loma Prieta remains one of the most complex events recorded by modern strong motion instrumentation within the San Andreas fault system. Extensive research has been performed over the past decade in an attempt to resolve the seismic history of the event and understand its impact on the seismic hazard for the region [*Hanks and Krawinkler*, 1991; *Spudich*, 1996].

4.1.1 Characterization of the Source Region

The epicentral region of the Loma Prieta earthquake is located along a left-stepping, restraining jog on the San Andreas fault (Figure 4.1). Uplift of the Santa Cruz mountains is distributed along a series of southwest-dipping, reverse faults that strike sub-parallel to the San Andreas fault [*Aydin and Page*, 1984]. Right-lateral slip has juxta-posed two distinctly different geologic units. The Salinian block, composed of marine sed-iments overlying granitic plutons, is located on the west side of the San Andreas fault while graywacke and greenstone of the Franciscan formation is found on the east side. The contrast in geology has been resolved in several tomographic studies using aftershock data [*Eberhart-Philips and Michael*, 1998; *Foxall et al.*, 1993]. A sharp lateral contrast in P velocity is observed across the fault for depths above ∼5 km and a high-velocity body is resolved in the vicinity of the mainshock at depth.

Aftershocks delineate a dipping structure which stretches 45-60 km along the strike of the San Andreas fault (N51^{o}W) and extends to a depth of 18 km. *Dietz and Ellsworth* [1997] interpret many of the aftershocks to occur on neighboring structures as well as in the weakened crust surrounding the rupture surface. The northern section of the aftershock distribution outlines a 65° southwesterly dipping plane that intersects a sub-vertical San Andreas fault at a depth of ∼8 km. A diffuse zone of aftershocks cluster to the east of the fault at shallower depths. The dip of the aftershock distribution led several researchers to conclude that the rupture did not actually occur on the San Andreas fault, but rather on a reverse structure named the Loma Prieta fault. Moving south, the aftershock dis-tribution gradually transitions to a sub-planar structure that rotates to a vertical profile
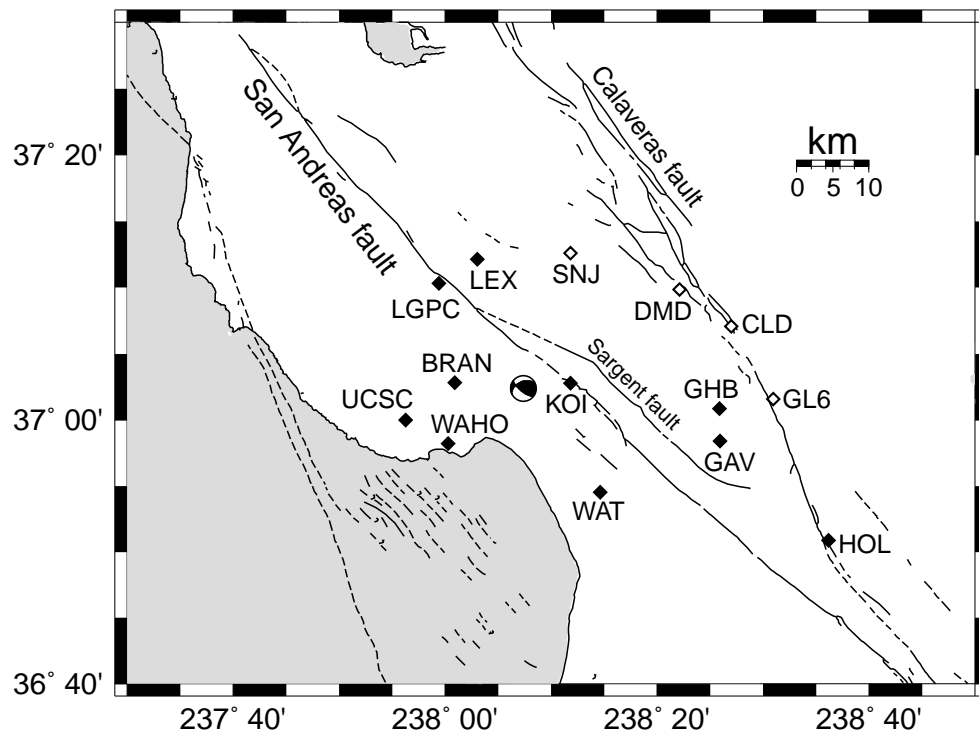
Figure 4.1: Map of the epicentral region showing the locations of strong motion stations with absolute time information. Stations with closed diamonds are used in the inversion analysis. Stations with open diamonds are excluded due to concerns over 3D path effects. Solid and dotted lines denote the regional faults. The focal mechanism for the mainshock marks the epicenter.

as it eventually meets up with the creeping section of the central San Andreas fault. The focal mechanisms for the aftershocks were found to be diverse, consisting of strike-slip, normal, reverse, and oblique events. *Beroza and Zoback* [1993] found the diversity to be inconsistent with the static stress change imposed by the mainshock. While the exact cause remains unclear, the diversity does suggest that the post-earthquake stress field was highly heterogeneous [*Michael et al.*, 1990].

4.1.2 Systematic Biases to Source Inversions

The lateral heterogeneity of the velocity structure, the diffuse distribution of aftershocks, the inability to explain the aftershock distributions from coseismic static stress changes, and an inferred heterogeneous stress field suggest that the Loma Prieta mainshock was complex. The potential for a systematic bias may be significant when performing a kinematic inversion. Despite the complexity, several inversions for kinematic slip history found similar results [*Beroza*, 1991; *Horton et al.*, 1997; *Steidl et al.*, 1991; *Wald et al.*, 1991]. All of the investigators found evidence for a bilateral rupture with two distinct patches of slip. The northwest patch produced ∼4 m of oblique motion (reverse and strike-slip) while the southeast patch released ∼5 m of predominately strike-slip motion. Very little slip was observed either at the hypocenter or up-dip of the hypocenter, and no offset was observed at the surface. Most studies assumed a single rupture plane when performing an inversion for the slip history. This assumption was taken to simplify the inversion and improve resolution. The rupture models differ in the magnitude of slip assigned to the two primary asperities and in the variable rake across the fault plane. While these discrepancies may reflect differences in inversion methodologies, it might also reflect a systematic bias

that forces unresolved slip to be mapped onto the predefined fault plane.

A systematic bias could result from a host of modeling assumptions or data limitations. The effects of using a one-dimensional velocity model to represent the three dimensional structure in the region has already been evaluated by *Cormier and Su* [1994]. They found that complex velocity structure can account for the variability between published rupture models. Lateral structure which focuses and defocuses seismic energy was found to be a potential bias while multipathing effects or caustics did not appear to be a significant concern. Station geometry may also impose a bias in resolving slip on different sections of the rupture plane. Additionally, the presence of inelastic deformation, either from the response of weakened crust or poroelastic effects, may also bias the results. Finally, a complex fault geometry, one where rupture occurs on multiple planes of different orientation, could also impose a significant bias. Several researchers investigated the effects of non-planar structures when resolving the Loma Prieta slip distribution using geodetic data [*Du and Aydin*, 1996; *Marshall et al.*, 1991; *Snay et al.*, 1991]. Generally, they found a modest or insignificant improvement in fit to the data compared to planar models. Beyond these studies of the coseismic displacement field using geodetic data, the effect of complex rupture geometry on the kinematic slip history has not been explored.

4.1.3 Fault Geometry

For most waveform inversion studies, the location of the rupture plane is determined either from the distribution of aftershocks, or the inversion of geodetic data which are more sensitive to static slip geometry. All of the waveform inversions for Loma Prieta that used waveform data assumed a 70° southeast dipping plane. Inversions of geodetic

data provided constraints on the location of the rupture plane and the magnitude of slip which agreed qualitatively with the waveform inversion, although these studies also limited their analysis to a single rupture plane [*Arnadottir and Segall*, 1994; *Marshall et al.*, 1991].

Given the diffuse aftershock distribution and the known geologic structure of the region, additional fault geometries have been proposed [*McLaughlin et al.*, 1999]. The partitioning of slip on a dipping Loma Prieta fault and a vertical San Andreas fault was first suggested by *Dietz and Ellsworth* [1990]. *Schwartz et al.* [1990] discuss how slip on a shallow thrust, in addition to slip on the San Andreas or the Loma Prieta fault, would better explain the present day topography. From the analysis of postseismic surface displacement data, *Bürgmann et al.* [1997] found that afterslip occurred on a shallow thrust fault located to the northeast and up-dip of the main rupture. This low angle thrust may correlate with the Berrocal fault or any of the other thrusts located along the foothill range front. It was never explored whether coseismic slip on this shallow thrust, or more complicated geometries, may be resolved by the available waveform data. If the rupture occurred on multiple planes, this would produce a significant, systematic bias in all published models of the source history. I evaluate how the slip distribution changes with increasingly complex fault geometries and determine whether these geometries provide a significant improvement in fit to both waveform and geodetic data.

4.2 Inversion Methodology

A finite source inversion for the kinematic slip distribution of the Loma Prieta earthquake is performed using the approach described in *Kaverina et al.* [2002] and *Dreger*

and Kaverina [2000]. The inversion solves for the strike-slip and dip-slip components on a discretized fault plane. Multiple rupture planes can be parameterized in the inversion and both waveform and geodetic data are inverted jointly. Positivity is enforced through a non-negative least squares routine [*Lawson and Hanson*, 1974]. Rupture is delayed on each subfault in accordance with a circular rupture front that propagates from the hypocenter. To allow for variable rupture velocity and dislocation rise time, slip on each subfault is convolved with an isosceles triangle of 0.7 seconds in duration for 5 overlapping time windows, each delayed by 0.35 seconds. Green's functions for each subfault-receiver pair are then summed to produce the synthetic at each station. Figure 4.2 shows how a constant rupture velocity and the dislocation rise time are constrained by the waveform data. Moment minimization and Laplacian smoothing constraints are included to help improve the model resolution and to provide stability.

Coseismic surface displacements at 32 stations are incorporated from Global Positioning System (GPS) data of *Lisowski et al.* [1990] and *Williams et al.* [1993], electro-optical distancing measurements from *Lisowski et al.* [1990], very long baseline interferometry data from *Clark et al.* [1990], and 219 leveling data described in *Marshall et al.* [1991]. Waveform data are restricted to corrected velocity records collected with absolute time at 22 stations maintained by the California Department of Mines and Geology (CDMG) and the University of California, Santa Cruz (UCSC) (Table 4.1). Absolute time for the UCSC stations was determined by McNally *et al.* [1996]. Stations in San Jose (USGS), Gilroy Array 6 (CDMG), Anderson Dam (USGS), and Coyote Lake Dam (CDMG) are excluded since *Cormier and Su* [1994] found these stations to be most susceptible to multipathing
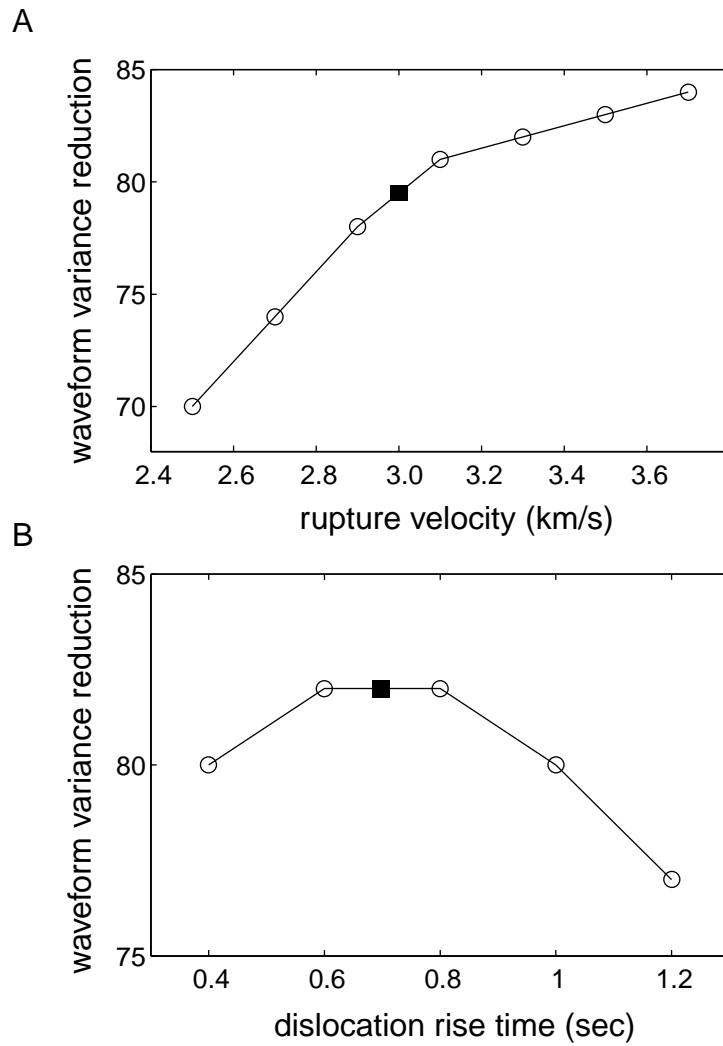
A

B

Figure 4.2: The inversion of the waveform data provides a good constraint on the (B) dislocation rise time, but does not limit (A) the velocity of the propagating rupture front. Values of 0.7 seconds for the dislocation rise time and 3 km/sec for the rupture velocity on the Loma Prieta fault are used in the inversion (solid squares).

and other path effects. Waveform data are filtered using a two-pass butterworth filter with corners at 0.1 and 1 Hz, and sampled at 0.1 sec.

Station delays are not employed when performing the combined inversion. *Wald et al.* [1991] discuss how station delays are crucial when accounting for lateral heterogeneity not modeled by a one-dimensional velocity model. However, waveform data are adequately modeled without applying arbitrary station delays. While incorporating the 3D velocity structure remains a long term goal for inversion studies, a 1D velocity model is employed for several reasons. *Cormier and Su* [1994] investigated the benefits of incorporating 3D velocity structure in waveform modeling for Loma Prieta. While amplitudes and local site responses are best modeled by 3D models, phase arrivals are reasonably modeled by 1D velocity structure. *Graves and Wald* [2001] perform synthetic inversions to evaluate the resolving power of Green's functions calculated from a 3D velocity model. They found that well-calibrated 3D models provide superior resolving power while hybrid 1D velocity models and inexact 3D crustal models can only partially resolve the slip distribution. Existing 3D models of the San Francisco Bay Area are still in the development stages and uncertainties in the lateral velocity structure at depth can produce significant biases in synthetic waveforms. The validation of existing 3D models of the San Francisco Bay Area using teleseismic and weak motion data suggest that modifications to the models are still necessary [*Dreger et al.*, 2001]. Given the existing options, a 1D model is least likely to impose an unknown bias into the inversion. Additionally, the calculation of waveforms using 3D models continues to be computationally expensive.

Green's functions are calculated for 3 distinct one-dimensional velocity models to

evaluate whether the choice in velocity structure significantly impacts the slip distribution. Several velocity models were tested, including models from *Beroza* [1991], *Wald et al.* [1991], and *Steidl et al.*[1991]. *Beroza* [1991] used two distinct velocity models, one for stations to the northeast of the San Andreas fault and one for stations to the southwest. This composite set was used to simulate the difference in velocity structure on opposite sides of the San Andreas fault. I attempted to examine how the velocity models were able to model the aftershock data. However most stations that observed the mainshock were not functional for the larger aftershocks. Additionally, few, if any, of the aftershocks duplicated the mainshock focal mechanism in the hypocentral region making it difficult to asses the velocity models or solve for station delays using a small subset of the aftershock data. After performing mainshock inversions using the three different velocity models, a significant difference between slip distributions was not found. Given our choice of inversion parameters, the velocity model from *Wald et al.* [1991] produced the best fit to the data. Waveform Green's functions are calculated using the model of *Wald et al.* [1991] (Table 4.2)using a frequency-wavenumber algorithm (written by Chandan Saikia of URS). Only the first 10-20 sec of the east and north components are used in the inversion. Several investigators have demonstrated that the initial rupture from the hypocenter was slow. Therefore, Green's functions are delayed by 1.8 seconds in accordance with previous estimates [see *Wald et al.*, 1991; *Deitz and Ellsworth*, 1997]. Displacement Green's functions are calculated for a dislocation in an elastic half-space using the formulation of *Okada et al.* [1985].

Table 4.1: Strong motion stations with absolute time used in the inversion.

Station	Location	Owner	Seconds used
KOI	Corralitos	CDMG	14
GAV	Gavilan College	CDMG	12
GHB	Gavilan Historical Building	CDMG	12
GI1	Gilroy Array #1	CDMG	15
HOL	Hollister	CDMG	12
WAT	Watsonville	CDMG	14
LEX	Lexington Dam	CDMG	10
LGPC	Los Gatos	UCSC	15
BRAN	Branciforte	UCSC	20
UCSC	UC Santa Cruz	UCSC	16
WHAO	Walter's House	UCSC	16

Table 4.2: The velocity model from *Wald et al.* [1991].

V_p	V_s	density	thickness	depth
1.73 km/s	1.00 km/s	1.50 g/cm^3	0.1 km	0.1 km
3.38	1.95	1.55	0.4	0.5
4.29	2.48	1.85	0.5	1.0
4.80	2.77	2.05	2.0	3.0
5.37	3.10	2.26	2.0	5.0
5.74	3.31	2.45	2.0	7.0
6.15	3.55	2.58	2.0	9.0
6.25	3.61	2.62	4.0	13.0
6.27	3.62	2.63	5.0	18.0
6.67	3.85	2.77	7.0	25.0
8.00	4.62	3.28	50.0	75.0

4.3   Fault Plane Resolution

Before presenting the inversion results for the 1989 event, a series of synthetic inversions are performed to assess our ability to resolve a known slip distribution given the data and station distribution for Loma Prieta. None of the forward or inverse models discussed in this section incorporate variable rupture velocity nor random noise. Therefore, these results illustrate the best-case scenario given the available data constraints. Four fault geometries are evaluated (Figure 4.6a-d): 1) a single 70°, southerwesterly-dipping plane (referred to as model LP), 2) a vertical San Andreas fault where a quarter of the fault plane dips 65° to the southwest below 10 km (model VERT-SAF), 3) a vertical San Andreas fault above 10 km and a 65° dipping fault below (model LP-SAF), and 4) model LP-SAF with a 30° dipping, shallow thrust located to the east of the San Andreas fault that intersects the vertical fault plane at a depth of 5 km (model THRUST). All models are parameterized with a northwestern patch of purely dip-slip motion and a southeastern patch of purely strike-slip. Model THRUST includes an upper patch of purely dip-slip. The geometry for all fault planes is listed in Table 4.3. The primary fault planes generally extend 40 km along strike and 20 km down dip within the depth range of 1.90 to 20.77 km.

From these model geometries, waveform and geodetic data are predicted using the station distribution for the Loma Prieta earthquake. All forward models begin with the same moment magnitude. To asses the resolution afforded by the station geometry, the synthetic data are then inverted using the identical fault plane geometry (middle plot in Figures 4.6b-d). The inversions include Laplacian smoothing, which explains why the slip distributions are not identically resolved. Results suggest that the data are able to resolve

Table 4.3: Fault plane geometries parameterized in the inversion.

Description	strike	dip	width	length	Latitude[a]	longitude[a]	depth[a]	V_r
after *Wald et al.* [1991]	129°	70°	20 km	40 km	37.07^o	-121.85^o	1.9 km	3.0 km/s
after *Arnadottir and Segall* [1994]	132	76	20	40	37.06	-121.86	-	
Loma Prieta fault	129	65	10	40	37.05	-121.87	10.3	3.0
San Andreas fault	129	90	10	40	37.05	-121.87	0.3	2.7
shallow thrust	129	30	10	40	37.10	-121.81	0.3	2.5

[a]The top-center coordinate for each fault plane. Hypocenter location 37.034^o, -121.885^o, 16 km depth, 00:04:15.2 UTC.

Model Input

Inversion Result

slip (m)
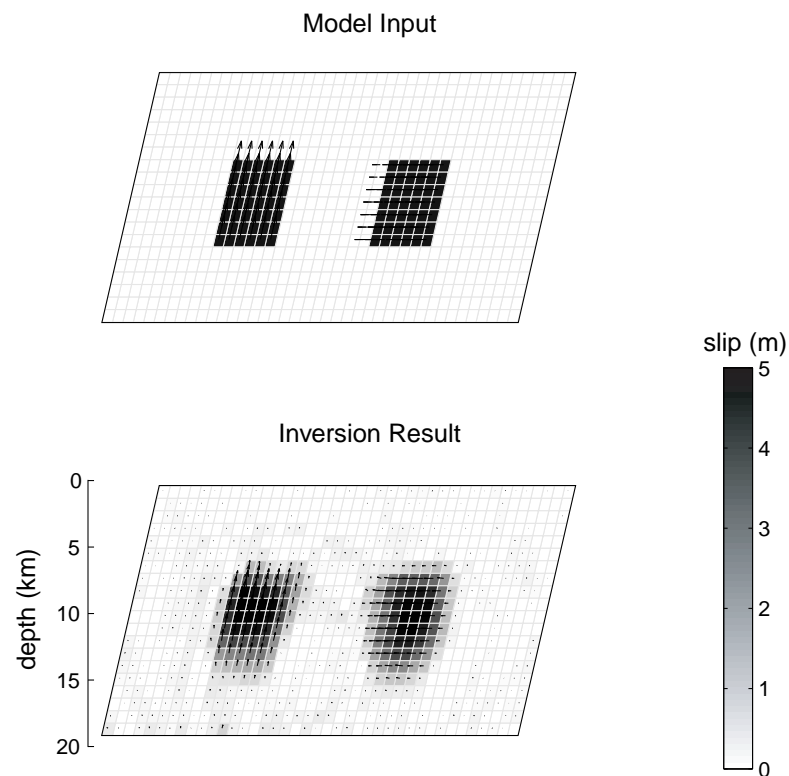
Figure 4.3: Station resolution and the mapping of complex rupture onto a single plane are assessed through a series of synthetic inversions. Four rupture geometries are analyzed (see text for a detailed description). (A) Synthetic waveform and geodetic data are produced for the parameterized slip distribution using model **LP** (top). Synthetic data are inverted for a 70° dipping plane, similar to the fault plane used in previously published inversion studies for Loma Prieta (bottom).

Figure 4.4: (B) Synthetic waveform and geodetic data are produced for the parameterized slip distribution (top plot) using model **VERT-SAF**. The inversion result is shown using the synthetic data to assess the resolution of the inversion given the station geometry (middle plot). Synthetic data are inverted for a 70° dipping plane, similar to the fault plane used in previously published inversion studies for Loma Prieta (bottom plot). This illustrates how slip on multiple rupture surfaces is mapped onto a single plane.

Model Input

slip (m)

Inversion Result
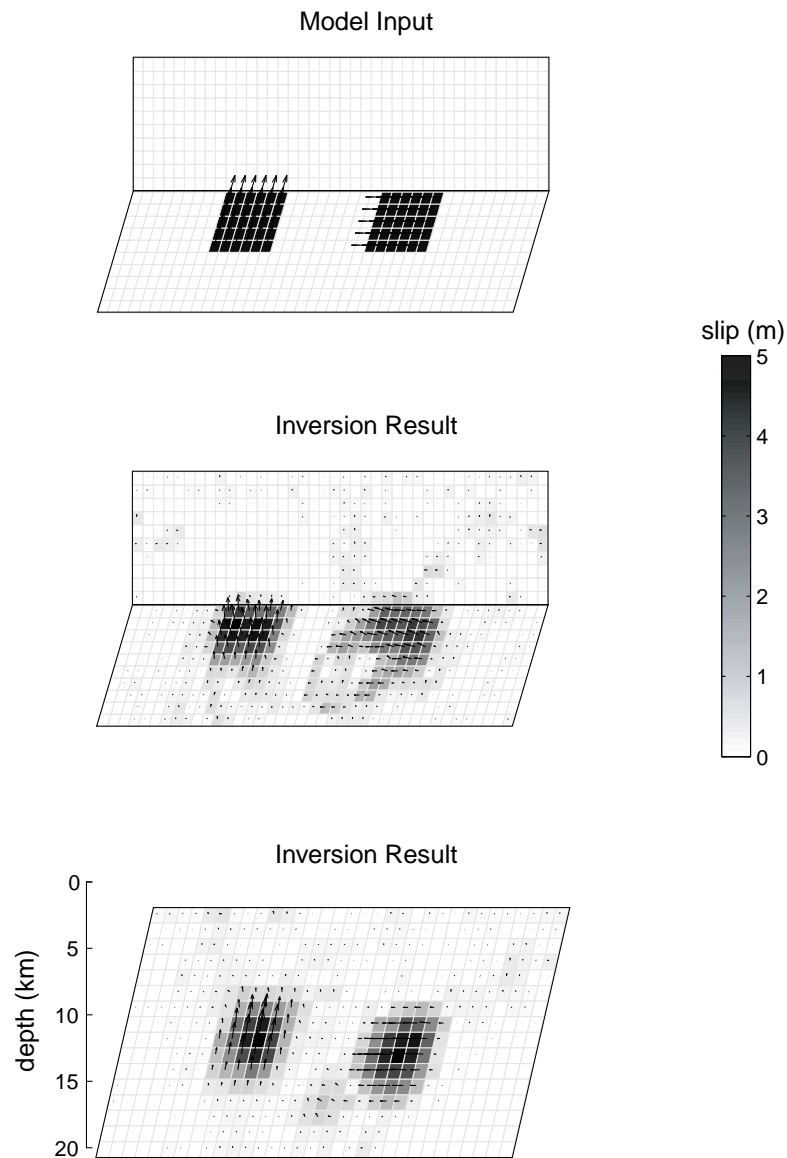
Inversion Result

Figure 4.5: (B) Synthetic waveform and geodetic data are produced for the parameterized slip distribution (top plot) using model **LPSAF**. The inversion result is shown using the synthetic data to assess the resolution of the inversion given the station geometry (middle plot). Synthetic data are inverted for a 70° dipping plane, similar to the fault plane used in previ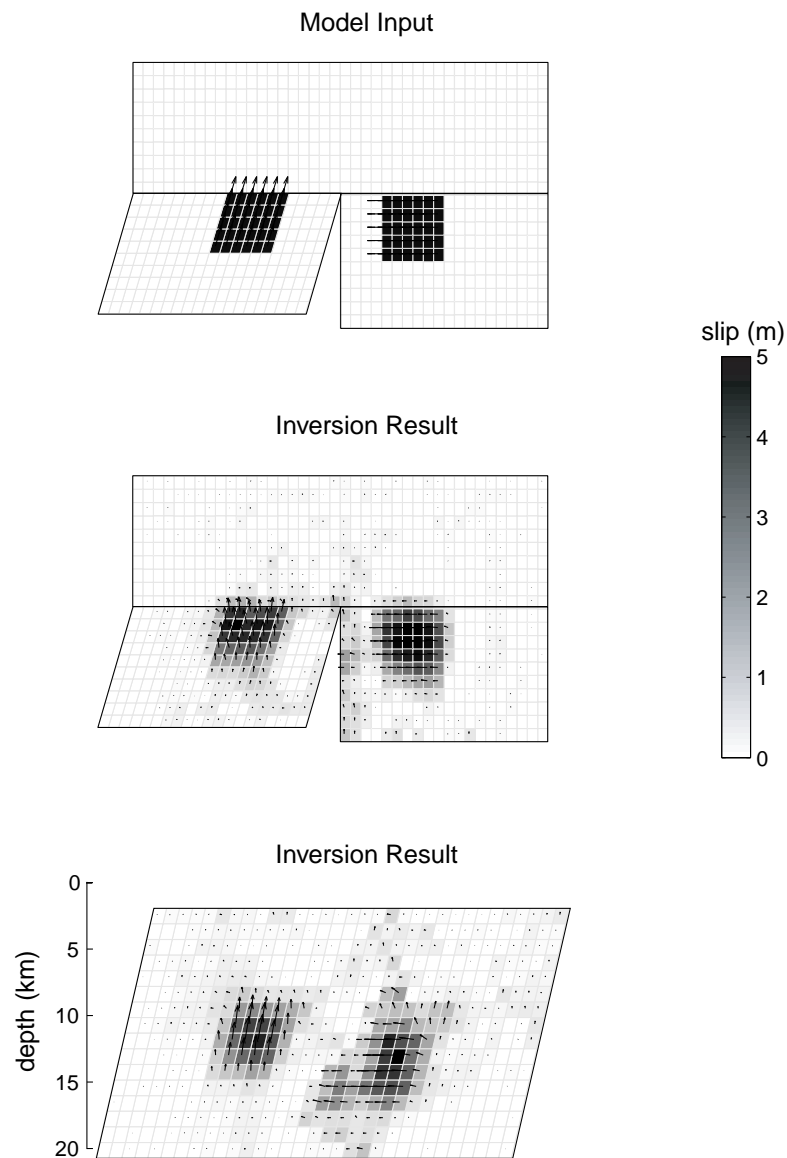ously published inversion studies for Loma Prieta (bottom plot). This illustrates how slip on multiple rupture surfaces is mapped onto a single plane.

Figure 4.6: (D) Synthetic waveform and geodetic data are produced for the parameterized slip distribution (top plot) using model **THRUST**. The inversion result is shown using the synthetic data to assess the resolution of the inversion given the station geometry (middle plot). Synthetic data are inverted for a 70° dipping plane, similar to the fault plane used in previously published inversion studies for Loma Prieta (bottom plot). This illustrates how slip on multiple rupture surfaces is mapped onto a single plane.
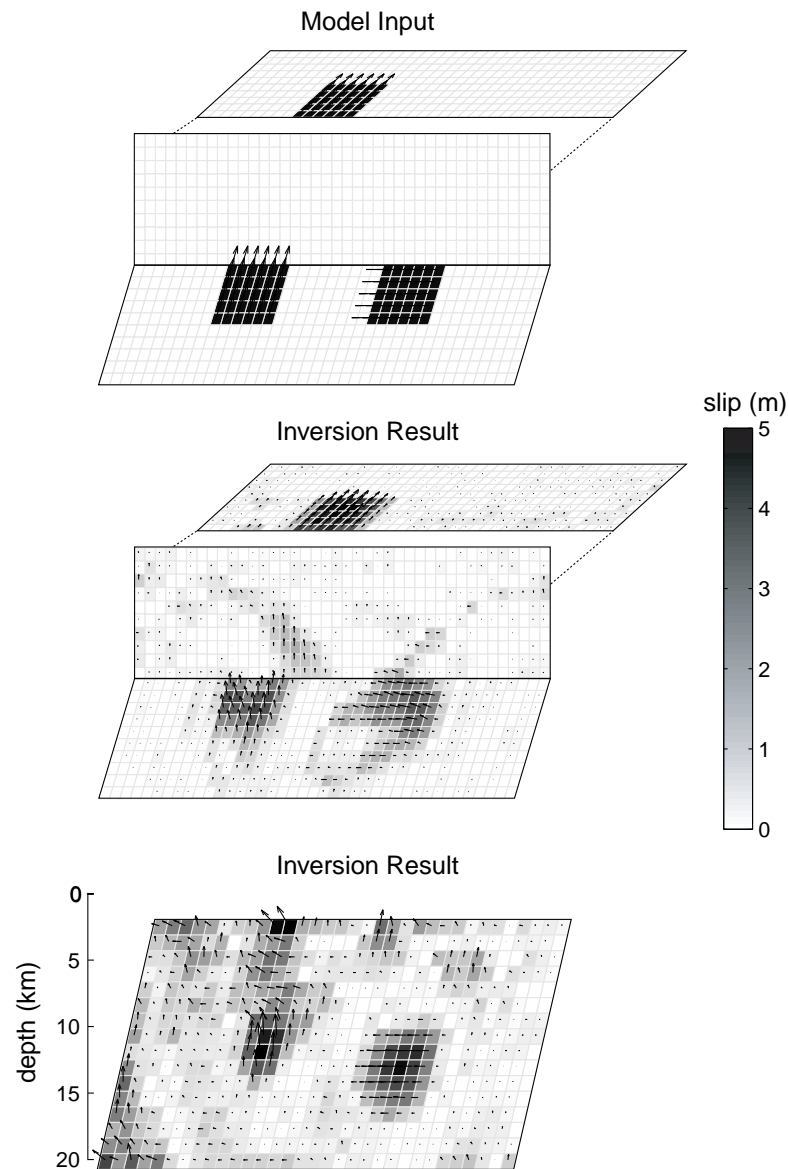
the primary features of the designed slip distributions. Strike-slip motion on a dipping surface tends to become more distributed as observed in the middle plots of Figure 4.6c-d. For model THRUST (Figure 4.6d), the inversion prefers to map reverse slip from the Loma Prieta fault to the shallow thrust plane.

A second set of inversions are performed using a single, 70° dipping plane (bottom plot in Figures 4.6a-d). This is done to visualize how slip on multi-oriented rupture surfaces may map onto a single plane. Generally, the strike-slip patch is resolved over a larger area than the dip-slip patch. Some strike-slip motion is mapped into the northwest patch producing oblique slip along the edge of the asperity. The rake on the dip-slip patch contains a small component of strike-slip motion. For Model THRUST, slip on the shallow thrust is mapped to the top half and along the northwest edge of the single fault plane. This illustrates how slip occurring on adjacent structures can lead to an inversion result with significant slip distributed across the fault plane.

4.4 Inversion Results

Waveform and geodetic inversions are first performed independently to assess how they agree with previously published results. For the waveform comparison I use the station delays and fault geometry as specified in *Wald et al.* [1991] except that I use a square subfault dimension of 1.25 km (Table 4.3). The slip history for a 70° dipping plane agrees with the bilateral distribution found by *Wald et al.*[1991] (Figure 4.7). A peak slip amplitude of 4.6 m is found for both the northwest and southeast slip patch.

For the inversion of the geodetic data, subfault dimensions are identical to the

waveform inversion except that I use a dip of 76° and a fault plane location as determined by *Arnadottir and Segall* [1994]. Slip is confined to the upper 10 km of the defined fault plane and is localized to at least two fault patches (Figure 4.8a). The distribution agrees well with that found by *Arnadottir and Segall* [1994] despite the fact that data covariances are not included in the inversion. Residuals for the leveling data are consistent with those found by *Marshall et al.* [1991] (Figure 4c). GPS stations south of the epicenter and near the San Andreas fault have the greatest discrepancies in orientation (Figure 4.8b). *Dietz and Ellsworth* [1997] found that moment tensor solutions and relocations were significantly biased by lateral heterogeneity along the southernmost portion of the aftershock distribution. Therefore, the misfit in the GPS data for stations south of the epicenter might reflect significant material heterogeneity in the top few kilometers of the crust.

The use of an elastic half-space is expected to bias the inversion by under-predicting the surface displacements [*Hearn and Bürgmann*, unpublished manuscript; *Wald and Graves*, 2001]. The inversion will either require higher slip magnitudes at deeper depths or lower slip magnitudes at a shallower depth. Given that the displacement Green's functions do not incorporate crustal heterogeneity, the inversion is only expect to partially recover the actual slip distribution. However, *Wald and Graves* [2001] have demonstrated that a combined inversion of both waveform and geodetic data significantly improves the resolving power of the inversion.

4.4.1 Combined Inversion

A combined waveform and geodetic inversion is performed for a single 70° dipping plane (Table 4.3). Absolute time is held fixed in the inversion except for a 1.8 second

A

Oblique Slip, This Study

B

Oblique Slip, *Wald et al.* [1991]
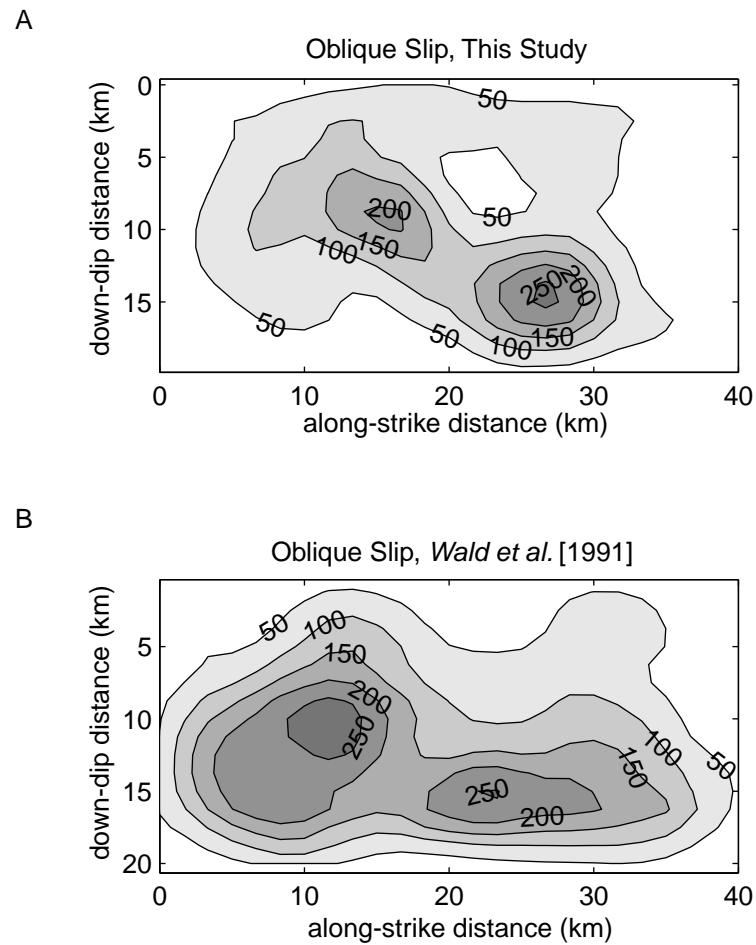
Figure 4.7: Cumulative slip is compared for (A) our inversion result for slip on a 70° dipping plane using only waveform data and (B) the slip distribution found by *Wald et al.* [1991]. Data are resampled and contoured in a consistent manner. For (A) the rupture velocity and station delays determined by *Wald et al.* [1991] are used. Contours of oblique slip are in increments of 50 cm.
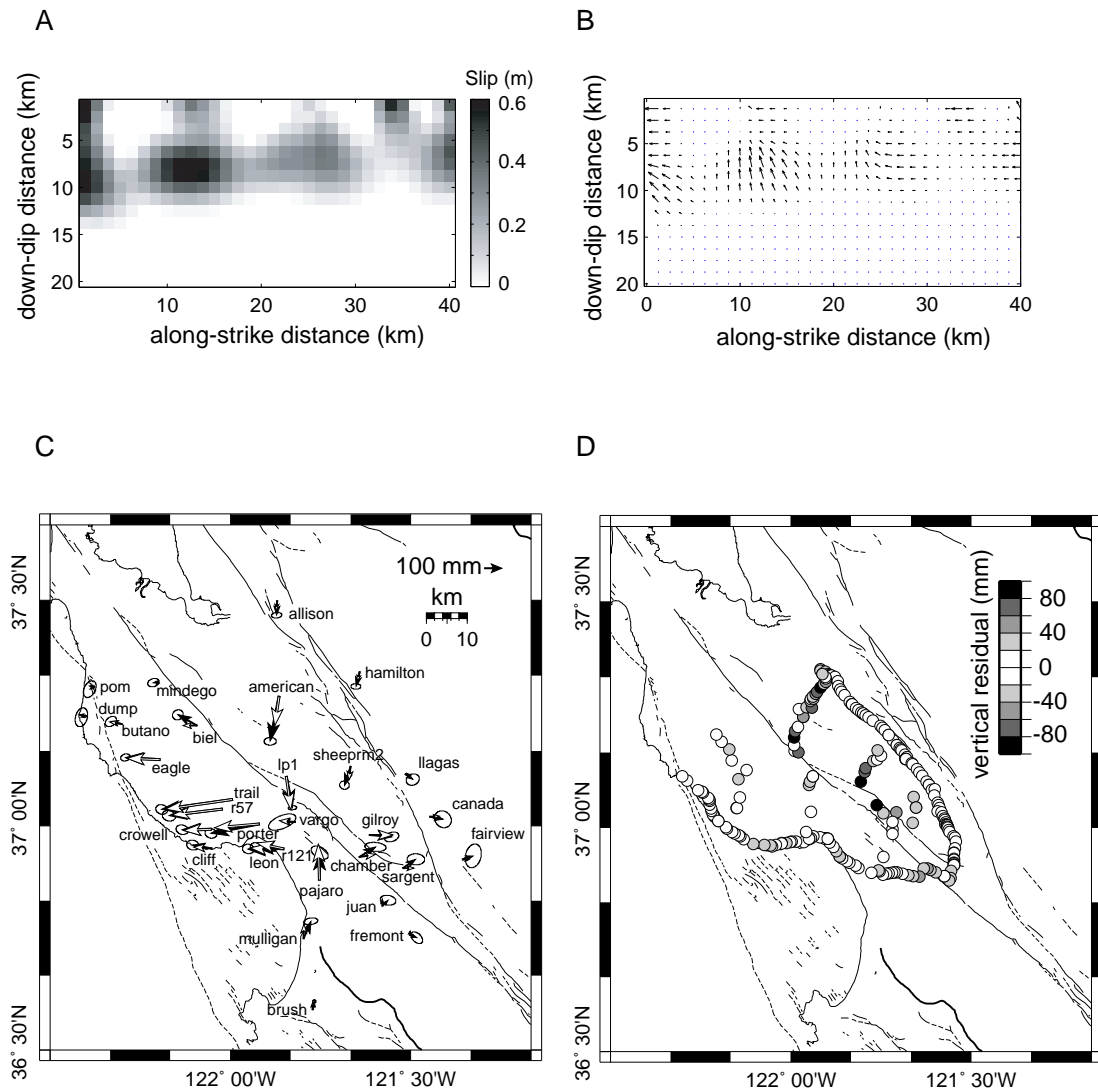
Figure 4.8: Total slip (A) and rake (B) determined for the geodetic data using the strike and dip of *Arnadottir and Segall* [1994]. (C) Significant misfits to the EDM, VLBI, and GPS data exist at the northern and southern extremes of the aftershock zone for benchmarks American, Biel, Chamber, and Sargent. (D) Misfits to the leveling data are consistent with that found by *Marshall et al.* [1991].

Table 4.4: Inversion results for various runs.

Run[a]	Description	Total Moment (dyne cm)	Variance Reduction			RSS (m^2 x 10^{-3})			L2 Norm
			Waveform	GPS	Leveling	Waveform	GPS	Leveling	
1	waveform only	2.5e+26	77	-	-	652	-	-	285
2	geodetic only	3.3e+26	-	95	94	-	37	119	1725
3	LP	3.4e+26	68	88	93	901	90	135	423
4	LPSAF	3.5e+26	71	90	87	812	71	242	429
5	THRUST	3.6e+26	79	91	93	583	67	128	383

[a]Run 1 uses station delays of *Wald et al.* [1991] . Run 2 uses the fault plane of *Arnadottir and Segall* [1994]. Runs 3-5 use both waveform and geodetic data in a combined inversion.

delay to the start of rupture from the origin time. The waveform and geodetic data are weighted such that the fit to the geodetic data is maximized without degrading the fit to the waveform data (Figure 4.9a). Waveform, GPS, and leveling data are assigned weights of 1.0, 0.1, and 0.06, respectively thereby assigning the greatest weight to the waveform data. This is appropriate given that the geodetic data can only constrain the static slip distribution and cannot constrain the kinematics of the rupture propagation. The appropriate smoothing weight is determined from the trade-off between the model roughness and the residual sum of squares (Figure 4.9b).

The majority of slip occurs in the first time window, except for a patch of slip that is placed in the final time window which is consistent with the findings of *Wald et al.* [1991] (Figure 4.10a). This would suggest that the rupture velocity was slower for slip found in the final time window or that the inversion is unable to model some aspect of the rupture history. The discussion that follows focuses on slip that occurs in the first time window. Oblique slip in the northwest patch propagates up-dip from the hypocenter (Figure 4.10b-c). The southeast patch is predominately strike-slip which is consistent with previously published rupture models. For the combined inversion, slip is found at greater depths with a smaller slip amplitude compared to the result using only geodetic data.

In addition to the single rupture plane, the data are inverted using two additional fault geometries: model LP-SAF and model THRUST. A kinked fault plane that includes both a Loma Prieta and San Andreas fault provides a modest improvement in the variance reduction for both the waveform and GPS data although the fit to the leveling data degrades (Table 4.4, run 4, model LP-SAF). Maximum slip consolidates along the upper portion of
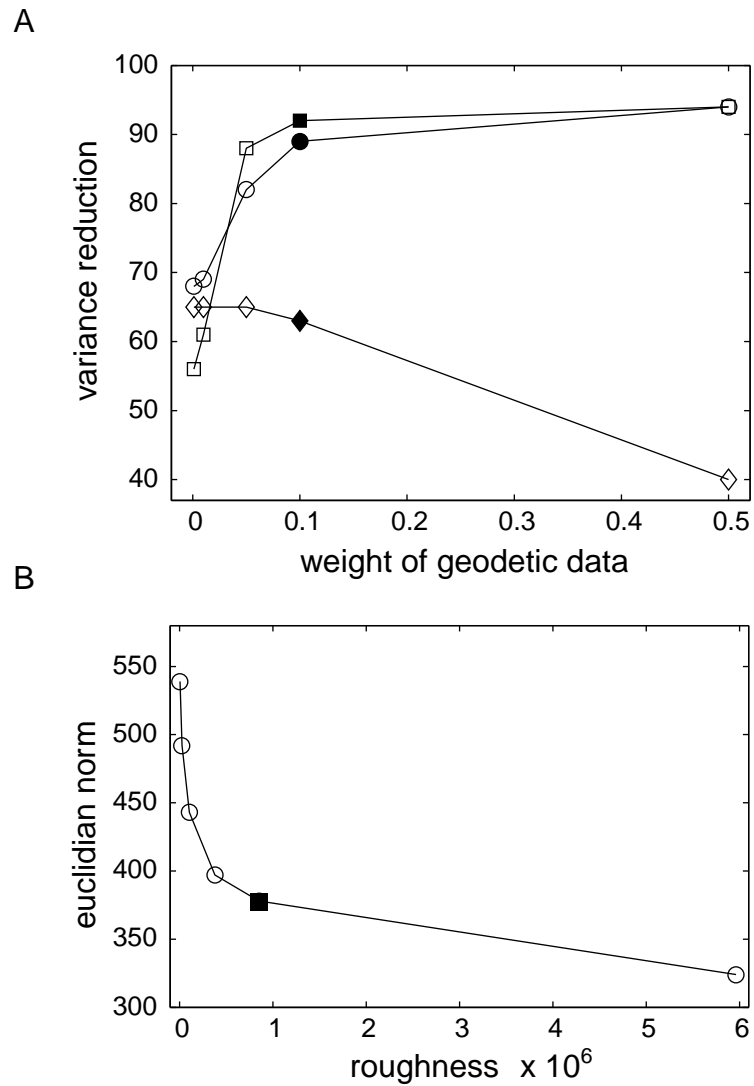
Figure 4.9: (A) Variance reduction is plotted as a function of the weight applied to the geodetic data. The fit to the waveform data (diamonds) decreases as the fits to the GPS, EDM, VLBI (squares), and leveling data (circles) increase. A geodetic weight of zero is equivalent to performing an inversion using only the waveform data. (B) The appropriate smoothing weight is determined from the tradeoff between model roughness and the L2-norm of the inversion. Open circles denote different smoothing weights. A smoothing weight of 0.0001 is used in the inversions (closed square).

A

C
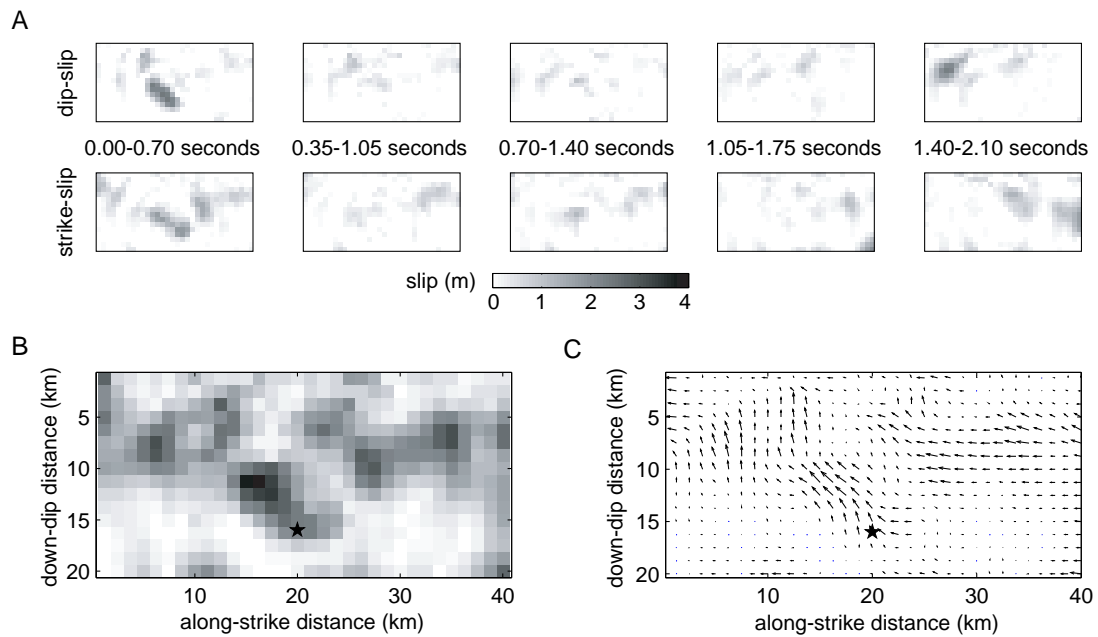
Figure 4.10: (A) Moving time windows for the combined inversion show that the majority of slip occurs in the first time window. (B) Total slip and rake for the combined inversion show slip propagating up-dip and north of the hypocenter while strike-slip motion is resolved to the south.

the Loma Prieta fault plane at a depth of 10 km, especially for the reverse slip component (Figure 4.11). Slip on a vertical San Andreas fault is not preferred by the inversion for this fault geometry. This might suggest that for strike-slip rupture to be assigned to the San Andreas fault, an appreciable dip is required.

A similar pattern of slip is maintained when a shallow thrust plane is included in the geometry (Figure 4.11c, Table 4.4, run 5, model THRUST). For the shallow thrust, a linear rupture front is parameterized in the inversion when slip first reaches the bottom edge of the thrust plane. A concentrated patch of slip is resolved on the shallow thrust plane. Slip on the thrust is spread out evenly over the 5 time windows suggesting that the rise time for this fault may last several seconds.

4.5   Discussion

Generally, the waveform data are well modeled by the inversion. Waveform data and synthetic traces are directly compared for each model geometry (Figure 4.12a-c). WAT, HOL, LGPC, and LEX have the largest peak velocities and typically exhibit the simplest waveforms. Stations UCSC and GHB have the poorest overall fits. The residuals at these stations do not improve as the model geometry changes. Stations GAV and WAT show the greatest improvement as the fault geometry is changed. Both of these stations are located south of the epicenter. The peak amplitudes at several stations are underestimated, especially for the large phase arrivals at stations LGPC, HOL, and in Gilroy. As discussed by *Cormier and Su* [1994], the large amplitude arrivals are underestimated because the Green's functions are calculated using a 1D velocity model.
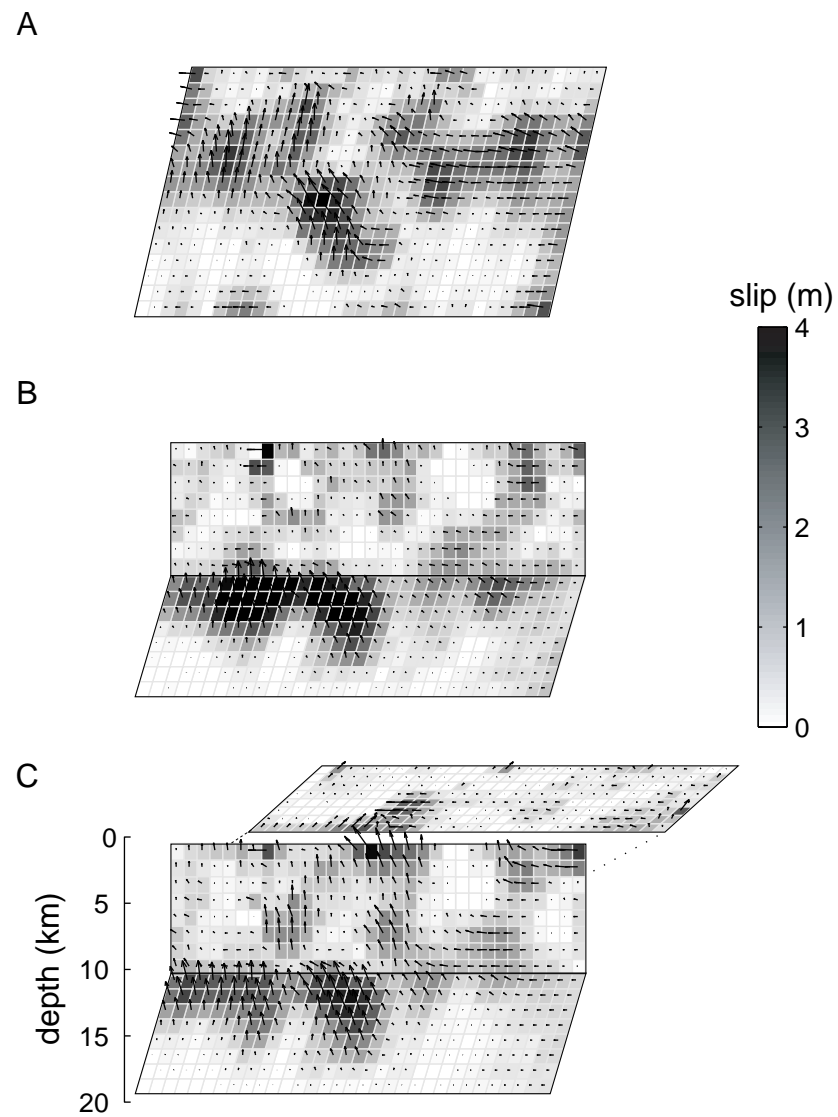
Figure 4.11: The oblique slip distributions for inversions using model LP (top plot), model LP-SAF (middle plot), and model THRUST (bottom plot). The descriptions for each run and the parameterization for each plane is summarized in Tables 4.3 and 4.4. The shallow thrust (bottom plot) is shifted away from the San Andreas fault to improve visibility. The perspective used to display the fault planes is looking towards the northeast.
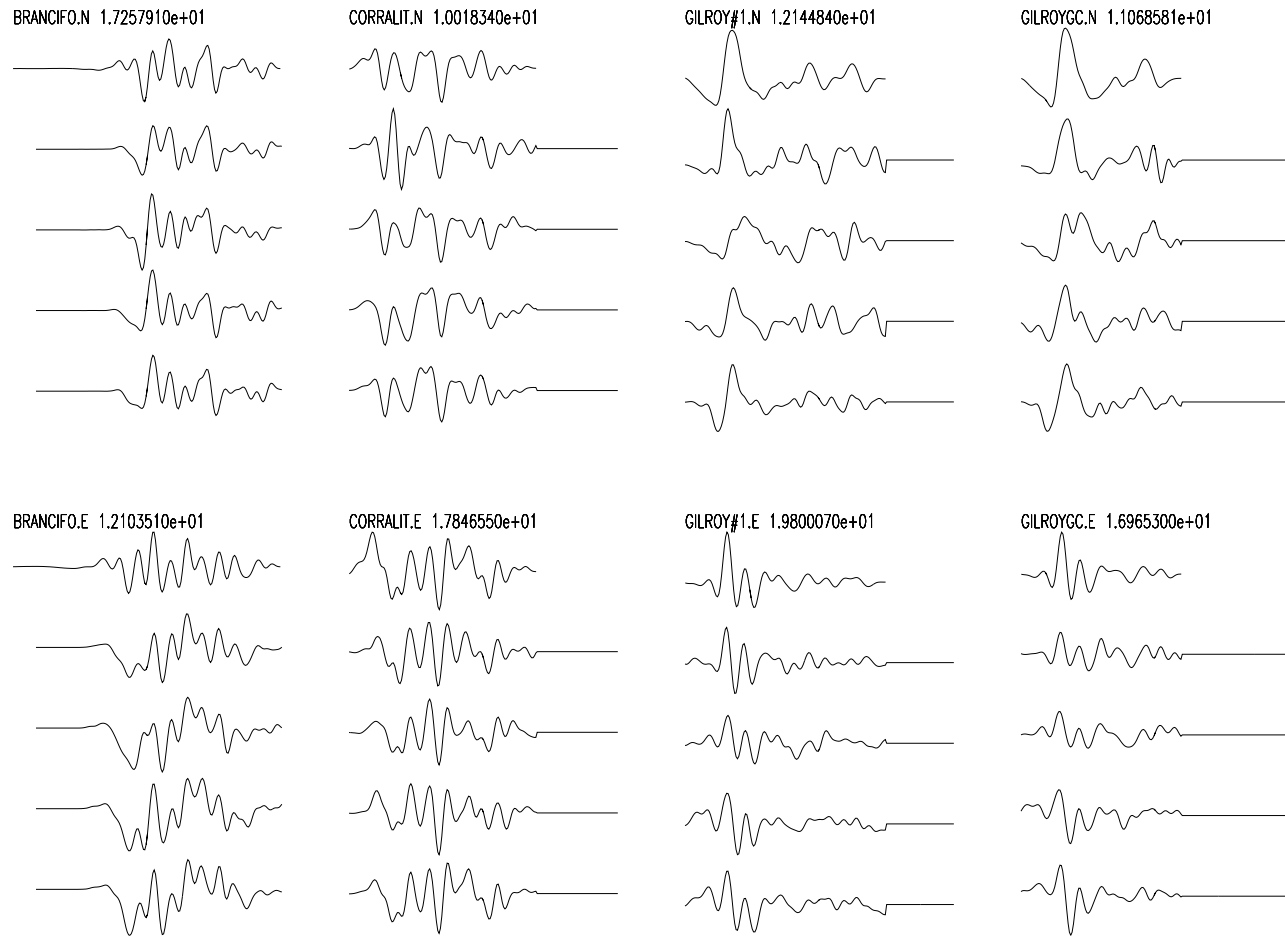
Figure 4.12: Synthetic velocity waveforms for a waveform-only inversion using model LP (second trace from top), a combined waveform and geodetic inversion using model LP (third trace from top), model LP-SAF (fourth from top), and model THRUST (bottom trace) are compared to the original data (top trace). The maximum amplitude (cm/s) of the waveform data is printed next to the station name. The top set of traces are for the north component and the bottom set are for the east component at each station.

GILROYHB.N 1.1908940e+01　　HOLLISTE.N 3.6378082e+01　　LEXINGTO.N 2.6132591e+01　　LOSGATOS.N 6.3720177e+01

GILROYHB.E 2.8565891e+01　　HOLLISTE.E 1.9904381e+01　　LEXINGTO.E 2.9996281e+01　　LOSGATOS.E 2.3362629e+01

Figure 4.12: Continued.

Figure 4.12: Continued.

A forward model is performed to identify which parts of the slip distribution for model LPSAF contributes to the energy received at various seismic stations (Figure 4.13a-c). Energy from the northwest asperity largely affects all of the UCSC stations (UCSC, WAHO, BRAN, LGPC) and station LEX. The synthetic waveform at station LEX is almost identically reproduced by the oblique motion on the northwest asperity. The predominately strike-slip motion on the southeast asperity produces the phase arrivals at the Gilroy stations (GAV, GI1, and GHB) and WAT. Given its central location, KOI receives phase arrivals from both asperities. Station HOL receives very little of its energy from either asperity.

The geodetic data show minimal change in the fit of the synthetic surface displacements given a change in the model geometry for stations gr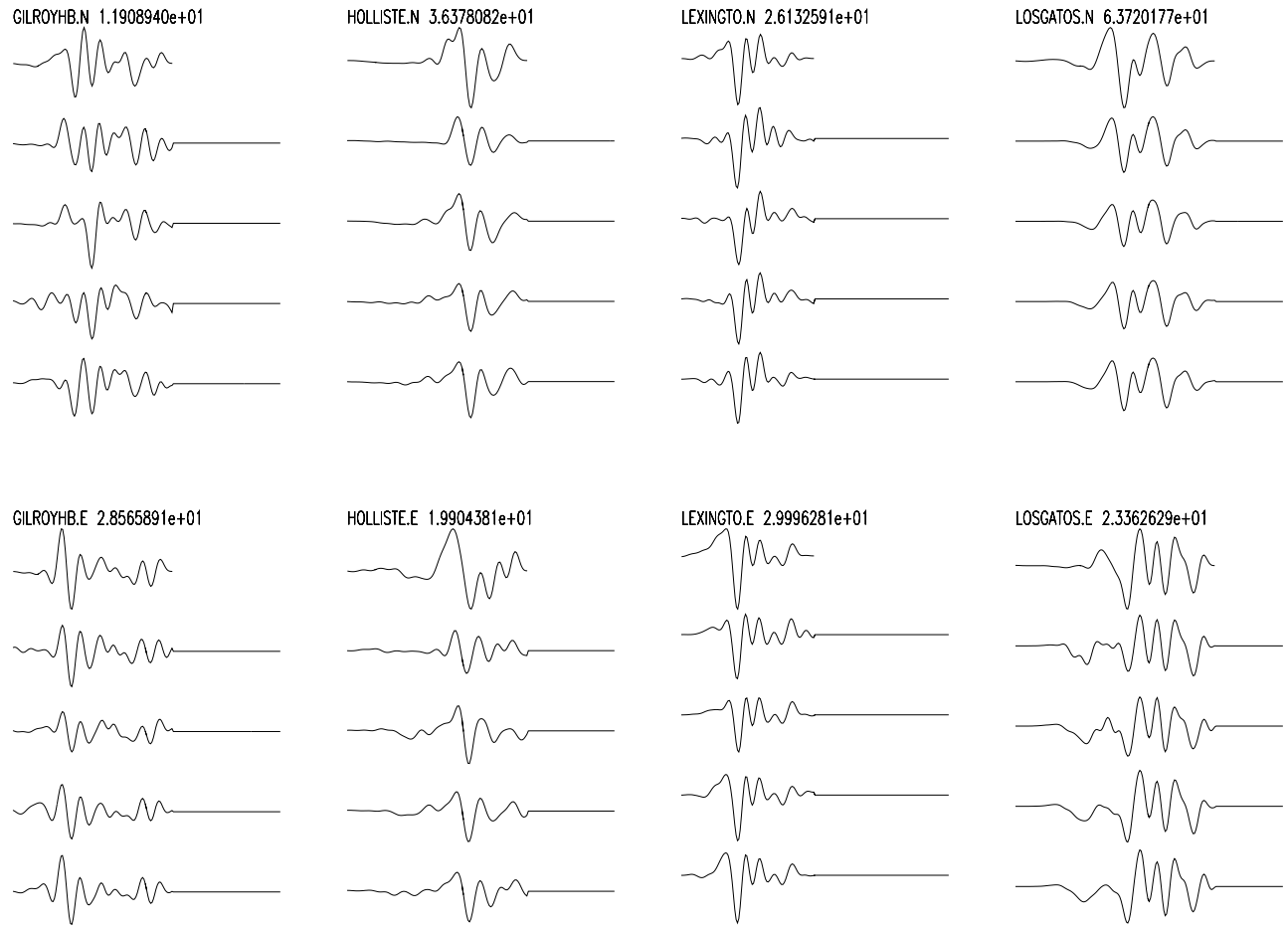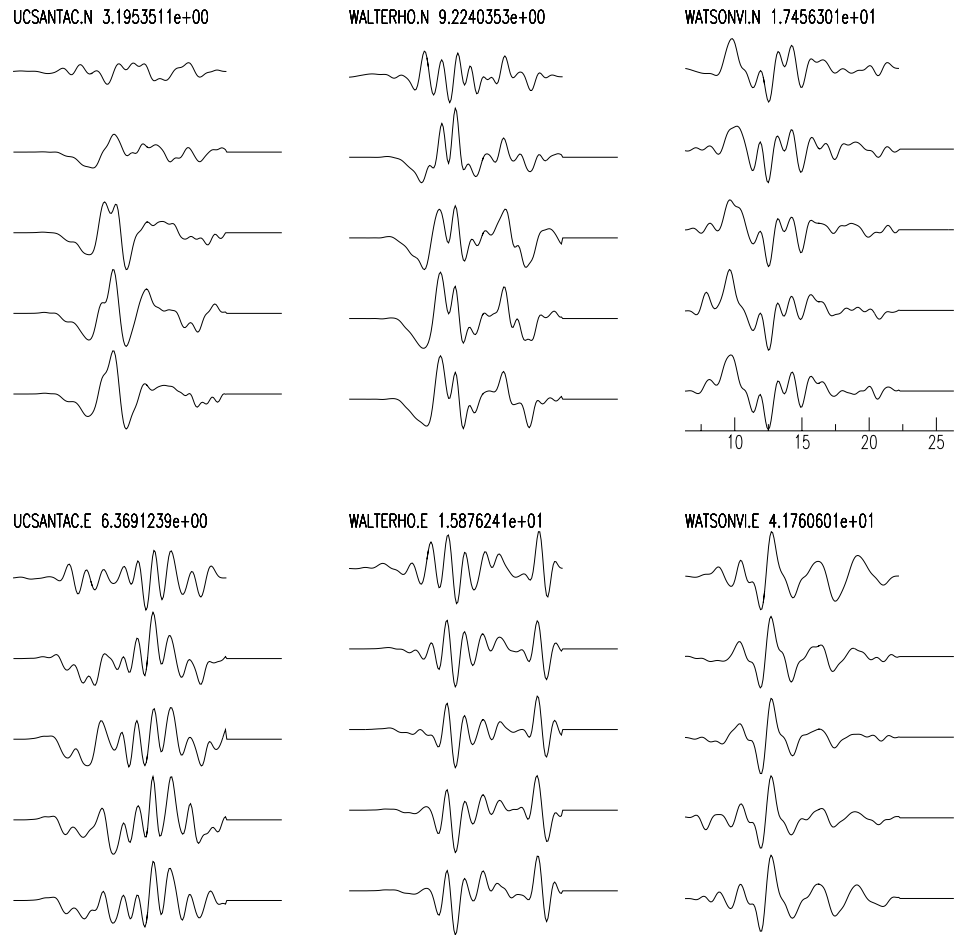eater than ~40 km from the epicenter. The most significant changes in horizontal surface displacements are observed at benchmarks Gilroy and Chamber, located on the southern edge of the rupture plane (Figure 4.14). No improvement was observed at benchmarks American and Biel where the amplitude remains underestimated by a factor of 2, although the orientation is consistent with the data. After changing the model geometry from LP to LP-SAF, residuals in the leveling data increase directly above the northwest and southeast asperities but decrease at stations away from the rupture plane (Figure 4.15).

Results suggest a gradual improvement in fit to the seismic and geodetic data and a decrease in the L2 norm for increasing fault complexity (Table 4.4). While the improvement in fit from model LP to model LP-SAF is significant, the improvement with model THRUST is likely not statistically significant given the increase in model parameters. Slip located north of the hypocenter appears to prefer a dipping structure and consolidates on the top
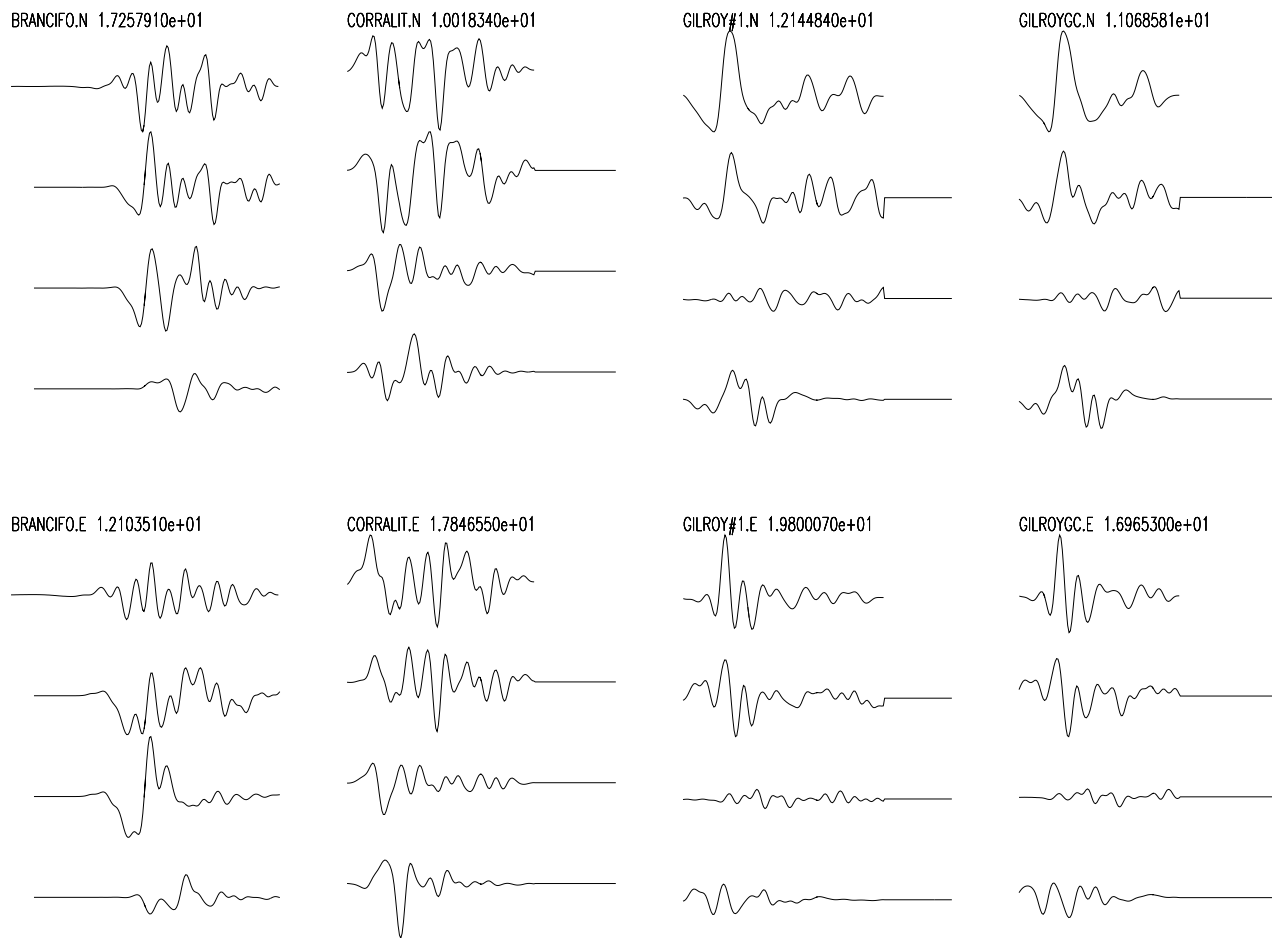
Figure 4.13: Synthetic waveforms are produced for different parts of the slip distribution found for model LP-SAF. The original waveform data (top trace) and the full synthetic (second trace from top) are shown for reference. Forward synthetics for the northwest asperity (third trace from top) and the southeast asperity (bottom trace) illustrate how the components of the slip distribution relate to the data.

Figure 4.13: Continued.

UCSANTAC.N 3.1953511e+00   WALTERHO.N 9.2240353e+00   WATSONVI.N 1.7456301e+01

UCSANTAC.E 6.3691239e+00   WALTERHO.E 1.5876241e+01   WATSONVI.E 4.1760601e+01

Figure 4.13: Continued.

Figure 4.14: Predicted horizontal surface displacements are shown for different model geometries. Chamber and LP1 show the greatest change with the fault geometry.
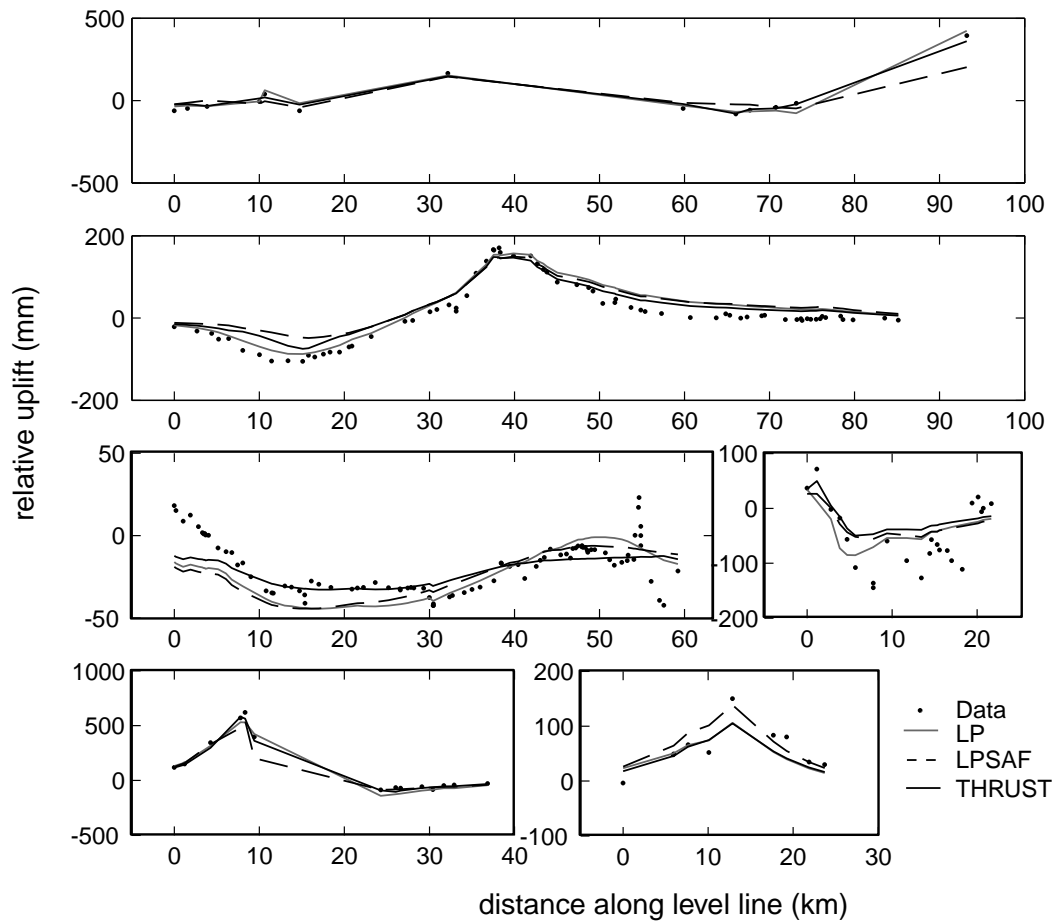
Figure 4.15: Vertical surface displacements are shown for different fault model geometries. A map with that shows the level line segments relative to the epicenter is shown in Figure 4.8d.

portion of the Loma Prieta fault. A common feature for all of the waveform inversions is the oblique slip that propagates away from the hypocenter towards the north, and the strike-slip patch to the south at a depth of $\sim$10 km. Even with a parameterized San Andreas fault, the majority of the slip occurs on the Loma Prieta fault. This supports the assertion that the San Andreas fault did not experience significant moment release for this event.

Inclusion of the shallow thrust plane results in a concentrated patch of strike-slip rupture up-dip of the northwest asperity. Dynamically, it is peculiar to resolve strike-slip motion on the thrust with no corresponding motion on the San Andreas. Regardless of the interaction that may have transpired between the thrust plane and the San Andreas fault, the wedge of crust that is bounded by the two faults is 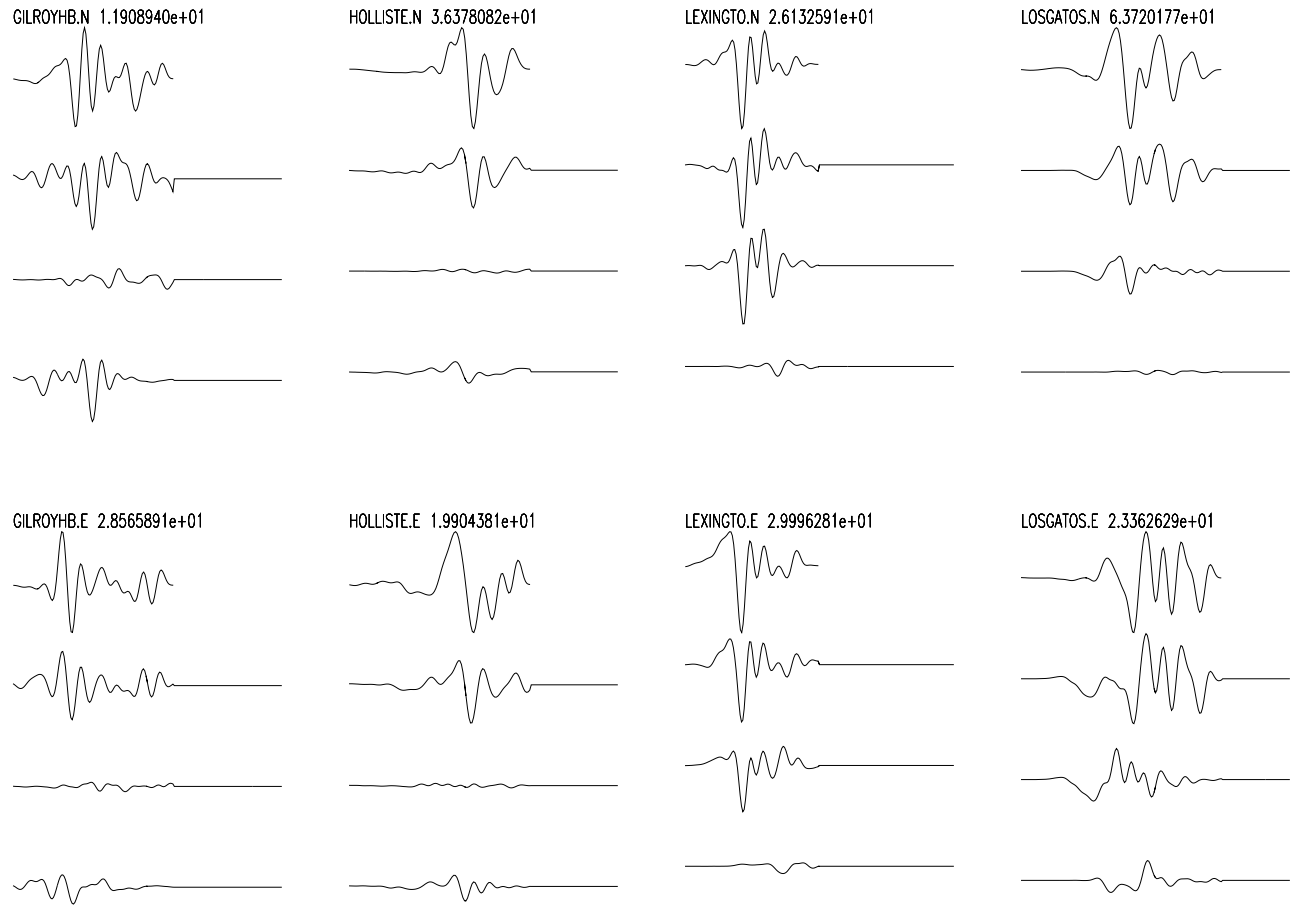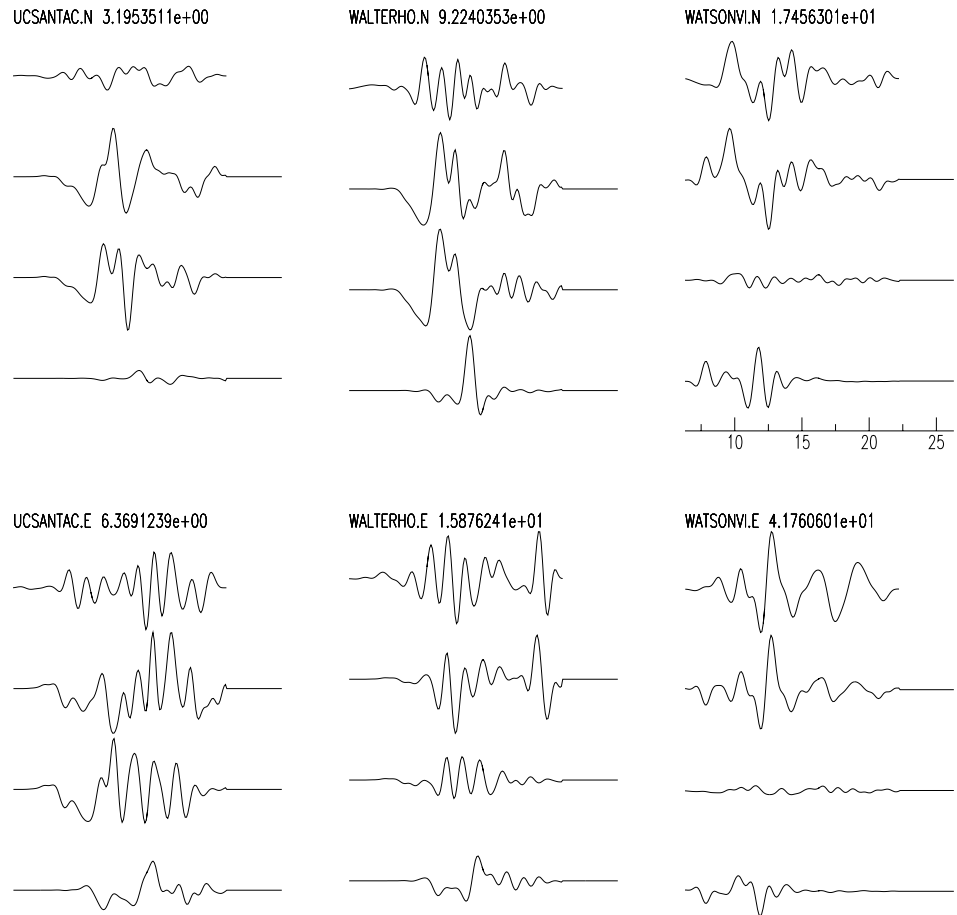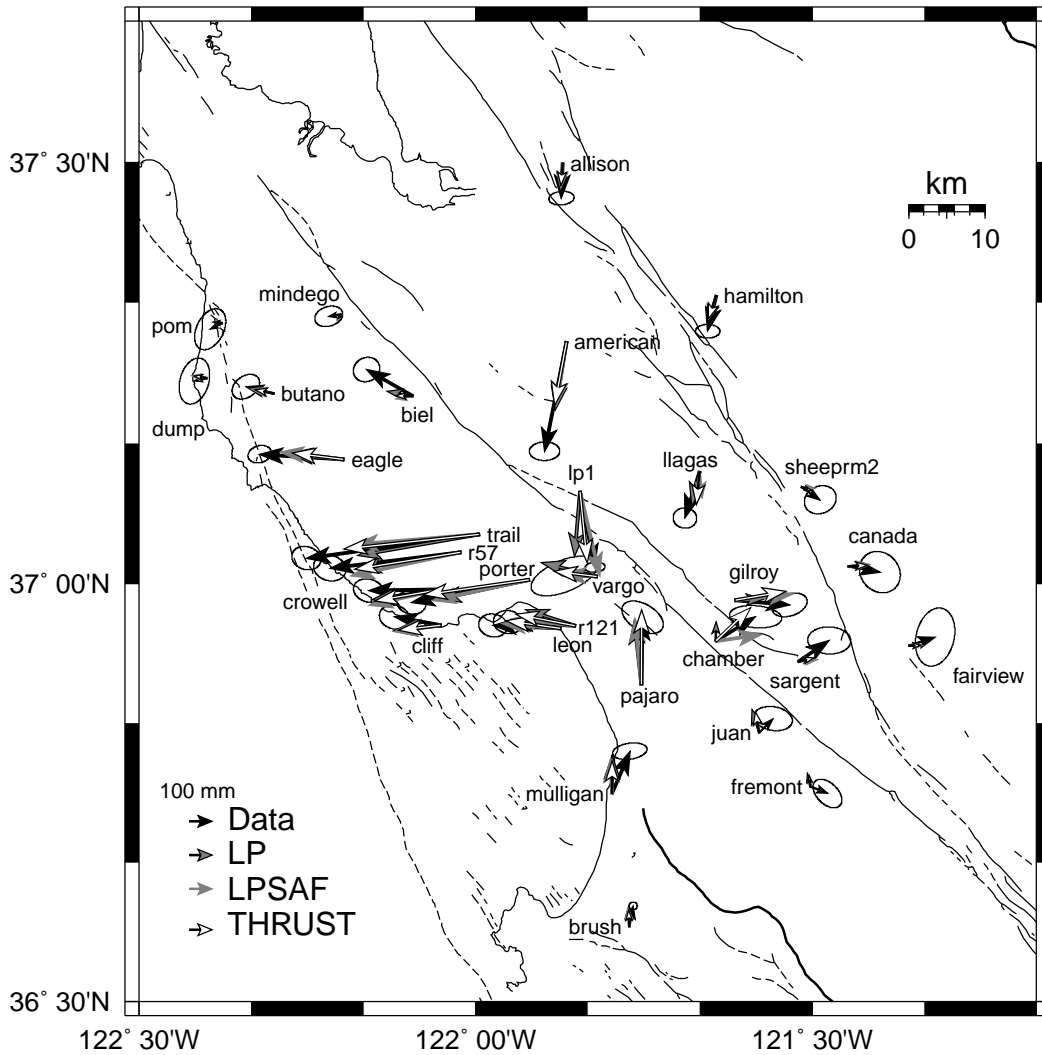illuminated by a cluster of aftershocks with events beginning in the first day following the mainshock. Additionally, *Arnadottir and Segall* [1994] and *Marshall et al.* [1991] found a positive residual in the vertical displacements located directly above this region, suggesting that some local signal is not modeled in their inversions. A similar residual is found in the leveling data and the residual is reduced with the addition of the thrust plane.

While several features discussed in the previous paragraph support the result of slip on the thrust plane, uncertainties in resolving this feature cast doubt on its existence. Slip on this surface occurs late in the rupture history. The anticipated phase arrivals would appear in the coda of the waveforms where definitive modeling is difficult. Forward modeling of this rupture patch produces synthetics with large amplitudes, due to the shallow proximity of the fault to the surface. These large amplitude arrivals are offset by other phases arriving late to the respective station to produce the final synthetic. The two seismic stations showing

the greatest improvement are located to the south of the epicenter away from the patch of slip on the thrust plane. Movement on the thrust at this location is expected to affect the northern stations although none of these stations show significant improvement. The strike-slip component and the resolvability of a signal in the coda lead us to conclude that this feature is either an artifact of the inversion or is a real, but poorly resolved feature in the data. It is also possible that immediate afterslip on the thrust is included in the geodetic data but not in the waveform data.

The aftershock distribution provides an independent assessment of the slip distribution (Figure 4.16). A V-shaped slip distribution with the hypocenter at the apex agrees with the overall structure of the aftershock distribution. A cluster of large aftershocks that occurs within the first hour bound the coseismic slip to the north and up-dip of the rupture. *Beroza* [1991] noted that the location of these aftershocks lies up-dip of the largest slip amplitudes. This is consistent with the northwest asperity being the robust feature of the slip distribution with auxiliary strike-slip activity to the south on a sub-vertical structure.

4.6   Conclusions

In addition to the 3D crustal effects found by *Cormier and Su* [1994], complex rupture on multiple planes can contribute to the variation in published rupture models. Modifying the mainshock rupture surface into a kinked plane consisting of a Loma Prieta fault and a San Andreas fault provides a modest improvement in fit to the data. The inversion prefers slip to reside on dipping surfaces suggesting that little slip may have occurred on a vertical San Andreas fault. It is possible that additional structures participated in the
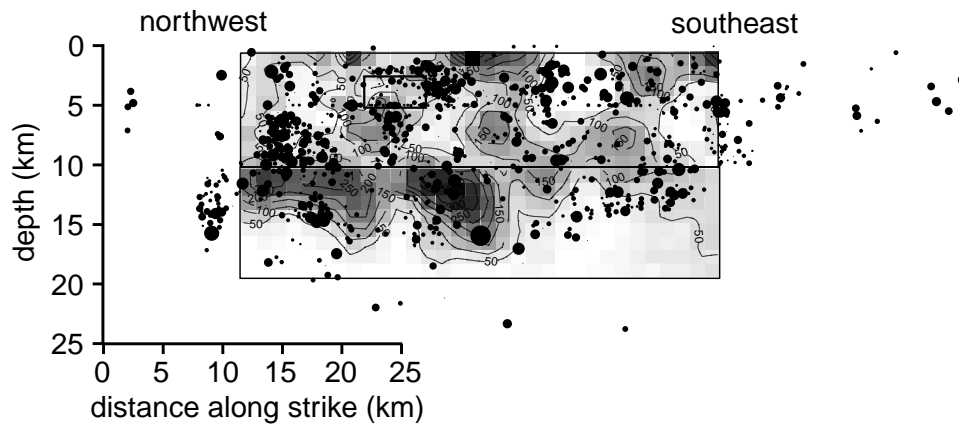
Figure 4.16: The aftershock distribution for events within one hour after the mainshock is plotted over contours of the total slip for model LP-SAF. The figure is oriented from north to south (left to right). Aftershock locations are from *Dietz and Ellsworth* [1997].

Loma Prieta rupture. Distributed slip on parallel structures or a non-planar surface linking the dipping Loma Prieta fault and the vertical San Andreas are also possible. However, the limitations of the data and the unknown structure at depth prevent us from exploring more complex fault models.

4.7   Acknowledgments

Bibliography

Arnadottir, T., and P. Segall, The 1989 Loma Prieta earthquake images from the inversion of geodetic data, *J. Geophys. Res., 99*, 21,835-21,855, 1994.

Aydin, A., and B. M. Page, Diverse Pliocene-Quaternary tectonics in a transform environment, San Francisco Bay region, California, *Geological Society of America Bulletin, 95*, 1303-1317, 1984.

Beroza, G.C, Near-source modeling of the Loma Prieta earthquake: evidence for heterogeneous slip and implications for earthquake hazard, *Bull. Seism. Soc. Am., 81*, 1603-1621, 1991.

Beroza, G. C., and M. D. Zoback, Mechanism diversity of the Loma Prieta aftershocks and the mechanics of mainshock-aftershock interaction, *Science, 259*, 210-213, 1993.

Bürgmann, R., Segall, P., Lisowski, M., and J. Svarc, Postseismic strain following the 1989 Loma Prieta earthquake from GPS and leveling measurements, *J. Geophys. Res., 102*, 4,933-4,955, 1997.

Cormier, V. F., and W. Su, Effects of three-dimensional crustal structure on the estimated slip history and ground motion of the Loma Prieta earthquake, *Bull. Seism. Soc. Am., 84*, 284-294, 1994.

Dietz, D. and W. Ellsworth, Aftershocks of the Loma Prieta Earthquake and their tectonic implications, *U.S. Geol. Surv. Prof. Pap., 1550-D*, 5-47, 1997.

Dietz, D. and W. Ellsworth, The October 17, 1989, Loma Prieta, California, earthquake and its aftershocks: Geometry of the sequence from high-resolution locations, *Geophys. Res. Lett., 17*, 1417-1420, 1990.

Dreger, D., and A. Kaverina, Seismic remote sensing for the earthquake source process and near source strong shaking: A case study of the October 16, 1999 Hector Mine earthquake, *Geophys. Res. Lett., 27*, 1941-1944, 2000.

Dreger, D., Dolenc, D., Stidham, C., Baise, L., and S. Larsen, Evaluating 3D earth models for the purpose of strong ground motion simulation, *Seism. Soc. of America 2001 Spring Meeting,* San Francisco, 2001.

Du, Y., and A. Aydin, Elastic stress relaxation: A mechanism for opposite sense of secondary faulting with respect to a major fault, *Tectonophysics, 257*, 175-188, 1996.

Eberhart-Phillips, D., and A. J. Michael, Seismotectonics of the Loma Prieta, California, region determined from the three-dimensional V_p, V_p/V_s, and seismicity, *J. Geophys. Res., 103*, 21099-21120, 1998.

Foxall, W., Michelini, A., amd T. V. McEvilly, Earthquake travel time tomography of the southern Santa Cruz Mountains: control of fault rupture by lithological heterogeneity of the San Andreas fault zone, *J. Geophys. Res., 98*, 17691-17710, 1993.

Graves, R. W., and D. J. Wald, Resolution analysis of finite fault source inversion using one- and two-dimensional Green's functions, *J. Geophys. Res., 106*, 8745-8766, 2001.

Hanks, T. C., and H. Krawinkler, The 1989 Loma Prieta earthquake and its effects: Introduction to the special issue, *Bull. Seism. Soc. Am., 81,* 1415-1423, 1991.

Hearn, E. H., and R. Bürgmann, The effect of elastic layering on estimates of coseismic slip from surface displacement, unpublished manuscript.

Horton, S., J.G. Anderson, and S.H. Mendez, Frequency-domain inversion for the rupture characteristics during the earthquake using strong motion data and geodetic observations, *U.S. Geol. Surv. Prof. Pap., 1550-A*, 59-74, 1997.

Kaverina, A., Dreger, D., and E. Price, The combined inversion of seismic and geodetic data for the source process of the 16 October 1999 M 7.1 Hector Mine, California, earthquake, *Bull. Seism. Soc. Am., 92*, 1266-1280, 2002.

Kilb, D., Ellis, M., Gomberg, J., and S. Davis, On the origin of diverse aftershock mechanisms following the 1989 Loma Prieta earthquake, *Geophys. J. Internl., 128*, 557-570, 1997.

Lawson, C. L., and R. J. Hanson, *Solving least squares problems*, Prentice-Hall, 1974.

Marshall, G. A., Stein, R., and W. Thatcher, Faulting geometry and slip from co-seismic elevation changes: the 18 October 1989, Loma Prieta, California, earthquake, *Bull. Seism. Soc. Am., 81*, 1660-1693, 1991.

McLaughlin, R. J., Langenheim, V. E., Schmidt, K. M., Jachens, R. C., Stanley, R. G., Jayko, A. S., McDougall, K. A., Tinsley, J. C., and Z. C. Valin, Neogene contraction between the San Andreas fault and Santa Clara valley, San Francisco Bay region, California, *Int. Geol. Rev., 41*, 1-30, 1999.

McNally, K. C., Simila, G. W., and J. G. Brown, Main-shock and very early aftershock activity, The Loma Prieta, California, earthquake of October 17, 1989-Earthquake occurrence: *U.S. Geol. Surv. Prof. Pap., 1550-A*, 147-170, 1996.

Michael, A.J., Ellsworth, W.L., and D. H. Oppenheimer, Coseismic stress changes induced by the Loma Prieta, California, earthquake, *Geophys. Res. Lett., 17*, 1441-1444, 1990.

Okada, Y., Surface deformation due to shear and tensile faults in a half-space, *Bull. Seism. Soc. Am., 75*, 1135-1154, 1985.

Pujol, J., Comment on "The 1989 Loma Prieta earthquake imaged from the inversion of geodetic data" by Thora Arnadottir and Paul Segall, *J. Geophys. Res., 101*, 20133-20136, 1996.

Saikia, C. K., Modified frequency-wave-number algorithm for regional seismograms using Filon's quadrature-modeling of L(g) waves in eastern North America, *Geophys. J. Int. 118*, 142-158, 1994.

Spudich, P., *ed*, The Loma Prieta Earthquake of October 16, 1989, Main-shock characteristics, *U.S. Geol. Surv. Prof. Pap., 1550-A*, 1996.

Steidl, J.H., R.J. Archulta, and S.H. Hartzell, Rupture history of the 1989 Loma Prieta California earthquake, *Bull. Seism. Soc. Am., 81*, 1573-1602, 1991.

Snay, R. A., Neugebauer, H. C., and W. H. Prescott, Horizontal deformation associated with the Loma Prieta earthquake, *Bull. Seism. Soc. Am., 81*, 1647-1659, 1991.

Schwartz, S. Y., Orange, D. L., amd R. S. Anderson, Complex fault interactions in a restraining bend on the San Andreas fault, southern Santa Cruz Mountains, California, *Geophys. Res. Lett., 17*, 1207-1210, 1990.

Wald, D., D.V. Helmberger, and H.T. Heaton, Rupture model of the 1989 Loma Prieta earthquake from the inversion of strong-motion and broadband teleseismic data, *Bull. Seism. Soc. Am., 81,* 1540, 1991.

Wald, D. J., and R. W. Graves, Resolution of finite fault source inversion using 1D and 3D Green's Functions, Part II: combining seismic and geodetic data, *J. Geophys. Res., 106*, 8767-8788, 2001.

Chapter 5

Predicting the creep response on the Hayward fault following the 1906 San Francisco earthquake

5.1   Introduction

Faults that exhibit surface creep are known to change their creep rate following large earthquakes on neighboring faults. Induced surface creep was documented on several Bay Area faults following the 1989 Loma Prieta earthquake ($\mathbf{M}_w$ 6.9). Slip responses range from accelerated/decelerated creep to a temporary reversal in slip direction [*Galehouse,* 1997]. A reduction in creep was observed along the southern Hayward fault which typically exhibits surface creep $\sim$9 mm/yr (Figure 5.1). *Lienkaemper et al.,*[1997] find that a $\sim$0.1 MPa reduction in shear stress imposed by the 1989 Loma Prieta earthquake is enough to alter the creep rate. Larger events, such as the 1906 San Francisco earthquake ($\mathbf{M}_w$ 7.8), are expected to produce significant postseismic transients thereby imposing a time-dependent creep response on adjacent faults. Given the significantly greater moment release of the 1906 event, the creep response on neighboring faults is expected to be much larger following the

1906 event than that observed following 1989 event.

Despite the lingering stress shadow [*Parsons*, 2002; *Harris and Simpson*, 1998; *Kenner and Segall*, 1998], there is no evidence showing that creep rates along the Hayward fault were reduced in the decades following the 1906 event. No direct observations of the surface creep response on the Hayward fault were documented in the years immediately following the 1906 earthquake on the San Andreas fault. *Lienkaemper and Galehouse* [1997] reconstruct the surface creep history on the Hayward fault using offset cultural features, such as curbs and other man-made structures. Sites that contain multiple measurements over varying time periods suggest that time-averaged creep rates have remained constant for much of the twentieth century (Figure 5.2). If creep rates were reduced, this reduction must have recovered by the early 1920's. The quick recovery to the contemporary creep rates is surprising given that seismicity rates have still not recovered to pre-1906 values after nearly a full century [*Bakun*, 1999]. I attempt to explain how creep rates could recover on the Hayward fault by performing numerical simulations of surface creep utilizing the full stressing history imposed during both the coseismic rupture and postseismic relaxation of the 1906 event. The determination of when surface creep recovers on regional faults has important implications for how the stress shadow developed both in space and time.

5.2   Methodology

The complex behavior of the creeping section of the Hayward fault is modeled using a rate-and-state constitutive law. Rate-and-state friction originated from laboratory observations of rock friction [*Dieterich*, 1979a, 1979b; *Ruina*, 1983]. Since the introduc-
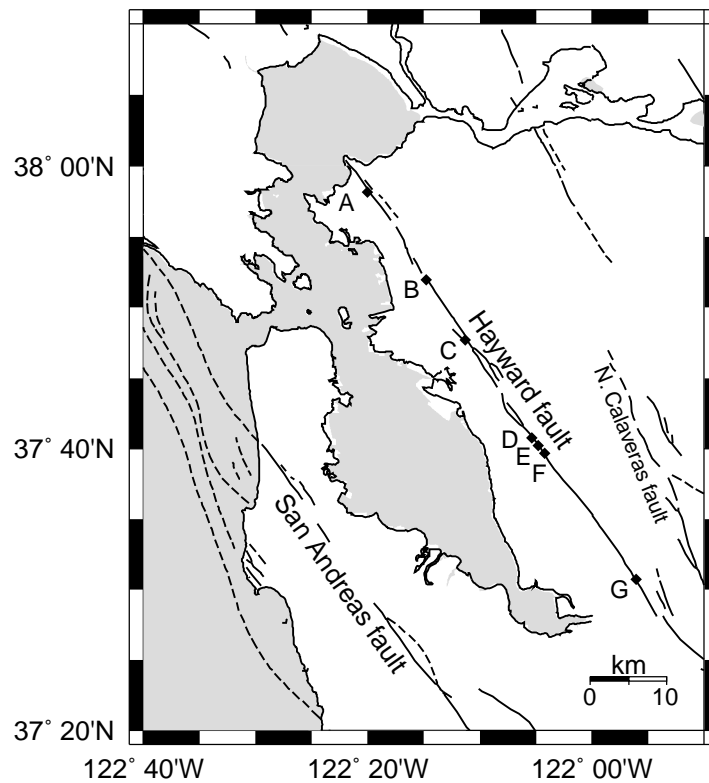
Figure 5.1: A map of the San Francisco Bay Area shows the location of major faults. The epicenter of the Loma Prieta earthquake is located along the San Andreas fault just south of the region shown. The 1906 earthquake ruptured a 400 km segment of the San Andreas fault, including the segment shown. Letters A-F along the Hayward fault mark the location of time-averaged creep measurements shown in Figure 5.2. Location G marks the observation point for the data in Figure 5.3.
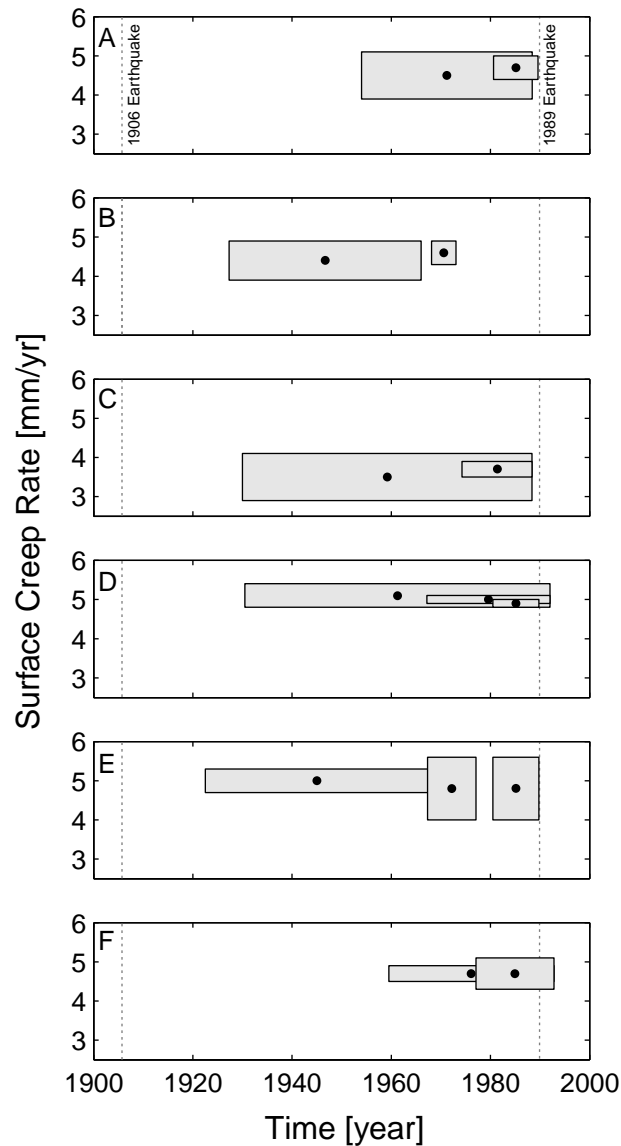
Figure 5.2: (A-F) Time-averaged creep rate data from offset cultural features [*Lienkaemper and Galehouse*, 1997] correspond to locations A-F in Figure 5.1. Each gray box represents one observation where the height of the box signifies the error of the measurement and the width of the box designates the time period over which the displacement is averaged. The data suggest that surface creep rates along the Hayward fault have remained constant despite a lingering stress shadow that has depressed regional seismicity rates.

tion of the constitutive law, the formulation has been applied to both experimental and theoretical fault studies [see references in *Marone, 1998*]. I use a "Dieterich-Ruina" formulation of the rate-and-state constitutive law to model the response of a creeping fault to a time-dependent stress perturbation,

$$\mu(\dot{\delta}, \theta) = \mu + A \ln(\dot{\delta}/\dot{\delta}_s s) + B \ln(\theta/\theta_s s), \tag{5.1}$$

$$\partial\theta(\delta, \sigma) = (1/\dot{\delta} - \theta/D_c)\partial\delta + (\alpha\theta/B\sigma)\partial\sigma. \tag{5.2}$$

Equation (1) describes the dependence of the coefficient of friction, μ, on the slip rate, $\dot{\delta}(t)$, and the state function, $\theta(\delta, \sigma)$. The notation is summarized in Table 5.1. Equation (2) defines the evolution of state with slip and normal stress. The dots over the variables designate derivatives with respect to time. Equation (2) utilizes the dependence on normal stress described by *Linker and Dieterich* [1992]. The fault is modeled as a one-dimensional elastic system which requires the following elastic coupling term,

$$\dot{\mu} = (\dot{\tau}(t) - k\dot{\delta}(t))/\sigma(t). \tag{5.3}$$

Taking the derivative of equation (1) with respect to time and equating it to equation (3) produces a second-order differential equation,

$$\ddot{\delta} - \frac{\dot{\delta}}{A}[B(\frac{\dot{\delta}}{D_c} - \frac{1}{\theta}) + \dot{\sigma}(\frac{\alpha}{\sigma} - \frac{\tau}{\sigma^2}) + \frac{\dot{\tau}}{\sigma}] = 0. \tag{5.4}$$

Combining equation (4) with (2) provides a set of differential equations that are solved numerically using a Runga-Kutta method. We must consider the possibility that the creeping section can slip in the reverse direction, i.e. left-laterally. The natural log dependence in (1) forbids negative slip rate values. To overcome this complication, the positive slip direction is defined to be coincident with the shear stress.

5.2.1 Determination of Fault Parameters

The fault constitutive parameters A, B, D_c, and α are unique to the fault surface and are dependent on the type of rock, the maturity of the gouge material, and the width of the shear zone along with other factors that define the state of the fault. In order to demonstrate that our choice of values is reasonable for modeling an actual fault system, the surface slip history observed following the 1989 Loma Prieta earthquake along the southern Hayward fault is reproduced (Figure 5.3). Initial conditions are determined assuming that the fault slips at a secular rate of 10 mm/yr [*Lienkaemper et al.*, 1991]. Unfortunately, no creep observation was made just prior to 1989 that document an immediate coseismic response. *Lienkaemper et al.* [2001] predict 4 mm of left-lateral slip on a frictionless fault for the expected static stress change. Lacking evidence of an immediate creep response, it is assumed that the initial shear stress on the fault is completely reduced by the coseismic stress reduction. Therefore, our model does not predict a coseismic creep event. The left-lateral response in the following years is driven by postseismic stress redistribution in the crust. The stress history on the Hayward fault from interseismic and postseismic processes are parameterized by calculating the shear and normal stressing rate imposed on the Hayward fault using the linear postseismic displacement rates determined by *Bürgmann et al.* [1997] for the four years following the 1989 Loma Prieta earthquake. An interseismic loading rate of 0.012 MPa/yr is used after 1993 [*Furlong and Verdonck*, 1994; *Parsons, in press*]. Trial and error is used to locate a combination of parameters that adequately reproduce the surface slip record in addition to a pattern search method to maximize the fit and refine the parameters. The values used to model the creep response are listed in Table 5.1. While

the values determined for A, B, D_c, and α are not necessarily unique, it is comforting that they fall within the range of published laboratory results. This suggests that small-scale rock friction experiments may have a direct application for modeling real fault systems.

5.2.2 Coseismic and Postseismic Stressing History

In order to predict how the Hayward fault would respond to the 1906 earthquake, both the constitutive parameters of the fault discussed above and its full stressing history must be defined. The 1906 coseismic slip model of *Thatcher et al.* [1997] is used to calculate the coseismic stress change resolved onto the southern portion of the Hayward fault. A right-lateral, shear stress change of -0.3 MPa and a -0.1 MPa change in compressional normal stress is calculated at a depth of 1 km. Because the postseismic response is expected to play an important role in driving regional deformation following a large earthquake, I incorporate the postseismic stressing histories calculated by *Kenner and Segall* [1999] for the 1906 event. *Kenner and Segall* [1999] use an anti-plane finite and infinite element code to calculate the stress imposed on Bay Area faults as a function of time for various rheological models (Figure 5.4). The "crustal fault model" represents an elastic layer over a Maxwell viscoelastic half-space. The "shear zone model" includes vertical, low-viscosity shear zones beneath the San Andreas, Hayward, and Calaveras faults. The "detachment model" connects the three vertical shear zones at a depth of 15 km with a horizontal zone of viscoelastic material.
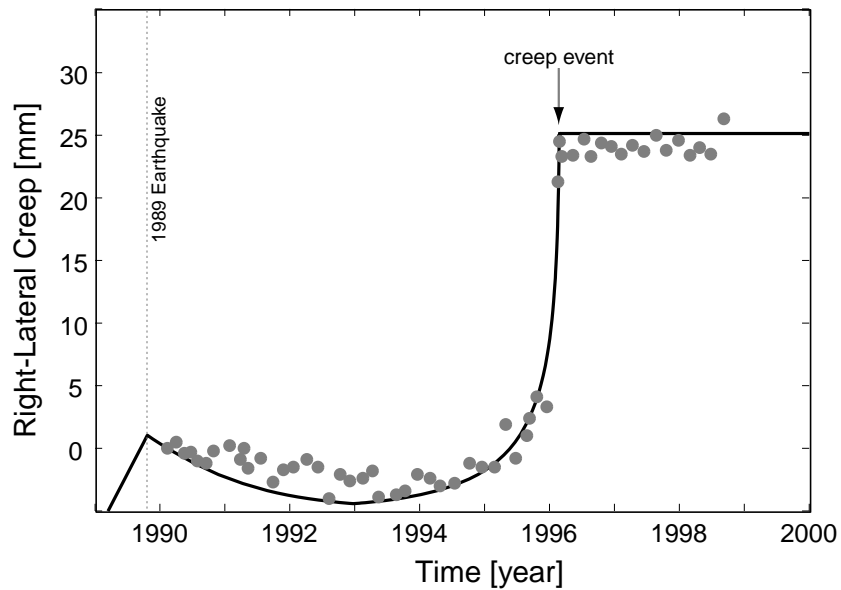
Figure 5.3: The surface creep response on the southern Hayward fault following the 1989 Loma Prieta earthquake is modeled with a rate-and-state constitutive law. The alignment array data (dots) were collected at location G in Figure 5.1 by *Lienkaemper et al.*[1997]. The modeled creep response (solid line) is calculated using the parameter values in Table 5.1. The fault creeps at a rate of 10 mm/yr prior to the 1989 earthquake.
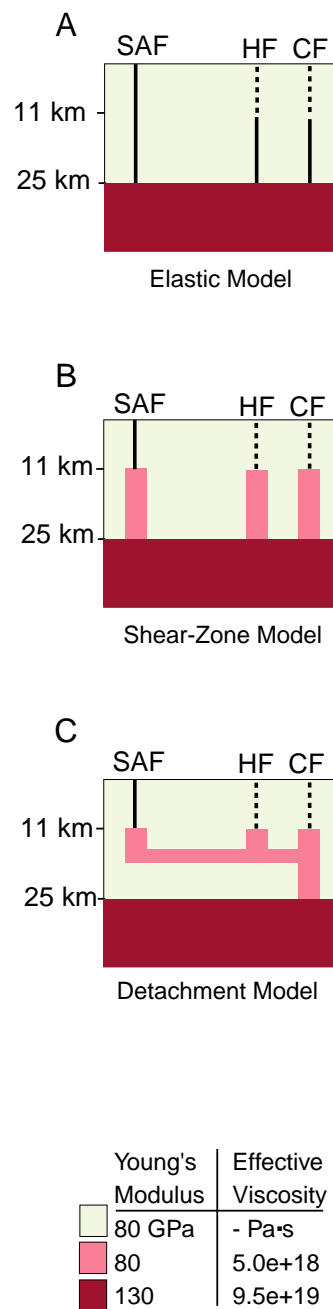
Figure 5.4: The postseismic stressing history imposed on the shallow Hayward fault following the 1906 San Francisco earthquake is calculated by *Kenner and Segall*[1999] for three rheological models: (A) an elastic layer over a viscoelastic mantle, (B) an elastic layer with vertical viscoelastic shear zone beneath the San Andreas (SAF), Hayward (HF), and Calaveras (CF) faults, and (C) an elastic layer with vertical and horizontal shear zones.

5.3   Results of Numerical Modeling

After defining the various fault parameters and the stressing history on the Hayward fault, the set of differential equations are allowed to evolve with time producing a synthetic surface slip response following the 1906 earthquake. The same initial conditions used for the Loma Prieta calculation are used for 1906 event. Figure 5.5a shows the predicted slip response for the "crustal fault model" of *Kenner and Segall* [1999]. The record begins with a steady-state right-lateral slip that is interrupted by a left-lateral creep event coincident with the 1906 coseismic event on the San Andreas fault. The initial right-lateral shear stress is eliminated by the coseismic stress change and the excess stress drives an immediate creep event in the opposite direction. The left-lateral response quickly decays before a series of right-lateral creep events signal the transition to the contemporary rate of 10 mm/yr of right-lateral slip. Since the coseismic fault does not penetrate the entire elastic layer, very little postseismic stress is transferred to the Hayward fault for the "crustal fault model". The inclusion of vertical shear zones beneath the three major faults in the Bay Area acts to delay the return to the contemporary creep behavior by approximately a decade, as shown in Figure 5.5b. The creep response using the stressing history from the horizontal shear zone model is shown in Figure 5.5c. As discussed by *Kenner and Segall* [1999], the horizontal shear zone acts to transfer additional stress to the Hayward and Calaveras faults thereby producing a more intense and drawn out postseismic response. In our simulations, this drives left-lateral creep on the fault for several decades and the contemporary creep rate does not recover for more than a century.
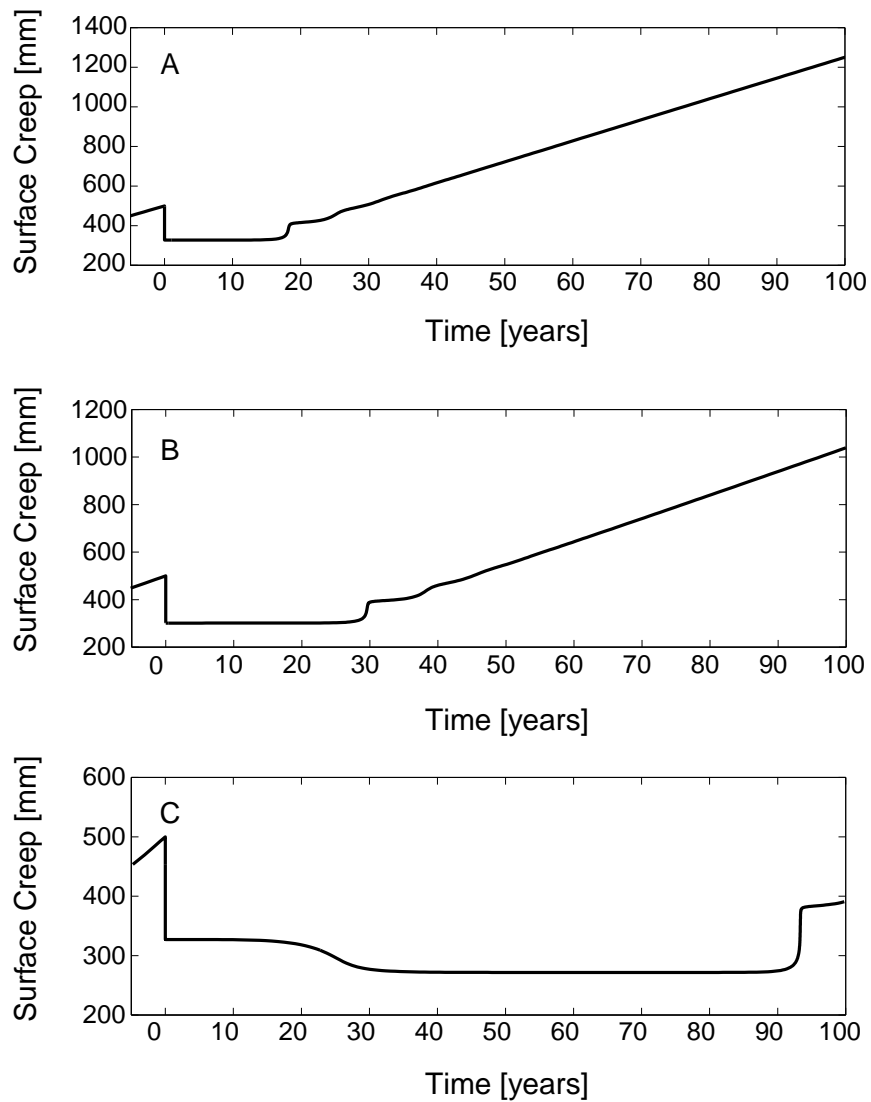
Figure 5.5: Predicted surface creep response on the southern Hayward fault following the 1906 San Francisco earthquake using the postseismic stressing history of *Kenner and Segall* [1999]. The duration of time required for creep rates to recover depends on the rheological model: (A) a crustal fault model, (B) a shear zone model, and (C) a horizontal shear zone (detachment) model (see Figure 5.4). Results suggest that the apparent recovery of creep rates shown in Figure 5.2 cannot be explained by the horizontal shear zone model.

5.4 Discussion

The three rheological models used to compute the stressing history provide an opportunity to test the sensitivity of the surface creep response to varying models of the Bay Area. The different rheological models produce observable differences in the surface creep response on the Hayward fault. Our modeling suggests that the horizontal shear zone model does not agree with the time-averaged slip rate data shown in Figure 5.2. Thus, observations of surface creep can be used not only for fault monitoring, but also as a tool to discriminate between crustal rheologies.

A left-lateral creep event would not be surprising given the large coseismic static stress change for the 1906 event. A simple elastic model where the Hayward fault is allowed to slip freely from the surface to a depth of 1 to 10 km predicts 0.03 to 0.21 m, respectively, of left-lateral slip. It should not be surprising that no observations of this left-lateral creep exist given the minimal cultural development that extended across the Hayward fault in the early part of the twentieth century, in addition to the chaos that ensued in the aftermath of the 1906 event. The greatest potential for a documented observation would exist in the deformation of railroad tracks that crossed the Hayward fault in Fremont. *Cluff and Steinbrugge*[1966] and *Bonilla*[1966] summarize the information obtained from records and accounts detailing the repair of railroad tracks during the first half of the twentieth century. There exists no mention of left-lateral movement across the tracks along the southern Hayward fault in 1906. However, *Forbes*[1914] mentions that activity was observed along the fault.

A 1965 survey of the railroad tracks built in 1869 (near site G, Figure 3.1) provides

a time-averaged creep rate estimate of $>8.5\pm0.6$ mm/yr, which is consistent with pre-Loma Prieta slip rate measurements [*Lienkaemper and Galehouse*, 1997]. While this is the only estimate that extends through 1906, the cumulative slip includes an unknown amount of afterslip from the 1868 earthquake (**M** 6.8) on the Hayward fault. Therefore, it is impossible to extract definitive information about the creep response in the 16 years immediately following the 1906 event. If it is assumed that no creep occurred from 1906 to 1922 and that the creep rate was >8.5 mm/yr after 1922, then a minimum time-averaged rate of 12 mm/yr is required between 1869 and 1906. Any left-lateral creep following 1906 would require additional right-lateral afterslip to offset the cumulative slip.

The major argument against sustained left-lateral creep or a prolonged period of reduced creep on the Hayward fault following 1906 is that historical creep rates measured from offset cultural features show no reduction compared to pre-Loma Prieta creep rates measured by modern instruments. *Cluff and Steinbrugge*[1966] document $\sim$15 cm of slip between 1949 and 1957 while no slip was observed during the preceding and following years, suggesting a transient creep event. These observations qualitatively agree with our numerical simulations which suggest that a series of large creep events preceded a return to the contemporary creep rate.

5.5   Conclusions

The rate-and-state simulations illustrate how right-lateral surface slip rates could quickly recover on the Hayward fault despite there being a lingering stress shadow at depth. The recovery of right-lateral creep suggests that the background loading became dominant

over the postseismic unloading within a couple of decades after the 1906 event. Our modeling results are consistent with time-average slip rates measured from offset cultural features. The modeling of surface creep can provide an additional constraint on lithospheric models [such as *Kenner and Segall*, 1999; *Parsons, in press*] which aim to estimate the time-dependent seismic hazard associated with the reduction of the 1906 stress shadow.

5.6 Acknowledgements

Table 5.1: Notation and Parameter Values

A	laboratory fit parameter	0.009
B	laboratory fit parameter	0.013
D_c	critical slip distance	4 mm
α	laboratory fit parameter	0.6
k	fault stiffness	0.0012 MPa/mm
τ	shear stress	-
σ	normal stress	-
δ	slip	-
θ	state variable	-

Bibliography

Bakun, W. H., Seismic Activity of the San Francisco Bay Region, *Bull. Seism. Soc. Am.,* *89,* 764-784, 1999.

Bonilla, M. G., Deformation of railroad tracks by slippage o the Hayward fault in the Nile District of Fremont, California, *Bull. Seism. Soc. Am., 56,* 281-289, 1966.

Bürgmann, R., Segall, P., Lisowski, M., and J. Svarc, Postseismic strain following the 1989 Loma Prieta earthquake from GPS and leveling measurments, *J. Geophys. Res., 102,* 4933-4955, 1997.

Cluff, B., and K. V. Steinbrugge, Hayward fault slippage in the Irvington-Niles Districts of Fremont, California, *Bull. Seism. Soc. Am., 56,* 257-279, 1966.

Dieterich, J., Modeling of rock friction, 1. Experimental results and constitutive equations, *J. Geophys. Res., 84,* 2161-2168, 1979a.

Dieterich, J., Modeling of rock friction, 2. Simulation of preseismic slip, *J. Geophys. Res., 84,* 2169-2175, 1979b.

Furlong W. L., and D. Verdonck, Three-dimensional lithospheric kinematics in the Loma Prieta region, California: Implications for the earthquake cycle, *U.S. Geol. Surv. Prof. Pap., 1550-F,* 103-131, 1994.

Forbes, H., Report on the underground waters of Niles cone, November 1913 to April 1914, *Water Res. Of Calif.,* 1914.

Galehouse, J. S., Effect of the Loma Prieta earthquake on fault creep rates in the San Francisco Bay region, *U.S. Geol. Surv. Prof. Pap.,* 1550D, 193-207, 1997.

Harris, R. A., and R. W. Simpson, Suppression of large earthquakes by stress shadows: A comparison of Coulomb and rate-and-state failure, *J. Geophys. Res., 103,* 24439-24451, 1998.

Kenner, S., and P. Segall, Time-dependence of the stress shadowing effect and its relation to the structure of the lower crust, *Geology, 27,* 119-122, 1999.

Lienkaemper, J. J., Borchardt, G., and M. Lisowski, Historic creep rate and Potential for seismic slip along the Hayward fault, California, *J. Geophys. Res., 96,* 18261-18283, 1991.

Lienkaemper, J. J., and J. S. Galehouse, Revised long-term creep rates on the Hayward fault, Alameda and Contra Costa counties, California, *U.S. Geol. Surv. Open File Rep.,* 97-690, 1997.

Lienkaemper, J. J., Galehouse, J. S., and R. W. Simpson, Creep response of the Hayward Fault to stress changes caused by the Loma Prieta earthquake, *Science, 276,* 2014-2016, 1997.

Linker, M. I., and J. H. Dieterich, Effects of variable normal stress on rock friction: observations and constitutive equations, *J. Geophys. Res., 97,* 4923-4940, 1992.

Marone, C., Laboratory-derived friction laws and their application to seismic faulting, *Annu. Rev. Earth Planet. Sci., 26,* 643-696, 1998.

Parsons, T., Post-1906 stress recovery of the San Andreas fault system calculated from three-dimensional finite element analysis, *J. Geophys. Res., 10.1029/2000JB000082,* 2002.

Ruina, A., Slip instability and state variable friction laws, *J. Geophys. Res., 88,* 10395-10370, 1983.

Thatcher, W., G. Marshall, and M. Lisowski, Resolution of fault slip along the 470-km-long rupture of the great 1906 earthquake and its implications, *J. Geophys. Res., 102,* 5353-5367, 1997.

Appendix A

Reduction of Atmospheric Errors

Atmospheric artifacts are shared amongst those interferograms that use common SAR scenes. While these errors are not reduced by a direct least squares inversion, they can be minimized through a smoothing constraint. Assume that model parameter, m_{ij}, represents the deformation during the time step between SAR scene acquisitions $\mathbf{L}_i$ and $\mathbf{L}_j$. In the following notation, i and j represent two points in time rather than a pixel location. The range change for an interferogram, r_{ij}, includes the crustal deformation signal, f_{ij}, common atmospheric artifacts associated with either SAR scene, e_i and e_j, and random error, a_{ij}.

$$r_{ij} = f_{ij} + e_i - e_j + a_{ij} \tag{A.1}$$

The least squares inversion acts to eliminate the uncorrelated errors leaving the model parameters, m_{ij}, to be a combination of deformation and correlated errors.

$$m_{ij} = f_{ij} + e_i - e_j \tag{A.2}$$

A smoothing constraint minimizes the roughness of the solution defined as $\|\nabla^2 \mathbf{m}\|_2$. The Laplacian smoothing operator is approximated using a finite difference approximation.

$$\nabla^2 x \simeq \frac{x_{i+1} - 2x_i + x_{i-1}}{\Delta t^2} \tag{A.3}$$

The smoothing operator assumes less deformation to occur during short time periods, as would be expected for tandem pairs (1 day interferograms). Applying (A3) to (A2) we can solve for the roughness.

$$\|\nabla^2 \mathbf{m}\|_2 = \sum \left(\frac{f_{(j+1)j} - 2f_{ij} + f_{(i-1)i} + e_{i-1} - 3e_i + 3e_j - e_{j+1}}{\Delta t^2} \right)^2 \tag{A.4}$$

If we assume that the crustal deformation signal is continuous and much smaller than e_i, then $f_{(j+1)j} - 2f_{ij} + f_{(i-1)i} \approx 0$. If the sum of the cross products of the correlated errors is

assumed to be zero (i.e. $\sum e_i e_j \approx 0$) then the roughness is dependent on the sum of squares of the correlated errors.

$$\|\nabla^2 \mathbf{m}\|_2 \approx \sum_{i=1}^{S} c_i e_i^2 \text{ where } c_i \text{ is a constant.} \qquad (A.5)$$

Thus by including a smoothing constraint, correlated errors will be minimized depending on the choice of smoothing weight.

Appendix B

ROI_PAC Resource Guide

B.1 Introduction

This resource is designed to assist new users in gaining familiarity with the Repeat Orbit Interferometry Package, ROI_PAC, developed at JPL/Caltech. This is not intended to be a complete manual, but rather a cheat sheet or guide on the basics of producing an interferogram. It is assumed that the user has some familiarity with UNIX. A working knowledge of Perl is also recommended in order to troubleshoot problems. This resource was originally created for use by graduate and undergraduate students at UC Berkeley, with the intent to provide a quick and efficient resource for learning how to process interferograms using ROI_PAC. With the recent public release of the software, it is hoped that other users might benefit from these instructions. This resource is currently available as an online supplement located at http://www.seismo.berkeley.edu/~dschmidt/ROI_PAC/. Additional tips and revised instructions will be posted accordingly.

B.2 First-Time Installation

These instructions are for users who are installing ROI_PAC v1.0beta on their computer system for the first time. The appropriate UNIX commands are shown following the percent sign which represents the command prompt. Additional information is found in the documentation that accompanies the software.

1. **Download the software from JPL.** Contact Jennifer Schlickbernd (jennifer.k.schlickbernd@jpl.nasa.gov) for a license and instructions on how to obtain the software.

2. **Un-tar the archived file.**

   % gtar xf roi_pac_dist.tar

3. **Read the documentation.** Read through the files found in ROI_PAC_DIST/GUIDE.

   % cd /home/ROI_PAC_DIST/GUIDE
   % vi *

4. **Configure environmental variables.** Alter SAR_CONFIG according to the instructions found in ROI_PAC_DIST/GUIDE/Setup and source the file. For now, you only need to edit the bold text in the SAR_CONFIG file shown below.

setenv	SAR	”**$HOME**/ROI_PAC_DIST”
setenv	SAR_PRC_DIR	”$SAR/**TEST_DIR/PRC**”
setenv	SAR_ODR_DIR	”$SAR/ERS/Delft”
setenv	ROI_PAC	”$SAR/**ROI_PAC**”
setenv	FFTW_LIB	”$SAR/FFTW/$ARCHC””_fftw_lib”
setenv	INT_LIB	”$ROI_PAC/LIB/$ARCHC”
setenv	MY_SAR	”$SAR”
setenv	INT_BIN	”$ROI_PAC/BIN/$ARCHC”
setenv	INT_SCR	”$ROI_PAC/INT_SCR”
setenv	OUR_SCR	”$MY_SAR/OUR_SCR”
setenv	SAR_TAPE	”/dev/rmt/0mn”

```
% cd ..
% cp SAR_CONFIG.master.csh SAR_CONFIG
% vi SAR_CONFIG
% source SAR_CONFIG
```

5. **Compile executables.** You can skip this step and see if the executables in ROI_PAC_DIST/ROI_PAC/BIN/SXX work for your system. Otherwise you will need to recompile everything (good luck!).

```
% cd ../ROI_PAC
% make clean
% make all
% make install
% make clean
```

6. **Update path to perl.** The path to the perl executable may be different on your machine than is used in the ROI_PAC scripts. There is a simple script that will edit this path for you.

```
% cd /home/ROI_PAC_DIST/ROI_PAC/INT_SCR
% chgperlpath.pl
```

7. **Test the installation.** You will need 2.5 Gb of free space to perform a test run. Be sure to change SAR_CONFIG for the test run and source it. You will want to configure SAR_CONFIG differently once you have tested the software and organized your working space.

```
% cd /home/ROI_PAC_DIST
% vi SAR_CONFIG
% source SAR_CONFIG
```

% cd TEST_DIR
% cd 930110
% gunzip IMAGERY1993011018252739T1Of3.Z
% make_raw.pl PRC SARLEADER* 930110
% cd ../950523
% gunzip IMAGERY1995052318253409T1Of3.Z
% make_raw.pl PRC SARLEADER* 950523
% cd ..
% process_2pass.pl int.proc

8. **Examine the results.** The script process_2pass.pl may take1-2 hours to complete. You should find the directory int_930110-950523 full of files. The finished product is the file geo_930110-950523.unw. If you have the program dgx.f, then you can view the image. Otherwise, you can try to view the file with a different program that can display binary image files. The file is composed of floating point values in an band-interleave format, i.e. alternating lines of amplitude and phase. The size of the file should be ~10 Mb. The header information for the file can be found in geo_930110-950523.unw.rsc.

% cd /home/ROI_PAC_DIST/TEST_DIR/int_930110_950523
% dgx.pl geo_930110-950523.unw

Congratulations! If process_2pass.pl ran smoothly, then ROI_PAC is installed correctly. You are now ready to process your own SAR data. Create a workspace where you will process future data. You may also want to create a new directory where you can archive your DEM and orbit files. Remember to go back and change SAR_CONFIG to reflect your new setup.

B.3   ROI_PAC Processing Instructions

The following is a step-by-step outline of a typical processing run. Instructions are found to the left with the appropriate unix commands to the right. Refer the reference tables for additional information.

1. **Set-up**

Change directory to workspace	% cd /workspace
Remove all files.	% rm -r *
Do not erase unsaved files!	
Make directory for each SAR scene.	% mkdir /workspace/date1
	% mkdir /workspace/date2
Copy configuration file to workspace.	% cp /ROI_PAC_DIST/SAR_CONFIG .
Source configuration file.	% source SAR_CONFIG
Create parameter file.	% vi date1-date2.proc
Example shown below.	

```
SarDir1=920610
SarDir2=980509
IntDir=920610-980509
DEM=/a/computer/data/sar/DEM/region.dem
unw_seedx=981
unw_seedy=254
flattening=topo
INTER_MODEL=/a/computer/data/sar/model_
```

2. Download Orbit Files

Change directory to orbit file destination.   % cd /orbit/PRC/ERS#
Download orbit file (see section A.4).
Repeat above for second SAR scene.

3. Upload Raw SAR Data

Change directory to /workspace/date1.   % cd /workspace/date1
Download data from WInSAR,
      or
Insert first tape or CD into device.
Upload data.   For tape: % load_remote_tape.pl
                                                              For CD: % load_cd.pl
Repeat above for second SAR scene.
Note: Files may need to be re-named to IMAGERY* and SARLEADER*.

4. Process Raw SAR Data

Change directory to data.   % cd /workspace/date1
Run make_raw.pl.   % make_raw.pl PRC SARLEADER* YYYYMMDD
usage: make_raw.pl ORBIT_TYPE LEADER_FILE DATE
Repeat above for second SAR scene.

5. Create Differential Interferogram

Run processing script.   % cd /workspace
(See section Table B.3.).   % process_2pass.pl date1-date2.proc

6. View Results

Run dgx.pl or other imaging software.   % cd /workspace/date1-date2
                                                              % dgx.pl geo_date1-date2.unw

Table B.1: Create a file named date1-date2.proc that contains the input parameters for the main processing script. The file must define the following parameters:

Required Parameter	Description
SarDir1	Directory containing raw SAR data for first scene
SarDir2	Directory containing raw SAR data for second scene
IntDir	Directory containing ROI_PAC output files

Table B.2: The following optional parameters can also be specified in date1-date2.proc.

Optional Parameters	Description	Optional Values	Default Value
SimDir	Directory containing topographic simulation output files		SIM
DEM	Path to Digital Elevation Model (DEM) used to remove topography		NULL
GeoDir	Directory containing tectonic simulation output files		GEO
FilterStrength	Strength of the filter used in the processing.	0-1	0.75
UnwrappedThreshold	Determines the extent of unwrapping. Connected regions with a magnitude greater than the threshold as found in the file *.msk are included in the unwrapping process.	0-1	0.1
OrbitType	Type of orbit file, either precise orbits (PRC) or Delft orbits (ODR)	PRC, ODR	ODR
BaselineType	Given to discriminate baseline estimation technique		OrbitType
Rlooks_sim	Specifies the number of looks to take when processing the raw SAR data.		4
Rlooks_int			Rlooks_sim
Rlooks_unw			Rlooks_sim
Rlooks_sml			16
pixel_ratio	pixel size ratio of azimuth/range		5
Alooks_sml	Defined as (pixel_ratio X Rlooks_sml)		80

Table B.2: Continued.

Optional Parameters	Description	Optional Values	Default Value
before_z_ext			1500
after_z_ext			1500
near_rng_ext			700
far_rng_ext			0
usergivendop1	User defined doppler value for scene 1		0
usergivendop2	User defined doppler value for scene 2		0
unw_seedx	x coordinate where the phase unwrapping begins. The default places the seed in the middle of the image.		-9999
unw_seedy	y coordinate where the phase unwrapping begins. The default places the seed in the middle of the image.		-9999
x_start	Specifies the range offset in pixels between the two SAR scenes. The default value signals the scripts to use the estimated range offset calculated from the a priori orbit information.		0.01
y_start	Specifies the azimuth offset in pixels between the two SAR scenes. The default value signals the scripts to use the estimated azimuth offset calculated from the a priori orbit information.		0.01
flattening	Used to specify the method of flattening. Set this variable to "orbit" if you do not have a DEM or other model simulation. Set to "topo" to re-estimate the baseline information using a DEM and/or other model information.	orbit, topo	orbit

Table B.2: Continued.

Optional Parameters	Description	Optional Values	Default Value
Threshold_mag	Defines an amplitude threshold when producing a mask during the unwrapping. This helps to reduce side effects on the edges of the radar scene where amplitudes are small. (0=unwrap everywhere)	0 to 5e-5	5e-5
Threshold_ph_grd			0
sigma_thresh			1.0
smooth_width	Specifies the size of the filter window in range and azimuth used when creating the phase gradient mask		5
slope_width			5
concurrent_roi	Allows SAR processor to work on both SAR scenes simultaneously	yes, no	no
mapping		dem_based	dem_based
cleanup	Remove intermediate files when finished.	yes, no	no
CO_MODEL	Specifies a Coseismic model used in flattening. Make sure to set "flattening=topo". Read the instructions for INTER_MODEL for details about naming input files.		NULL

Table B.2: Continued.

Optional Parameters	Description	Optional Values	Default Value
INTER_MODEL	Specifies an Interseismic model used in flattening. Make sure to set "flattening=topo" for this option. Provide three data files for each component of displacement along with three resource files. ROI_PAC will expect the files to be named XE, XE.rsc, XN, XN.rsc, XU, and XU.rsc for the east, north, and vertical components, respectively, where the "X" can be a user defined prefix specified by the INTER_MODEL parameter.		NULL
Filt_method	Specify type of filter used.	psfilt, adapt_filt	psfilt
unw_method	Specify unwrapping method. Bridge.pl is only compatible with the "old" unwrapping method.	old, icu	old

Table B.3: The primary processing script is process_2pass.pl. The optional arguments, [DoItFrom] and [EndItAt], allow the user to control where the script begins and ends in the sequence of processing steps.

Function	process_2pass.pl	
Description	Goes from raw ERS data to geocoded interferogram with topography removed according to the 2-pass method	
Usage	% process_2pass.pl file.proc [DoItFrom] [EndItAt]	
Argument List	**Description**	**Value**
file.proc	Input parameter file	
DoItFrom	Define where to begin processing	raw, roi_prep, orbbase, slcs, offsets, resamp, flatorb, full_res, seismic, begin_filt, filtered, make_mask, unwrapped, done_sim_off, done_sim_removal, redo_base, use_sim_base, synth_offset, sim_removal, sim_removal_bsim, unwrapped_bsim
EndItAt	Define where to end processing	raw, roi_prep, orbbase, slcs, offsets, resamp, flatorb, full_res, seismic, begin_filt, filtered, make_mask, unwrapped, done_sim_off, done_sim_removal, redo_base, use_sim_base, synth_offset, sim_removal, sim_removal_bsim, unwrapped_bsim, done

Table B.4: Structure of output files.

ROI_PAC File Suffix	ROI_PAC File Structure	Data Type
.slc	cpx	complex
.int	cpx	complex
.cor	rmg	floating point
.unw	rmg	floating point
.hgt	rmg	floating point
.amp	cpx	complex

cpx = complex values; alternating real and imaginary pixels
rmg = alternating lines of amplitude and phase (i.e., band interleave)

B.4   Obtaining Orbit Files

There exist two sources for obtaining accurate orbits for the ERS satellite. The Delft Institute for Space-Oriented Space Research (DEOS) (http://www.deos.tudelft.nl/) provides orbit information for both ERS1 and ERS2. An alternative source is the Precise Orbit Products (http://earth1.esrin.esa.it/f/eeo2.400/pgersorbprc) through the European Space Agency (ESA) (http://www.esa.int/). To upload these orbit files, follow the instructions below.

B.4.1   ODR Orbit Files From DEOS

From the ERS Precise Orbit Determination web-page
(http://www.deos.tudelft.nl/ers/precorbs/), click the "orbit" link under the content heading. Choose the link for "precise orbits" corresponding to either the ERS1 or ERS2 satellite and follow the download instructions for ODR files and the arclist.

B.4.2   PRC Orbit Files From ESA

An account must be established with ESA to download their orbit products. The PRC filename (PPP_yymmdd_no_revi.Z) can be interpreted as follows:

PPP	=	PRC
yymmdd	=	start date of the orbit: year (yy), month (mm), day (dd)
no	=	absolute orbit number (revolutions since launch)
revi	=	revision id

Retrieve the orbit file with the date and orbit number that most closely precedes the date and orbit of the given SAR scene. After downloading the necessary files, update the list of orbit files by running arclist_PRC.pl in the same directory.

Table B.5: Important files created during the processing are listed below. Not all of the files listed are created during every processing scenario. For example, additional files are created when you include a seismic model in the processing. Capital letters designate where names will vary according to the input parameters in date1-date2.proc.

Filename (listed in order of creation for v1.0beta)	Description
log	ascii file of command line arguments called during processing
log1	ascii file with standard output and messages
DATE1.slc	single look complex image produced from raw data
DATE1_DATE2_baseline.rsc	calculated baseline information between scenes
fitoff_ampcor.out	parameters used to align SAR scenes
DATE1-DATE2.int	interferogram created from date1.slc and date2.slc (full resolution)
DATE1-DATE2.amp	multi-look amplitude file
zero.hgt	zero-valued dummy height file
flat_ORBIT_DATE1-DATE2.int	flattened interferogram using a priori orbit information
ramp_ORBIT.unw	flat-earth ramp using a priori orbit information
DATE1-DATE2.cor	correlation between flat_ORBIT_Date1-Date2.int and DATE1-DATE2.amp
SIM_#rlks.hgt	extracted DEM in range, azimuth, and height coordinates
radar_#rlks.hgt	extracted DEM in satellite coordinates
radar_ORBIT_#rlks.unw	simulated unwrapped interferogram in satellite coordinates
DATE1-DATE2-sim_ORBIT_4rlks.int	wrapped differential interferogram
MODEL#rlks.unw	simulated unwrapped differential interferogram using seismic model
DATE1-DATE2-sim_ORBIT-MODEL#rlks.int	Wrapped differential interferogram; simulated orbital gradient and seismic model removed
phase_var_ORBIT_#rlks.msk	mask calculated from the phase variance
filt_DATE1-DATE2-sim_ORBIT-MODEL#rlks_c##.unw	unwrapped, filtered, differential interferogram with seismic model removed
total_DATE1-DATE2-MODEL#rlks.unw	unwrapped differential interferogram (including orbital ramp) with seismic model removed
radar_SIM_#rlks.unw	revised simulated interferogram using re-estimated baseline values and topography
filt_DATE1-DATE2-sim_SIM_#rlks_c#.unw	filtered, unwrapped, differential interferogram using new baseline values

Table B.5: Continued.

Filename (listed in order of creation for v1.0beta)	Description
geo-DATE1-DATE2.unw	final geocoded, filtered, unwrapped, differential interferogram
geo-DATE1-DATE2-MODEL#rlks.unw	final geocoded, filtered, unwrapped, differential interferogram with the simulated seismic model removed

B.5   Troubleshooting

1. Should I be concerned by the error message "** ERROR **: only 0 bytes are read out of 11812 requested" ?

   This error message is fairly common and can be ignored.

2. Should I be concerned by the error message "Note: Nonstandardfloating-point mode enabled. See the Numerical Computation Guide ieee_sun(3M)"?

   This warning is printed by all the programs that are compiled with the "-fast" optimization and can be ignored.

3. What is wrong when the processing aborts following the message "Too few points left after culling: 2 left"?

   This error occurs when the SAR processor is unsuccessful at determining the offset between the two images. There are two points when this could occur: 1) while trying to find the offset between the *slc files, or 2) while finding the offset between the resampled interferogram and the simulated interferogram (DEM based). Look at the file fitoff_ampcor.out or amp-mag.out, respectively. If the "number of points remaining" is less that 50, then the scripts will abort. If the number is just under 50, you can try to reduce the threshold by running "fitoff" manually. Look at the perl script make_offset.pl for the correct syntax. If the number of points remaining is significantly less than 50, then the orbit or timing information for the two scenes may be incorrect resulting in a poor initial guess for the offset between scenes. You may need to manually specify the offset between the two *slc files by including x_start and y_start in the *proc file. Alternatively, check question 14 for another possibility.

4. How much disk space is required to process one frame?

   You will need about 6 GB of disk space.

5. Why doesn't dgx.pl work?

   The base program, dgx.f, was not included in the ROI_PAC distribution. If you do have this program, then you may have to reduce the bit depth to 8 on your monitor or switch to a monitor on a different machine. For SunOS, you can use the UNIX program "m64config" to change the bit depth.

6. What should I do if nothing seems to work?

   Often the processing routines fail if previous output files exist. Try deleting intermediate files and start the process again. If problems continue to arise, then delete all files and begin anew.

7. How can I transfer the interferogram into an image file?

> While viewing an image using dgx.pl select the image amplitude (Amp), height or phase (Hgt), or a combination of amplitude and height (Mix). If you press the middle mouse button on the image part of the window, you get a "Zoom" window that can zoom in or out, and print what is visible in the window. If you want to see the full image, you can zoom out 4-5 times. Pressing the right mouse button on the "Print" button will write the image to a JPEG file.

8. Why did the processing fail to unwrap the interferogram?

> If the unwrapping process begins in a region with no coherence, then the unwrapping procedure will fail. The point where this process begins can be set by defining the point in the input parameter file (date1-date2.proc) using the parameters unw_seedx and unw_seedy. A seed point can be found by looking at any filtered, wrapped interferogram, such as filt*.int. Use DGX to view the file and choose a point in the image where the phase is smooth and coherent.

9. What is an acceptable maximum perpendicular baseline?

> There is no set value for what perpendicular baseline is acceptable. The maximum threshold will depend on what you consider to be an acceptable phase error resulting from the overall coherence of the image and the caliber of the DEM. Any topographic signature remaining in the image may suggest that the perpendicular baseline is too large for the given DEM. The baseline information for a processed tandem pair can be found in the file date1_date2_baseline.rsc.

10. How can I determine if a raw ERS data file is corrupted?

> In general, the size of the imagery file should be 300Mb ($\pm$ 25 Mb). The SARLEADER file should be about 28 Kb and the VDF file about 2 Kb. Large deviations from these sizes might suggest a problem. To test the file you can run the script make_raw.pl and examine the file date_parse_line.out. This file will list lines in the file that have bad data values or missing data. Several lines of missing data should not be a concern. ROI_PAC simply duplicates the previous line. If dozens or hundreds of adjacent lines are missing from a section of the file, then the file may be corrupted.

11. What has gone wrong when the processing pauses with "p must be at least 2 in moment"?

> The processing does not have enough information to calculate the statistical information necessary to determine the offset between two SAR scenes. Type "go" to resume the processing, which should subsequently fail. Refer to question 3 above for further instructions.

12. Why does the unwrapping process fail in the program trees.c?

   The program trees.c is inefficient at processing large files. Try using the icu unwrapping method.

13. Why does icu fail while trying to unwrap the image?

   Try running icu manually. If the programs quits with an error message about the azimuth buffer size, you will need to lower the value in the icu input file. If it complains about the range buffer size, the icu program is not setup for the RAM configuration on your computer. You will need to edit the file sizes.inc in the ROI_PAC source directory for the icu package and recompile the program.

14. Why does the amplitude band appear out of focus or blurred?

   Occasionally the software incorrectly calculates the doppler ambiguity, resulting in a blurred image observed in the *.slc image. The scripts will often fail during make_offset.pl. This problem is most prevalent for data collected by ERS2 after February of 2000 due to the loss of one of its gyroscopes. Check the DOPPLER_RANGE0 value in the *raw.rsc for both SAR scenes. The value should range between 0.5 and -0.5. If the value is outside this range, add ± 1, replace the value in the *raw.rsc file, and restart the processing. DOPPLER_RANGE0 should be similar for SAR scenes along the same latitude, or scenes of the same frame.